EFFICIENT DURABLE SOLAR-DRIVEN WATER SPLITTING DEVICES

By

SHINJAE HWANG

A dissertation submitted to the

School of Graduate Studies

Rutgers, The State University of New Jersey

In partial fulfillment of the requirements

For the degree of

Doctor of Philosophy

Graduate Program in Chemistry and Chemical Biology

Written under the directions of

Eric L. Garfunkel and

G. Charles Dismukes

And approved by

_____

_____

_____

_____

_____

New Brunswick, New Jersey

JANUARY, 2020

ABSTRACT OF THE DISSERTATION

EFFICIENT DURABLE SOLAR-DRIVEN WATER SPLITTING DEVICES

by SHINJAE HWANG

Dissertation Directors:

Prof. Eric L. Garfunkel and

Prof. G. Charles Dismukes

The conversion of solar energy into chemical energy using renewable feedstocks such as water continues to expand at an accelerating rate. One device capable of producing hydrogen, a renewable chemical fuel, is the photoelectrochemical (PEC) cell which "splits water" by breaking it into its constituent elements at two distinct electrodes connected by an ion conducting medium. However, achieving both high efficiency and device stability at low-cost remain major challenges to the practical use of PEC devices at any scale. The operation of PEC devices can be better understood by examination of the three key components: (i) the catalysts upon which the water is split, (ii) the photoabsorbing semiconductors which capture energy from light, and (iii) passivation layers between catalyst and photoabsorber. We examined each component using low-cost earth-abundant materials and found that a key aspect of creating long-term stable and energy-efficient PEC devices is a full understanding of how best to integrate crystalline catalysts and photoabsorbers, using an appropriate interfacial passivation layer. The two key roles of the passivation layer are first to ensure that the catalyst and photoabsorber layers do not chemical

modify each other, and second to ensure that the chemically unstable photoabsorber is protected by the corrosive solution.

In chapter 2, thin-films of nickel phosphide compounds (Ni_xP_y) are proposed and developed as low-cost catalysts for the hydrogen evolution reaction (HER). The optimal structure studied in this work involved a tri-layer photocathode structure consisting of cubic-NiP_2 catalyst, a TiN ultrathin-film passivation layer, and a Si photoabsorber. We found that an ultrathin interfacial layer of TiN can effectively hinder atomic diffusion during high temperature fabrication, while also protecting the underlying photoabsorber against corrosion during illumination in electrolytes. The thin-film deposition process developed resulted in a cubic-NiP_2 film to be grown normal to the planar direction; this film results in hydrogen production with a comparable turnover frequency to that of other state-of-the-art transition metal phosphides (TMPs) for the HER (1.04 H_2 s^{-1}). This interfacial fabrication method maintains a stable photocurrent density without loss for at least 125 hours, the duration of the test.

In Chapter 3, we extend this fabrication technology, demonstrating crystalline nickel phosphide catalysts on high efficiency III-V semiconductors in place of Si as photoabsorber, increasing the overall device efficiency. Application of an ultra-thin TiN layer on a high-performance buried junction photocathode comprised of n^+p-$GaInP_2$ allows processing at elevated temperatures that is needed for growth of crystalline Ni_5P_4. The resulting Ni_5P_4 catalyst on a TiN protection layer results in nano-islands of Ni_5P_4 that produce negligible absorption loss in the visible spectrum. The light saturated photocurrent density is equivalent to the same junction using a PtRu decorated benchmark photocathode. We demonstrated that the resulting

catalyst-protection layer-$GaInP_2$ photocathode structure is stable for over 120 h, the limit of testing, exceeding all previous benchmarks.

Finally, in chapter 4, we investigate methods to create thin films of $SrNbO_2N$ as a low-cost wide-bandgap photoabsorber in a tandem photoabsorber structure with crystalline silicon. By introducing a thin film of TaN as diffusion layer on crystalline silicon, we could synthesize $SrNbO_2N$ by high temperature ammonolysis of the oxide precursor film without atomic diffusion across the interface. We experimentally determined the electronic band edge positions of thin-film $SrNbO_2N$ and related these to the understanding of efficient charge injection. Furthermore, we determined how oxynitride thickness, crystallite size, and electrochemical surface roughness contribute to optimal performance of the photoanode across a wide range of variables.

ACKNOWLEDGEMENTS

This thesis contains the work behind the following publications (in whole or part)

1. Hwang, S.; Porter, S. H.; Laursen, A. B.; Yang, H.; Li, M.; Manichev, V.; Calvinho, K. U. D.; Amarasinghe, V.; Greenblatt, M.; Garfunkel, E.; Dismukes, G. C. *J. Mat. Chem. A* **2019**, *7* (5), 2400.

2. Hwang, S.; Mow, R.; Young, J. L.; Laursen, A. B.; Li, M.; Yang, H.; Batson, P. E.; Steiner, M. A.; Greenblatt, M.; Deutsch, T. G.; Garfunkel, E.; Dismukes, G., M. Greenblatt, "Highly efficient and durable III-V semiconductor-catalyst photocathodes via a transparent pr otection layer" *submitted*

3. Hwang, S.; Porter, S. H.; Li, M.; Thrope, R.; Laursen, A. B.; Safari, A.; Greenblatt, M.; Garfu nkel, E.; Dismukes, G. C. "$SrNbO_2N$ thin-film as a photoanode for solar-driven water oxidati on" *submitted*

Although I alone obtained this Ph.D. degree, it could not have been possible without help from many people. First and foremost, I would like to thank my two advisors, Prof. Eric Garfunkel (Rick) and Prof. G. Charles Dismukes (Chuck), who allowed me to be a joint student between their two groups and exposed me to the surface sciences and catalysis world. As a joint student, I had access to many facilities and tools and allowing me to answer many research questions during my time here. With their guidance, I have learned teamwork, critical thinking, collaboration with other scientists, and how our research can impact the world. My Ph.D. journey would not have been possible without their intellectual support and mentorship.

I would like to thank Prof. Martha Greenblatt, who has not only served as a committee member but also as a co-PI for my project. With her advice, I was able to quickly learn solid-state chemistry and conduct fruitful research during my graduate studies.

I would also like to thank Prof. Torgny Gustafsson and Prof. Leonard Feldman for their help and guidance during the five years of my Ph.D study. I have learned many aspects as a scientist, especially how physicists approach the scientific problems and how to solve it.

I would like to thank my lab mentors, Dr. Graeme Gardner, Dr. Spencer Porter, and Dr. Anders Laursen. Dr. Graeme Gardner guided me through catalysis work during my first year, and Dr. Spencer porter took over the mentorship and taught me leadership and communication skills, as well as how to fix the lab instruments. Dr. Anders Laursen has shared all his secrets for (photo)electrocatalysis and taught me how to convince other scientists with our research. Without their help, my days at Rutgers would not have been as productive or enjoyable.

I also want to give my thanks to my same-year colleagues, Karin Calvinho and Mengjun Li, who spent five years with me in the Dismukes and Garfunkel lab, respectively. It has been an absolutely joyful journey with them, including all the various discussion we had and watching how we grew together as scientists.

Collaborating with the NREL team has been very rewarding and expanded my knowledge in multiple directions. I thank Dr. James Young, Dr. Todd Deutsch, Dr. Myles Steiner, and Dr. Daniel Friedman for having constructive discussions and for their help in strengthening this dissertation.

I was very fortunate to have many fellow graduate students, postdoc, and scientists who have helped me in various ways. Hongbin Yang and Dr. Philip E. Batson for STEM, Dr. Ryan Thorpe and Dr. Boris Yakshinskiy for RBS, Dr. Sylvie Rangan for UPS, and Dr. Ahmad Safari for PLD. Here, I would like to extend my thanks to all the colleagues in GGF group and

Dismukes group including, Dr. Gennady Anayev, Dr. Feixiang Luo, Dr. Paul Smith, Dr. Xiuyan Li, Dr. Colin Gates, Dr. Yuan Zhang, Dr. Aleksandra Biedron, Dr. Malathi Kalyanikar, Bin Liu, Ajay Kashi, Hengfei Gu, Krishani Teeluck, Ryan Crichton, Apostolos Zournas, Yifei Li, and Thomas Geannkakes.

I would like to thank my committee members Prof. John Brennan and Prof. Deidre O'Carroll for their guidance and constructive suggestions on my dissertation.

Finally, I would like to express my deepest gratitude to my wife, Eun Cho, my son Hejun, and my family, especially my mother, for their unconditional love, support, and prayers.

Dedication

This dissertation is dedicated to a memory of my father, Myungshin Hwang

Table of Contents

List of Figures

List of Tables

Chapter 1: Introduction

1.1 Carbon Economy

Carbon and hydrocarbon fuels sources have accumulated near the earth's surface by the massive production and settling of biomass over millions of years. These abundant carbon-based species (solids, liquids and gases) have become relatively easy to handle as fuel sources, and have been the primary energy source supplying over 80% of world energy consumption for ages.[1,2] This is the basis of the concept of a global carbon economy.

Since the industrial revolution, a tremendous amount of fossil fuel has been consumed by humanity and is expected to last only 50-100 years.[2] New technologies now enable greater access to carbon-based fuels that were not accessible in the past, and these innovations will likely make fossil fuel last longer than a century.[3] However, fossil fuels are still limited and are not sustainable in the long term. More important, we must seriously consider the negative environmental effects of fossil fuel consumption.

1.2 Environmental Effects of Carbon Economy

Carbon emission in the atmosphere (predominantly as CO_2) has historically been well balanced by nature thorough photosynthesis processes which utilize sunlight to fix CO_2. This process converts CO_2 into carbohydrates and other chemicals that enable chemical energy to be stored in plants. This class of photochemical reactions accumulates carbon as plants and eventually biomass, which through high pressure and high-temperature geological processes

ends up as carbon reserves, our current fuel sources.[4] However, the massive usage of carbon resources by humanity has resulted in a "timing problem" and has broken this balance. As illustrated in Figure 1.1,[3] photosynthetic production and geological processes take 10^{6-8} years, whereas the energy production generated by consuming fossil fuels takes only a couple of seconds.[3] This discrepancy is more than 12 orders of magnitude, and has given rise to an

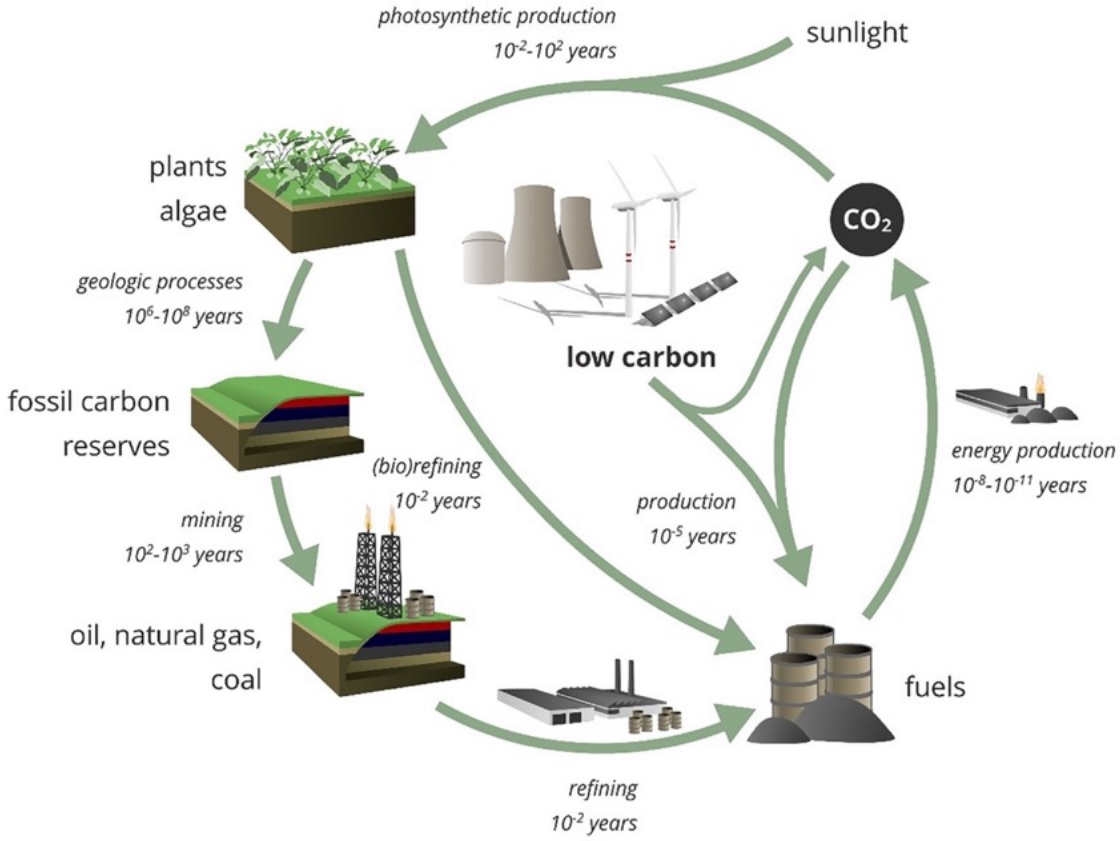

Figure 1.1 Timing in the carbon redox cycle[3]

acceleration of production of CO_2 in the atmosphere. CO_2 is a powerful greenhouse gas that has helped to stabilize the temperature of the earth, with an atmospheric concentration of CO_2 of 280 ppm, over hundreds of thousands of years. However, since the beginning of the industrial revolution the level of CO_2 has risen to 400 ppm. This increase is responsible for the rise in

average earth temperature, which results in a series of massive global changes including a rise in the sea-level.[5] The problem has been recognized by many intergovernmental organizations such as the IPCC[6] and is being addressed by a variety of approaches including regulations such as emissions trading systems.[7] However, without rapidly and globally moving our fossil fuel-dependent energy consumption to renewable energy sources, the problem appears intractable.

1.3 Hydrogen Economy

Hydrogen is the lightest element and is regarded as a critical and indispensable element to aid in decarbonization, enabling a more sustainable global energy system. Hydrogen can be stored and converted into electricity, or used directly as a fuel to power devices.[8,9]

Fuel	Energy type	Specific energy (MJ kg^{-1})
Hydrogen	Chemical	120
Methane	Chemical	47
Diesel	Chemical	43
Gasoline	Chemical	43
Coal	Chemical	23
Methanol	Chemical	20
Lithium-ion battery	Electrochemical	0.36-0.875
Alkaline battery	Electrochemical	0.67

Table 1.1 The specific energy of common fuels.[10]

Comparing energy density of different fuels, hydrogen has the most significant gravimetric energy density. (Table 1.1)[10] If the production, delivery (transportation), and efficient conversion of hydrogen into electricity (and H_2O) can be achieved on a large scale, hydrogen can become a key energy carrier. This concept could enable our current carbon economy to be transformed into a hydrogen economy. U.S., Department of Energy showed a future H_2@Scale energy system across the sectors (Figure 1.2).[11] This suggests intermittent renewable energy such as sun, and wind can be converted into electricity, which can operate water electrolyzers for storing hydrogen. The generated hydrogen can be used for power generation, fuel cell cars, and upgrading the fuels for other industrial applications.

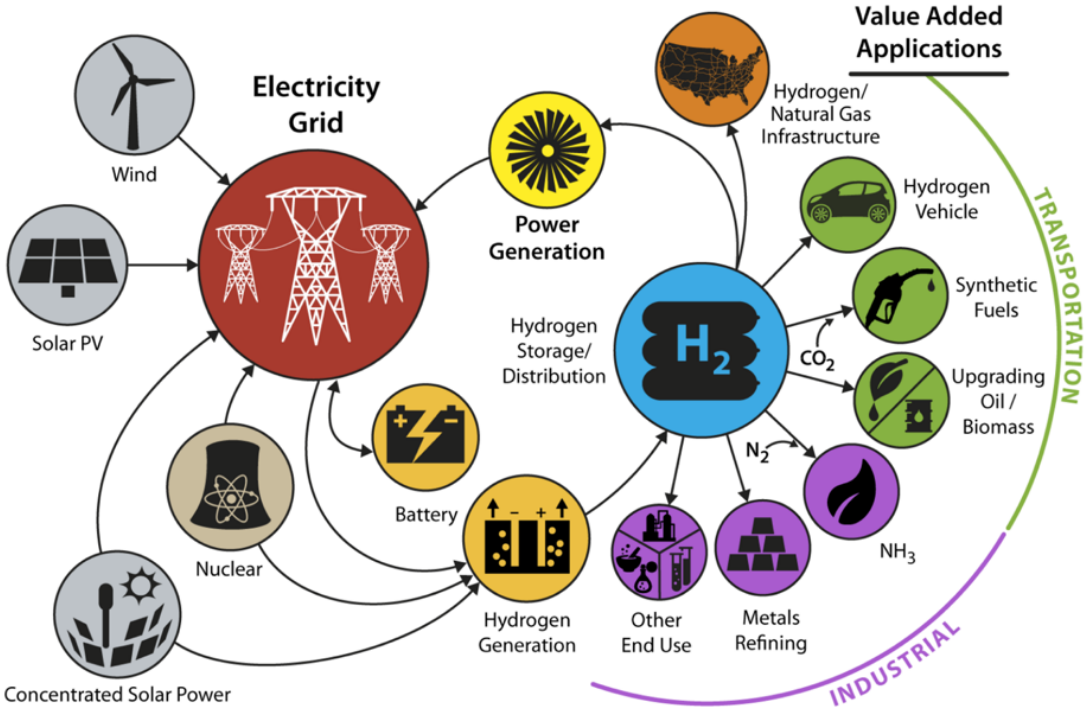

Figure 1.2 A future hydrogen-based economy and its energy system across the sectors

Recent advances in fuel cell technology and commercially available fuel cell cars makes the concept of a hydrogen economy more viable. However, the required amount of hydrogen to satisfy total world energy consumption makes developing a global hydrogen economy challenging. For example, among the total world energy consumption, the fraction of renewable energy is currently less than 10%. (Figure 1.3)[2] The global hydrogen production is close to 50 M metric tons,[12] and the predominant method for hydrogen production today still relies on steam reforming. If the world fuel-cell electrical vehicle (FCEV) demand exceed 50% of the total vehicles, hydrogen requires at least 100 M metric tons.[12] This motivates further technology development for capturing renewable energy and direct hydrogen production.

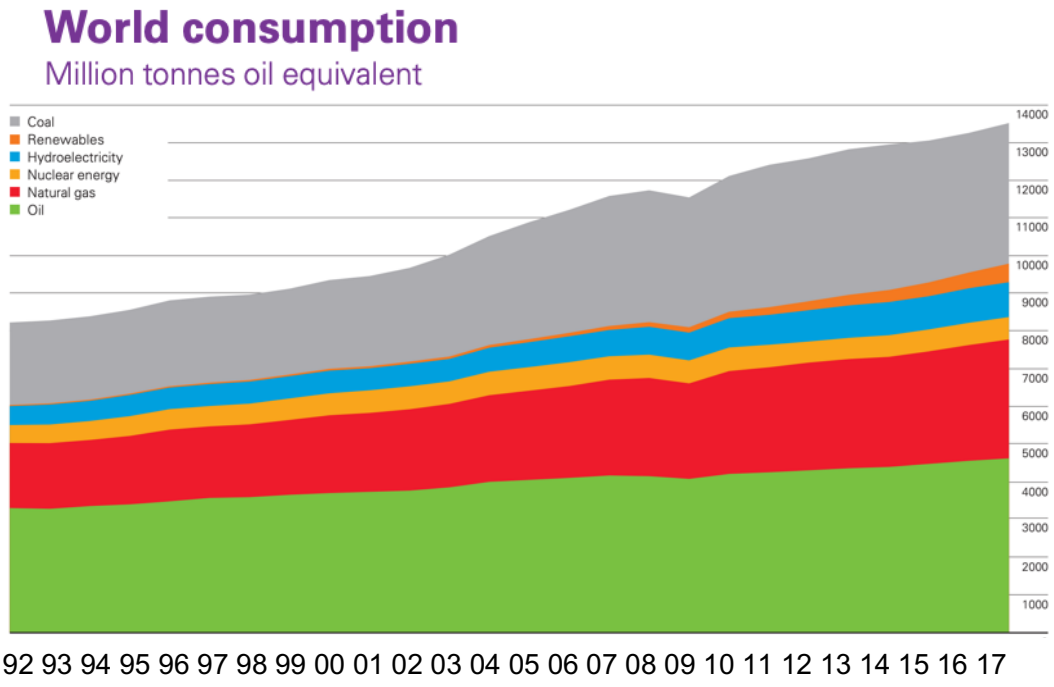

Figure 1.3 World energy consumption from 1992 to 2017

1.4 Potential of Solar Energy

Solar energy arriving at the surface of the earth is by far the largest CO_2-free energy source, totaling 173,000 TW. This energy source could supply a year of world energy consumption within an hour if all photon energy could be captured and stored without loss.[13] Unfortunately, solar energy is hard to capture with high efficiency and is even harder to store. About 50% of solar energy immediately leaves the earth through reflection and absorption in the atmosphere, and approximately 25% of the energy that absorbed at the earth's surface is stored as latent heat by water evaporation.[3] Photosynthesis stores less than 1% of energy (as chemical energy), and the rest of the energy is converted into heat.[12] The challenge is to capture solar energy efficiently and making this energy capable of meeting our energy needs.

State-of-the-art photovoltaic (PV) cells are now produced with approximately 50% of solar-to-power efficiency,[14] and recent development of low-cost solar-cells showed a potential to drop the electricity cost generated by PV cells.[15,16] If proper energy storage systems can be combined with PV devices, the fluctuations in radiation hitting solar panels can be mitigated and meet the our energy needs.

1.5 Solar-driven Water Splitting

Solar-driven water splitting is a photoelectrochemical process that can capture the sunlight and directly split the water into hydrogen and oxygen molecules.[17] Solar-driven water-splitting devices are also called “photoelectrochemical (PEC) cells”, and use this process to store energy as clean hydrogen.

There are two essential components for PEC devices:

1) Water splitting catalysts – Two separate catalysts for hydrogen and oxygen generation (evolution)
2) Photoabsorbing semiconductors

Similar to a water electrolyzer (EC), a PEC device requires efficient water splitting catalysts for both anode and cathode, and the reaction can be summarized with following equations:

$$2H_2O \rightarrow 2H_2 + O_2(1.23\ eV + \eta(overpotential))$$

Oxygen Evolution Reaction (OER), which takes place at the anode:

$$2H_2O \xrightarrow[Ox]{catalyst,\ 4h^+} O_2 + 4H^+ + 4e^-$$

Hydrogen Evolution Reaction (HER), at the cathode:

$$4H^+ \xrightarrow[Red]{catalyst,\ 4e^-} 2H_2$$

The conversion of one molecules of H_2O to H_2 and $1/2O_2$ requires 237.2 kJ/mol, the free energy at standard condition, which corresponds to 1.23 V per electron based on the Nernst equation.[18] However, in practical operation, additional voltages are required to split the water to H_2 and O_2. The additional voltage needed to drive the reaction is called the overpotential, and comes from kinetic and mass transportation limitations, and ohmic losses. Therefore, catalysts that efficiently split water at both anode and cathodes are required to mitigate unnecessary overpotential.

Another requirement is efficient photoabsorbing semiconductors. Similar to PV devices, PEC devices use photoabsorbing semiconductors, but instead of generating electricity, they generate charge that is "injected" into molecules at the solid-liquid interface, splitting water. Similar to PV devices, PEC semiconductor should have high absorption coefficient, low charge recombination, and long carrier lifetime.[19] Furthermore, semiconductors should provide enough photovoltage to split the water (>1.23 V + η). This has been challenging for single junction semiconductor PEC devices,[20] and often requiring multijunction structures.[21,22] For example, a tandem junction device uses two semiconductors that consist of wide bandgap(top) and narrow bandgap (bottom) semiconductors. As shown in Figure 1.4a,[23] a top junction can capture UV-Vis light, and the bottom junction utilizes the Vis-NIR light. Adding additional junctions (e.g., triple junction structures) are also capable of increasing the photovoltage (Figure 1.4b).[24] However, PEC devices do not require more than 1.8 V (assuming a ~0.5 V overpotential); any additional voltage is waste. Also, increasing the photovoltage by additional junctions can compromise the total current density, which is more directly related to solar-to-hydrogen efficiency (STH).[25]

Compared to combined photovoltaic+electrolyzer (PV+EC) devices, PEC ones can avoid extra fabrication costs and lower the overall system cost.[26] Also, PEC devices should minimize wasted photovoltage when junctions are properly designed. However, this is not the case for PV-EC device, because PV-EC devices have an unmatched (photo)voltage and (photo)current from PV and water electrolyzer.

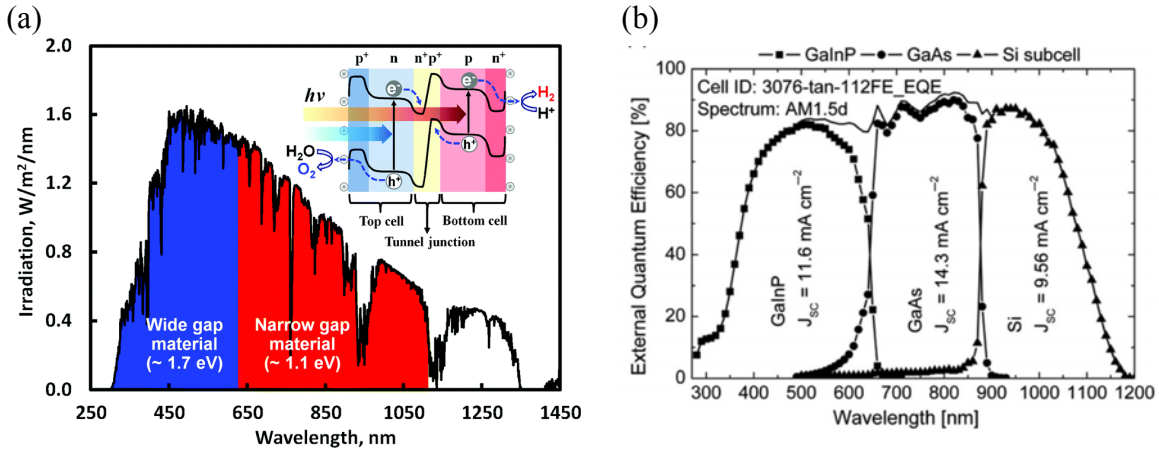

Figure 1.4 (a) Solar spectrum (AM 1.5G) coverage by a tandem photoabsorbing semiconductor. The top cell is formed with a wide-bandgap semiconductor and the bottom cell with a narrow bandgap semiconductor. The inset schematic shows a device in a tandem design composed of dual pn-junctions, co-catalysts for oxygen and hydrogen evolution, and a recombination layer (tunnel junction);[22] (b) External quantum efficiency and solar spectrum coverage (AM 1.5d) of triple junction semiconductors. (Top: GaInP, middle: GaAs, bottom, Si)

1.6 Efficient and Durable PEC devices

Since the first PEC work by Fujishima and Honda almost 50 years ago,[20] PEC efficiency has dramatically improved, and state-of-the-art devices can achieve almost 20% of STH.[27] However, the stability of the most efficient devices has not been resolved and remain a major challenge for the PEC community. For stable PEC devices, in addition to maintaining high efficiency, careful consideration has to be made of the top layer that consists of semiconductor/catalyst/electrolyte junctions. (Figure 1.5) First, the catalyst layer has to be transparent enough to maintain a saturated current density that is generated by the semiconductor. This often requires a thin-film or nanoparticle film of an efficient catalyst. [28] Second, both the catalyst and protection layer should be stable enough to protect the underlying semiconductor from the corrosive electrolytes used in devices. Ideally, both layers should have minimum parasitic absorption with little reflection loss at the semiconductor to help maintain high efficiency. Lastly, rapid charge injection has to be made from the semiconductor to the catalyst/electrolyte interface. Facile charge injection can be achieved by a clean interface between the semiconductor and protection/catalyst layers with proper band alignment.[19]

In this dissertation, the properties mentioned above were considered, leading to the design and fabrication of a set of novel thin-film catalyst-protection layer structures that are made of earth-abundant elements. These layers were applied on in-house Si and demonstrated applicability on commercially available Si PV cells. Also, our thin-film catalyst-protection layer structures were synthesized on high-performance $GaInP_2$ semiconductors, and highly efficient and durable performance PEC devices were achieved. Furthermore, fabrication of a perovskite oxynitride semiconductor in a PEC device was demonstrated. Overall, the body of work outlined

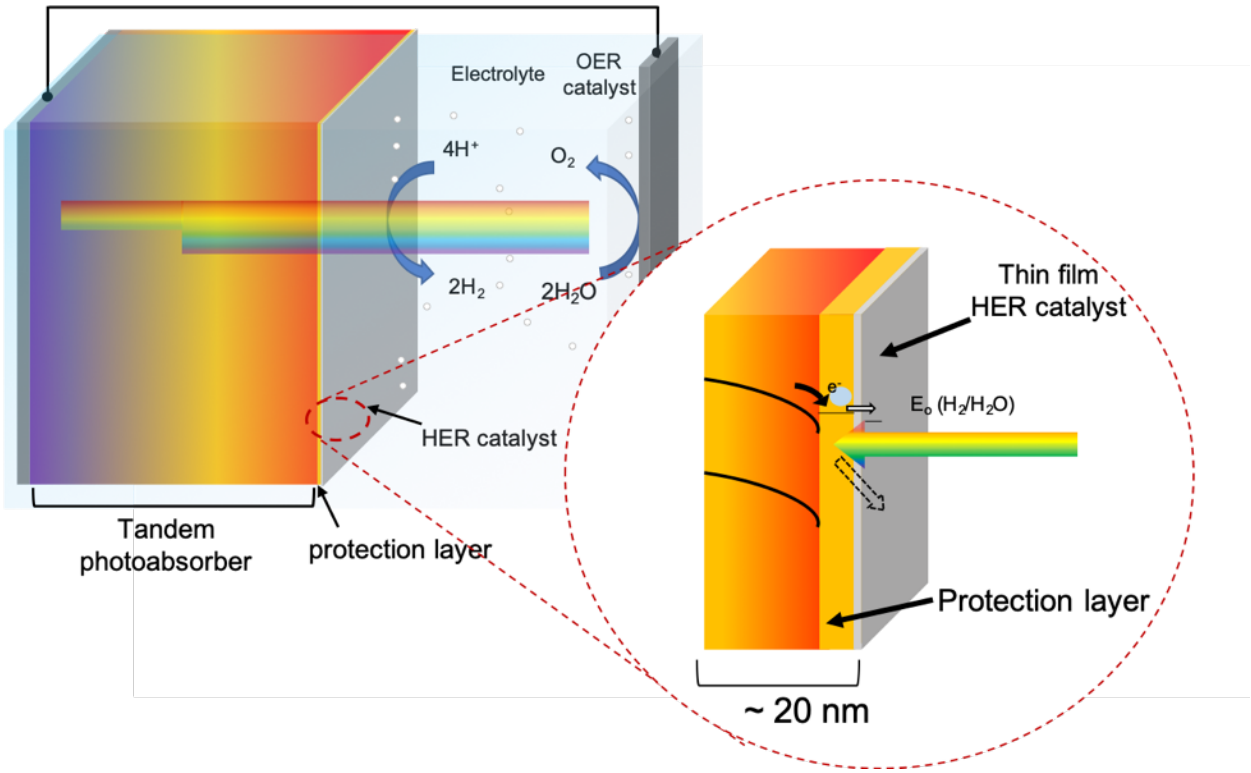

Figure 1.5 Schematic of a tandem PEC configuration. (Left) Schematic illustrates the direction of light and charge at semiconductor/protection layer/catalyst/electrolyte junctions

in this thesis discusses new PEC device structures and fabrication methods. PGM-free water-splitting catalysts, protection layers, and wide-bandgap photoabsorbing semiconductors are design, synthesized and characterized using a host of powerful methods, giving new understanding of the fundamental material properties at the device level.

1.7 References

(1) Dresselhaus, M. S.; Thomas, I. L. *Nature* **2001**, *414* (6861), 332.

(2) BP Statistical Review of World Energy, **2019**, 68th editions, https://www.bp.com/content/dam/bp/business-sites/en/global/corporate/pdfs/energy-economics/statistical-review/bp-stats-review-2019-full-report.pdf (accessed September 2019)

(3) Martens, J. A.; Bogaerts, A.; De Kimpe, N.; Jacobs, P. A.; Marin, G. B.; Rabaey, K.; Saeys, M.; Verhelst, S. *ChemSusChem* **2017**, *10* (6), 1039.

(4) Archer, D. *J. Geophys. Res.* **2005**, *110* (C9), 1769.

(5) Kopp, R. E.; Kemp, A. C.; Bittermann, K.; Horton, B. P.; Donnelly, J. P.; Gehrels, W. R.; Hay, C. C.; Mitrovica, J. X.; Morrow, E. D.; Rahmstorf, S. *PNAS* **2016**, *113* (11), E1434.

(6) Masson-Delmotte, V.; Zhai, P.; Skea, J.; (null), H.-O. P.; Shukla, P. R.; Pirani, A.; Moufouma-Okia, W.; Pean, C.; Pidcock, R.; Connors, S.; Matthews, J. B. R.; Chen, Y.; Zhou, X.; Gomis, M. I.; Lonnoy, E.; Maycock, T.; Tignor, M. *The Intergovernmental Panel on Climate Change*. 2018, pp 1–24.

(7) Rogge, K. S.; Schneider, M.; Hoffmann, V. H. *Ecological Economics* **2011**, *70* (3), 513.

(8) Staffell, I.; Scamman, D.; Abad, A. V.; Balcombe, P.; Dodds, P. E.; Ekins, P.; Shah, N.; Ward, K. R. *Energy Environ. Sci.* **2019**, *12* (2), 463.

(9) The Green Hydrogen Report, *Department of Energy* **1995**, https://www.hydrogen.energy.gov/pdfs/greenhyd.pdf (accessed September 2019)

(10) Lower and Higher Heating Values of Fuels, http:// hydrogen.pnl.gov/hydrogen-data/lower-and-higher-heating-values-hydrogen-and-other-fuels (accessed September 2019).

(11) H2@scale, U. S. Department of Energy, www.energy.gov/eere/fuelcells/h2scale (Accessed September 2019)

(12) Melaina, M.; Penev, M.; Heimiller, D. *Resource Assessment for Hydrogen Production: Hydrogen Production Potential from Fossil and Renewable Energy Resources*; 2013.

(13) Trenberth, K. E.; Fasullo, J. T.; Mackaro, J. *J. Climate* **2011**, *24* (18), 4907.

(14) Geisz, J. F.; Steiner, M. A.; Jain, N.; Schulte, K. L.; France, R. M.; McMahon, W. E.; Perl, E. E.; Friedman, D. J. *IEEE Journal of Photovoltaics* **2018**, *8* (2), 626.

(15) Dou, B.; Whitaker, J. B.; Bruening, K.; Moore, D. T.; Wheeler, L. M.; Ryter, J.; Breslin, N. J.; Berry, J. J.; Garner, S. M.; Barnes, F. S.; Shaheen, S. E.; Tassone, C. J.; Zhu, K.; van Hest, M. F. A. M. *ACS Energy Letters* **2018**, *3* (10), 2558.

(16) Tong, J.; Song, Z.; Kim, D. H.; Chen, X.; Chen, C.; Palmstrom, A. F.; Ndione, P. F.; Reese, M. O.; Dunfield, S. P.; Reid, O. G.; Liu, J.; Zhang, F.; Harvey, S. P.; Li, Z.; Christensen, S. T.; Teeter, G.; Zhao, D.; Al-Jassim, M. M.; van Hest, M. F. A. M.; Beard, M. C.; Shaheen, S. E.; Berry, J. J.; Yan, Y.; Zhu, K. *Science* **2019**, *364* (6439), 475.

(17) Bard, A. J.; Fox, M. A. *Acc. Chem. Res.* **1995**, No. 28, 141.

(18) Walter, M. G.; Warren, E. L.; McKone, J. R.; Boettcher, S. W.; Mi, Q.; Santori, E. A.; Lewis, N. S. *Chem. Rev.* **2010**, *110* (11), 6446.

(19) Hwang, S.; Porter, S. H.; Laursen, A. B.; Yang, H.; Li, M.; Manichev, V.; Calvinho, K. U. D.; Amarasinghe, V.; Greenblatt, M.; Garfunkel, E.; Dismukes, G. C. *J. Mat. Chem. A* **2019**, *7* (5), 2400.

(20) FUJISHIMA, A.; HONDA, K. *Nature* **1972**, *238* (5358), 37.

(21) Turan, B.; Becker, J.-P.; Urbain, F.; Finger, F.; Rau, U.; Haas, S. *Nat Comms* **2016**, *7* (1), 12681.

(22) Urbain, F.; Tang, P.; Carretero, N. M.; Andreu, T.; Gerling, L. G.; Voz, C.; Arbiol, J.; Morante, J. R. *Energy Environ. Sci.* **2017**, *10* (10), 2256.

(23) Bae, D.; Pedersen, T.; Seger, B.; Malizia, M.; Kuznetsov, A.; Hansen, O.; Chorkendorff, I.; Vesborg, P. C. K. *Energy Environ. Sci.* **2015**, *8* (2), 650.

(24) Jain, N.; Hudait, M. K. *Energy Harvesting and Systems* **2014**, *1* (3-4), 121.

(25) Steiner, M. A.; Barraugh, C. D.; Aldridge, C. W.; Alvarez, I. B.; Friedman, D. J.; Ekins-Daukes, N. J.; Deutsch, T. G.; Young, J. L. *SUSTAIN. ENERG. FUELS* **2019**.

(26) Khaselev, O.; Turner, J. *Science* **1998**, *280* (5362), 425.

(27) Cheng, W.-H.; Richter, M. H.; May, M. M.; Ohlmann, J.; Lackner, D.; Dimroth, F.; Hannappel, T.; Atwater, H. A.; Lewerenz, H. J. *ACS Energy Letters* **2018**, *3* (8), 1795.

(28) Young, J. L.; Steiner, M. A.; Döscher, H.; France, R. M.; Turner, J. A.; Deutsch, T. G. *Nature Energy* **2017**, *2* (4), 17028.

Chapter 2: Creating stable interfaces between reactive materials: titanium nitride protects photoabsorber–catalyst interface in water-splitting photocathodes

2.1 Abstract

The development of a solar-driven water splitting device that replaces costly precious metals, while achieving stable high performance, is a major challenge. Transition metal phosphides are active and low-cost catalysts for the hydrogen evolution reaction (HER), although, none thus far have exhibited stable performance when interfaced with semiconductors. Here, we report on a monolithic junction consisting of cubic-NiP_2:TiN:Si, fabricated using both commercial and custom Si photovoltaics. Stable performance is achieved using an ultrathin film of crystalline TiN that effectively hinders atomic diffusion between interfaces during fabrication. Crystalline cubic-NiP_2 deposited on TiN/n^+p-Si retains 97% of the bare Si photovoltage, comparable saturation current density as bare Si, and has a turnover frequency of 1.04 H_2 site^{-1}s^{-1} at −100 mV applied potential. In acid, it requires only −150 mV additional overpotential compared to the benchmark, Pt/TiN/n^+p-Si, to reach a HER photocurrent density of −10 mA/cm^2. This photocathode maintains a stable H_2 photocurrent (±10%) for at least 125 hours, the duration of testing. When the same layers are fabricated on a commercial Si solar cell, this photocathode produced double the photocurrent density (36.3 mA/cm^2, under simulated 1.5 AM G illumination). Physical characterization gives detailed information on the properties responsible for the observed activity and durability of these interfaces. In general, the thin-film methodology presented here is widely applicable, demonstrates superior activity, and achieves long-term stability.

2.2 Introduction

Hydrogen is a renewable energy carrier, and could potentially replace a fossil-fuel-based economy by using advanced fuel cell technology to recover the stored energy.[1] However, the predominant method to produce hydrogen today involves steam reforming of natural gas resulting in CO_2 production.[2] This has motivated significant research into the production of clean H_2 from water, without the release of CO_2.[3,4] Solar-driven water splitting is a potentially clean and renewable hydrogen production technology, because it absorbs sunlight and produces only hydrogen and oxygen as products.[5] Efficient water splitting devices use two or more photoabsorbers to obtain sufficient photovoltage for bias-free photoelectrochemical cell (PEC) operation. A tandem configuration PEC has two absorbers in series, one with a narrow bandgap and a second one with a wide bandgap, where the bandgaps are carefully matched to optimize absorption across the solar spectrum[6-9] This configuration mimics the two photosystems found universally in natural oxygenic photosynthesis. Multijunction series-connected PV cells have also been demonstrated to achieve high solar-to-hydrogen efficiency as a photovoltaic-electrolysis (PV-EC) device configuration[10-14] However, because most semiconductors that operate in the visible-NIR spectrum, such as Si, $GaInP_2$, and GaAs are unstable in water, a protective interfacial layer is required between the photoabsorber and the catalyst/electrolyte to maintain operation. Interfacial protection layers comprised of wide bandgap oxides (e.g., TiO_2, Al_2O_3) or 2D chalcogenides (e.g., MoS_2) have been demonstrated to be superior to direct contact for stability.[15-18] An alternative approach, a back illumination (illuminating the non-catalyst part) of PV-EC setup has also been attempted to help enable prolonged durability.[13,19,20] In addition,

progress has been made towards replacing the archetypical (yet expensive and scarce) platinum catalyst, used for the hydrogen evolution reaction (HER), with non-noble catalysts. [21-23] However, successful integration of these reported catalysts to the underlying photoabsorbing semiconductors, while not compromising either materials performance and achieving long term passivation remains a very active research area for technology.

Silicon is a well-established photovoltaic material possessing excellent electronic properties including an optimal narrow bandgap which theory predicts is matched well to the narrow bandgap materials required for a tandem PEC.[7,24] Earlier studies investigated TiO_2 as a protection layer on a Si photoabsorber and under an amorphous MoS_x (or crystalline MoS_2) as catalyst, but insufficient exposure of MoS_2 HER-active edge sites hindered activity.[25,26] To increase the HER activity, vertically standing 2D-nanosheets of MoS_2 have been deposited on Si protected with an Al_2O_3 layer. Although relatively high saturated photocurrent density (~ 35.6 mA/cm^2) and relatively low onset voltage were achieved (V_{onset} 0.4 V vs. RHE), the low intrinsic HER activity of this MoS_2 polymorph requires high mass loading of catalysts to match up with the underlying high performance Si photoabsorber.[17]

Transition metal phosphide (TMP) catalysts show higher intrinsic HER activity than most non-noble HER catalysts, and a few of them such as Ni_5P_4, and $Fe_{0.5}Co_{0.5}P$ are currently recognized as state-of-the-art HER catalysts. [22,27-30] Nevertheless, few studies have demonstrated active TMP catalysts coupled with silicon light absorbers, mainly due to an unstable catalyst/Si interface. [27,28] Hellstern, *et al.* [31] produced a CoP thin-film on a Si photoabsorber that outperforms MoS_2 on Si photoabsorber for HER. However, the authors noted the formation of

silicon oxide during operation (after 24 hours), indicating the onset of photoabsorber degradation. Commercial applications in viable PEC devices require thousands of hours of durability. [28,29, 31,32] In a different approach, a thin film of cubic-NiP_2 was synthesized on a Ti adhesion layer on top of a silicon photoabosorber.[33] However, this method achieved similar photo/electrocatalytic activity compared to MoS_2 with similar catalyst loading and showed only 6 h of stability.[6,33] Ti does indeed provide good adhesion for the Ni layer,[34] but it is not a suitable diffusion barrier for Si, as seen by intermixing of Ti and Si even at the lowest temperature for catalyst synthesis (300 °C).[35]

To achieve a stable and active TMP catalyst/Si system, an understanding of metal silicide ($NiSi_x$, $CoSi_x$) chemistry is necessary. Metal silicides are conductive materials that have been explored previously for metal contacts in microelectronic devices.[36,37] Although nickel silicides are known as good metallic contacts (resistivity ~15 μΩ·cm), [38] they have two major drawbacks for PEC applications: First, if they become overly thick (> 30 nm) they will decrease transmissivity (T < 50 %), thus reducing the incident photon to H_2 efficiency.[39] Second, they form a native oxide upon air-exposure causing significantly increased junction impedance.[40] Furthermore, silicon diffusion interferes with the conversion of Ni to the nickel phosphide by consumption of the Ni source. Figure 2.1 shows that the relatively low formation temperature of nickel silicide causes it to form at the interface between nickel and silicon.[36,41] Additionally, it was found that an oxide forms on the nickel silicide outer surface layer upon exposure to air. It is therefore clear that introducing a diffusion barrier between the active TMP catalyst and the Si absorber is indispensable to obtain stable interfaces between these desired materials.

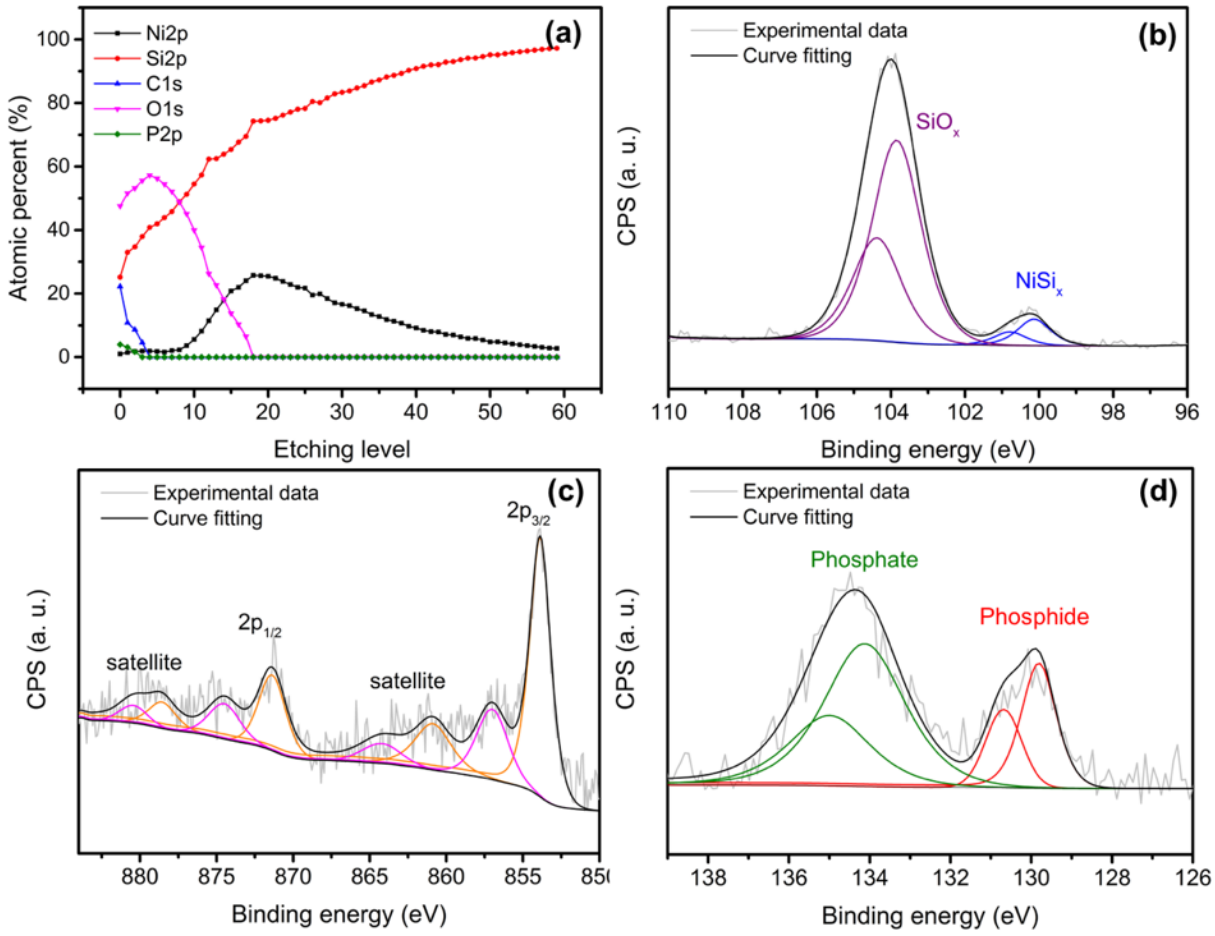

Figure 2.1 XPS analysis for a direct conversion of Ni to the nickel phosphide on a silicon substrate. The depth profile of the $NiP_x/NiSi_x/Si$ is shown in (a). Depth profiles indicate the majority of Ni was consumed to form nickel silicide with a phosphorus-containing surface layer. Si core level spectra (b) of the top layer demonstrates that the nickel silicide is exposed and forms a native oxide. Ni core level spectra (c) have metallic nickel ($NiSi_x/NiP_x$, purple) and NiO_x (orange) features. Similarly, P core level spectra (d) show nickel phosphide (red) and phosphate (green).

Titanium nitride has been well investigated in microelectronic devices due to its unique combination of physical properties, such as high conductivity, corrosion resistance, and extreme hardness. [42] It also has been used effectively as a diffusion barrier on silicon at high temperature because of an extremely low diffusivity of silicon ($\sim 10^{-20}$ m^2/s) — which is an order of magnitude lower than that of TiO_2 at the TMP formation temperature (400 – 600 °C) due to densely packed structure. [43] In the fuel cell research literature, some attempts have also been made to replace the carbon support with TiN due to its high corrosion resistance. [44,45] By contrast, only a few reports have gone on to utilize TiN as a catalyst in the PEC community. [4643] Moreover, none of them have used TiN as a protection layer. The high density of TiN and its low formation energy, [47,48] predicts it as an excellent passivation layer for the Si photoabsorber during HER. Furthermore, the work function of thin-film TiN (4.6 eV) also makes the conduction band minimum of TiN well aligned to degenerately-doped Si, thereby minimizing the junction impedance.

Herein, we report fabrication of a monolithic HER/photocathode junction comprised of cubic-NiP_2 thin-film, supported on a TiN/Si photocathode, with high turnover frequency (TOF), and exceptional stability in acidic media. Diffraction analysis establishes that the c-axis of cubic-NiP_2, deposited as a thin-film, is oriented normal to the interface which, in turn, may contribute to its high TOF. Comparing it to TiO_2, the TiN interfacial layer is demonstrated to be superior for prevention of Si diffusion during high temperature fabrication, creating a low impedance contact possessing high optical transparency, and providing long-term stability. Using this approach to fabricate a photoelectrochemical cell using commercial crystalline Si as

photocathode, the resulting cubic-NiP_2/TiN/Si device produces a photocurrent of 35.9 mA/cm^2 at 0 V vs. RHE under simulated 1.5 AM G illumination.

2.3 Experimental methods

Chemicals. Red P (98.9%, Alfa Aesar), Ni (99.99%, Aldrich), TiN target (99.5%, Kurt Lesker)

Reflectance measurement. All reflectance was measured with Xe arc lamp as a light source and collected by Andor Technology Shamrock SR303i-A imaging spectrometer equipped with Zeiss, Axio Vert.A1 microscope.

The reflectance (R) is plotted by:

$$R = (I_0R - I_b) / (I_0 - I_b)$$

where I_0 is reflected light source intensity from a silver mirror, I_b is background signals, and I_0R is reflected light intensity from the sample. Below 350 nm wavelength, background subtraction overcompensated the reflection signal due to the low incident light source intensity.

To conduct the wet condition measurement similar to a PEC operation condition, a quartz window (1mm thick) placed on the bottom and fixed the sample position 1 mm away from the quartz window to keep the water thickness constant during the measurements.

Pulsed laser deposition of TiN and TiO_2. For TiN deposition, Si (100) substrates were cleaned with acetone and deionized water followed by 5 min in Buffered Oxide Etch (BOE) 6:1vol.

NH_4F/HF prior to introduction into the PLD vacuum chamber. Pulsed laser deposition of TiN and TiO_2 were carried out using a KrF excimer laser Compex 205 (λ = 248 nm d = 7 cm, 10 Hz, 2.5 – 5 J cm^{-2}; Coherent). TiN deposition was carried out under high vacuum condition (5 – 7 × 10^{-4} Pa, 600 °C). For TiO_2, the chamber was pumped down to high vacuum (5 – 7 × 10^{-4} Pa), and deposition was carried out under oxygen partial pressure (P_{O2}: 6.7 Pa) at 300 °C

Thermal evaporation of nickel. To minimize native TiO_x ($x \leq 2$) formation on the TiN layer, a few seconds of BOE etching was performed on the TiN/Si electrode just prior to nickel deposition. Deposition of Ni was carried out at a rate of 1.0 Å/s as determined by quartz crystal microbalance (QCM).

RF sputtering of titanium. Si substrate was cleaned in the same manner as PLD deposition prior to introducing to the sputtering chamber. PVD 75 (Kurt J. Lesker) was used for the sputtering deposition. The chamber was pumped down to 2 – 3 × 10^{-4} Pa and backfilled with Ar and kept at 1.1 Pa during deposition.

Chemical vapor phosphidation. A previous evacuated (1 – 3 × 10^{-3} Pa) and sealed quartz ampoule was heated in a furnace (500 °C, 3 h, +\–8 °C/min). In the ampule, red P (5mg) was loaded with a distance of 6 – 7 cm to the substrate, with bottleneck in-between ensuring the separation.

Faradaic Efficiency Measurement. Hydrogen was quantified on an automated online HP 5890 Series II GC (500 µL sample loop, series connected 6-inch packed HayeSep D + 6-inch packed MoleSieve 13X column, serial TCD + FID detectors, and N_2 carrier gas at 50 °C).

The calibration curve was constructed from constant current electrolysis of water (0.5 M H_2SO_4 electrolyte) in a 3-compartment electrochemical cell using flame-annealed Pt foil as working electrode and IrO_x mesh as counter electrode, separated by a Nafion membrane. Hg/Hg_2SO_4 electrode is used for reference electrode. At steady state, samples of the headspace were taken (averaged, n = 3 at 10-minute intervals). The number of moles of H_2 is calculated using the following equation:

$$n_{H_2}(mol) = \frac{i \times t}{2F}$$

where i is the current in Amps, t is the time necessary to fill the sampling loop ($t = \frac{10\ ml}{min} \times \frac{1\ min}{60\ s} \times \frac{1}{0.5mL}$), and F is Faraday's constant. The calibration curve (area in the chromatogram as a function of hydrogen concentration) was constructed assuming 100% faradaic efficiency for water reduction on platinum at four three currents (linear fit, $R^2 = 0.999$). The faradaic efficiency of the HER for cubic-NiP_2 thin-film on Si and e-Si were measured in a similar fashion at different current (3 mA, and 5 mA, respectively). The value reported corresponds to the average (n = 3) of the headspace hydrogen concentration.

Sequential wet-etching process for uncovering Si solar cell. To protect the bottom Al contact during the etching process, a photoresist (AZ5214) was spin-coated on the back side of the wafer. To remove the Ag bus bar and underlying adhesion layer and Si_3N_4 coatings, Si solar cell wafers were dipped in HF/NH_4F mixture (1:6 buffer oxide etchant) for 30 min. This process will lift off the Ag contact by removing the Si_3N_4 layers and expose Al_2O_3. Al_2O_3 coating was removed by dipping in the concentrated H_3PO_4 at 40 C for 20 min with agitation. After a very short period (5s) of piranha solution, the remaining photoresist layer was removed with acetone. The etched Si solar cell wafer then washed with a copious amount of water and dried with N_2.

Physical characterizations: A cross-sectional STEM sample was prepared by an *in-situ* lift-out method using FEI Helios Nanolab 600 dual beam SEM/FIB at Brookhaven National Laboratory. Amorphous carbon was chosen for the first sacrificial layer. Gallium ions with a fairly low acceleration of 2 KeV were used for final thinning to eliminate surface amorphization and Ga contamination. High angle annular dark field (HAADF) imaging was performed on a Nion UltraSTEM at Rutgers with an accelerating voltage of 60 kV and collecting signal angles above 145 mrad. The microscope is equipped with an aberration corrector, which enables the spatial resolution close to 1 Å. For XPS, a Thermo K-Alpha spectrometer was used with a flood gun for charge compensation. Spectra were calibrated against adventitious carbon (284.8 eV). For time-dependent XPS measurements, X-rays with a spot size of 200 μm were focused on each sample. For depth profiling, sputtering with a 3.5 mm diameter (much larger than the imaged area) was

achieved by Ar sputtering at 1 keV. An X-ray beam with a 35 μm diameter was used every 30 s until only Si was observed indicating that the film was fully etched and the silicon substrate was exposed. Helium ion microscopy was carried out on an Orion Plus Helium Ion Microscope (Carl Zeiss) operating at a 30 kV acceleration voltage and an ion beam current around 1 pA. Atomic force microscopy (AFM) images were taken using a Park Systems (Suwon, Korea) NX-10 with a Nanosensor (Neuchatel, Switzerland) PPP-NCHR tip in non-contact mode at room temperature. Rutherford backscattering spectrometry (RBS) was performed using a 2 MeV He^{2+} beam source from the Rutgers University tandem accelerator. The incident beam was normal to the surface and the backscattered He ions were collected by silicon detectors at a 163° back-scattering angle. Data fitting and modeling were accomplished using the SIMNRA 6.06 software package. The theoretical densities were taken from the appropriate crystal structures (NiP_2 PDF 01-073-0436, TiN 01-087-0633 and $Ni_3(PO_4)_2$ 01-072-3977).

Electrode assembly: The method for electrode assembly was adopted from elsewhere. [66] An electrical contact of the prepared electrodes was made on the back side of the silicon substrate scoring in the presence of a Ga-In eutectic (99.99% Aldrich). A copper or zirconium wire was attached to the eutectic with conductive silver paint (SPI supplies). The wire was then inserted into a Pyrex glass tube. The back side of the electrode were finally sealed with a mixture of epoxy resin (Loctite Hysol 1C) and TiO_2 nanoparticle (p25, Evonik). Electrode areas were measured with a digital photograph and ImageJ analysis. Typical electrode areas ranged between 0.1 – 0.3 cm^2.

Photoelectrochemical measurements: Photoelectrochemical measurements were performed in a custom built three-electrode glass cell in H_2 purged 0.5 M H_2SO_4 using a Bio-logic potentiostat (SP-150). The working electrodes were illuminated by simulated 1.5 AM G illumination (AM1.5G, 100 mW/cm^2) supplied by a 75 W Xe arc lamp (ORIEL) through a quartz viewport in the cell. The photoelectrode (working electrode) locates 5 mm away from the quartz viewport. For counter and reference electrode, a boron-doped diamond electrode (Element Six, Da Beers) and mercury/mercury sulfate reference electrode (single junction Hg/Hg_2SO_4, PINE Instruments) were used. We used anion exchange membrane (FKS, Fumatech) compartments (membrane attached quartz tubes) on both reference and counter electrodes to minimize the cross-contamination. The reference electrode potential was calibrated against the reversible hydrogen electrode (RHE, Pt electrode at 1 atm. H_2) before each measurement. All J-V curves are obtained by averaged cyclic voltammograms at the scan rate of 10 mV/s.

IPCE measurement: Measurements were performed using monochromated light from a 1000 W Xe arc lamp (Oriel) light source. The wavelength of light was selected by a monochromator (Horiba) and ranged from 400 nm to 900 nm at 50 nm intervals except for 840 nm which replaced 850 nm due to a spike in the light source intensity. The working electrode was held at 0.0 V vs. RHE using Biologic potentiostat and the measured photocurrent was derived as the difference between the dark and illuminated current values.

2.4 Results and discussions

Investigations of optical properties, structures, interfaces and surface morphologies

The fabrication process to make the NiP_2/TiN/n^+p-Si is summarized as follows (Figure 2.2a): First, a n^+p-Si buried PV junction was creating a degenerately phosphorous-doped surface on a p-type Si (100) wafer. A high-quality TiN/n^+p-Si structure with a sharp interface was created by pulsed laser deposition (PLD). 3 nm of nickel (Ni) was then thermally evaporated on top of TiN, followed by thermal phosphidation using red-P for synthesis of cubic-NiP_2 (See detailed procedure in Methods). A schematic description of the full photocathode and its absolute conduction band energies aids in understanding carrier transport in the device (Figure 2.2b).[49,50] To optimize the TiN film thickness and reveal its optical properties, varying thicknesses of TiN films were prepared on quartz substrates. Although the quartz substrate has different refractive index than Si, it allows unobstructed observation of the optical properties of TiN.

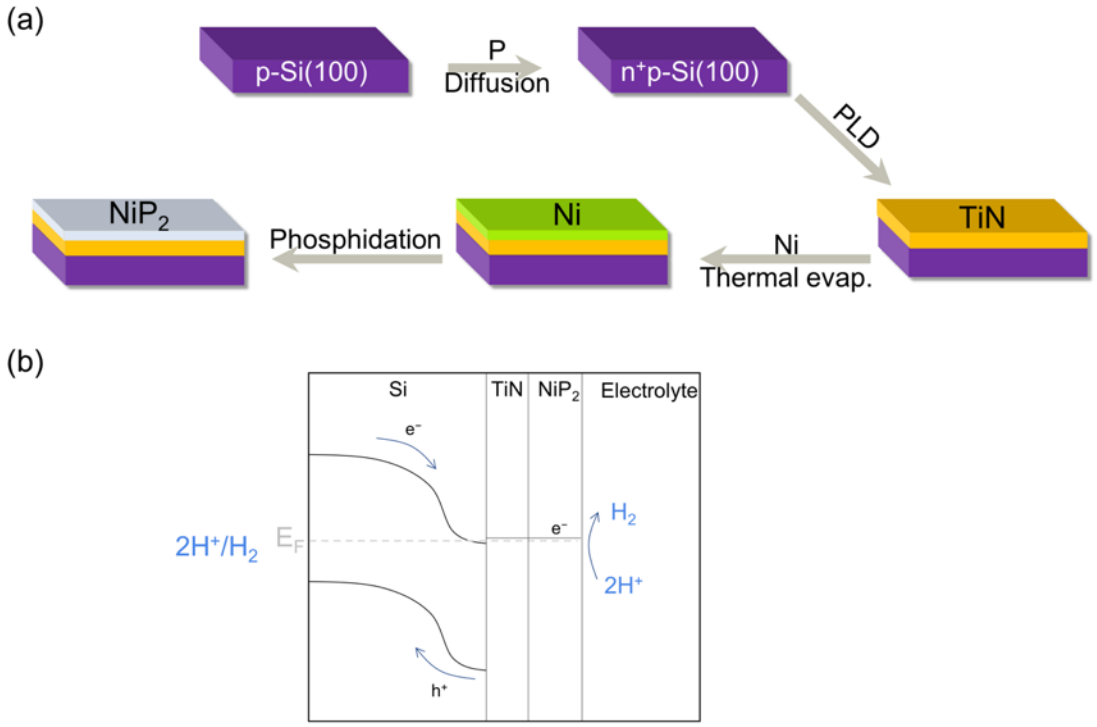

Figure 2.2 Schematic illustration of (a) NiP_2/TiN/n^+p-Si photocathode fabrication and (b) their band structure. (Band structure were reconstructed based on references 49, and 50)

In Figure 2.3, the spectra show a linear loss of transmittance as a function of thickness; films thicker than 6 nm reduce the transmittance to below 65%. When the deposited TiN layer is thinner than 4 nm, film conformality is an issue with random pinholes appearing, and therefore might not be able to serve as an adequate diffusion barrier (data not shown). At wavelengths above 380 nm, the measured transmittance of 4 nm TiN film on quartz is around 70%. However, to obtain the contribution only from absorption, we also measured the reflectance of 4 nm TiN on quartz and plotted it along with the absorptance and transmittance as a function of

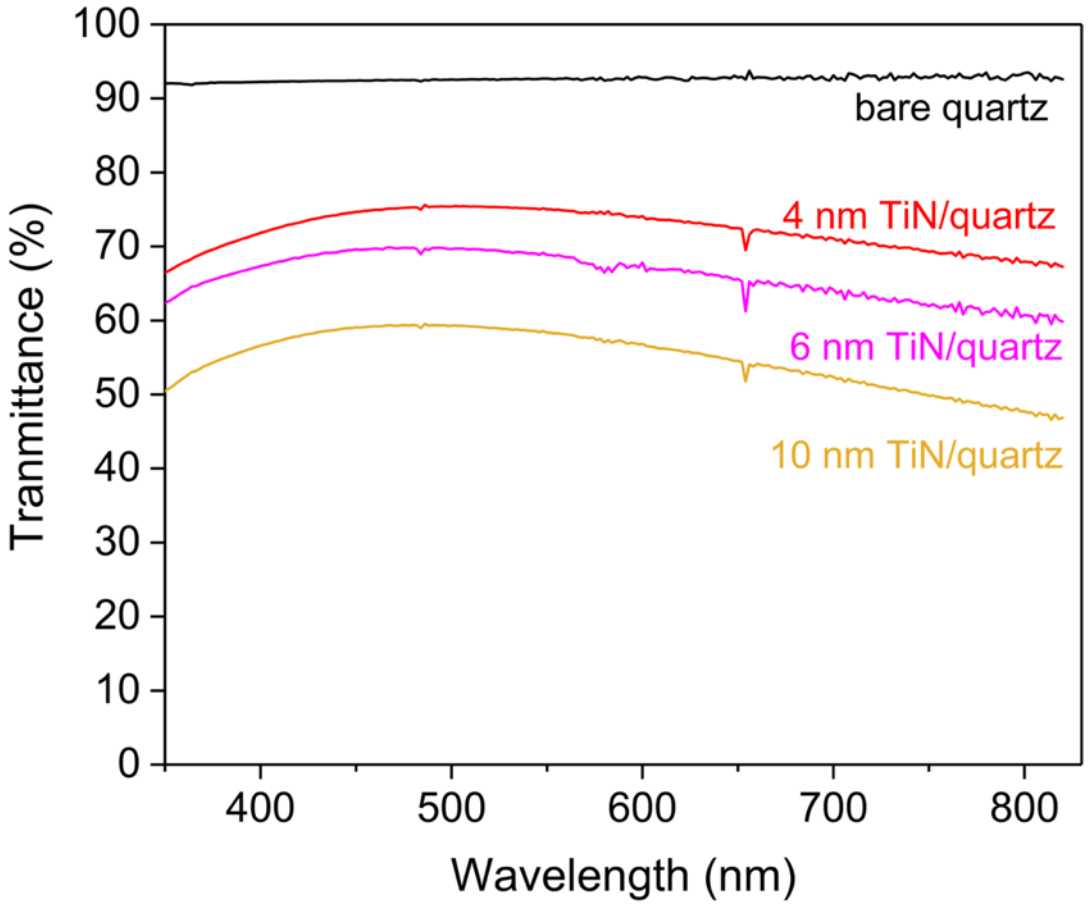

Figure 2.3 Transmittance spectrum of different thicknesses of TiN film deposited on a quartz substrate. The loss of transmittance from quartz substrate is due to the reflectance which also contributes to all other TiN coated samples.

wavelength. (Figure 2.4). The absorptance of 4 nm TiN at a given wavelength ranges between 15 and 20%, with an estimated absorption coefficient of 5.2×10^5 cm^{-1} (at 500 nm). To further investigate the influence of the TiN film on total reflectance during operation, the reflectance of bare Si as well as 4 nm of TiN-coated Si were measured in dry (PV, in air) and wet conditions (PEC, with 1mm thick quartz window and 1 mm water layer) (Figure 2.5a). The TiN coating

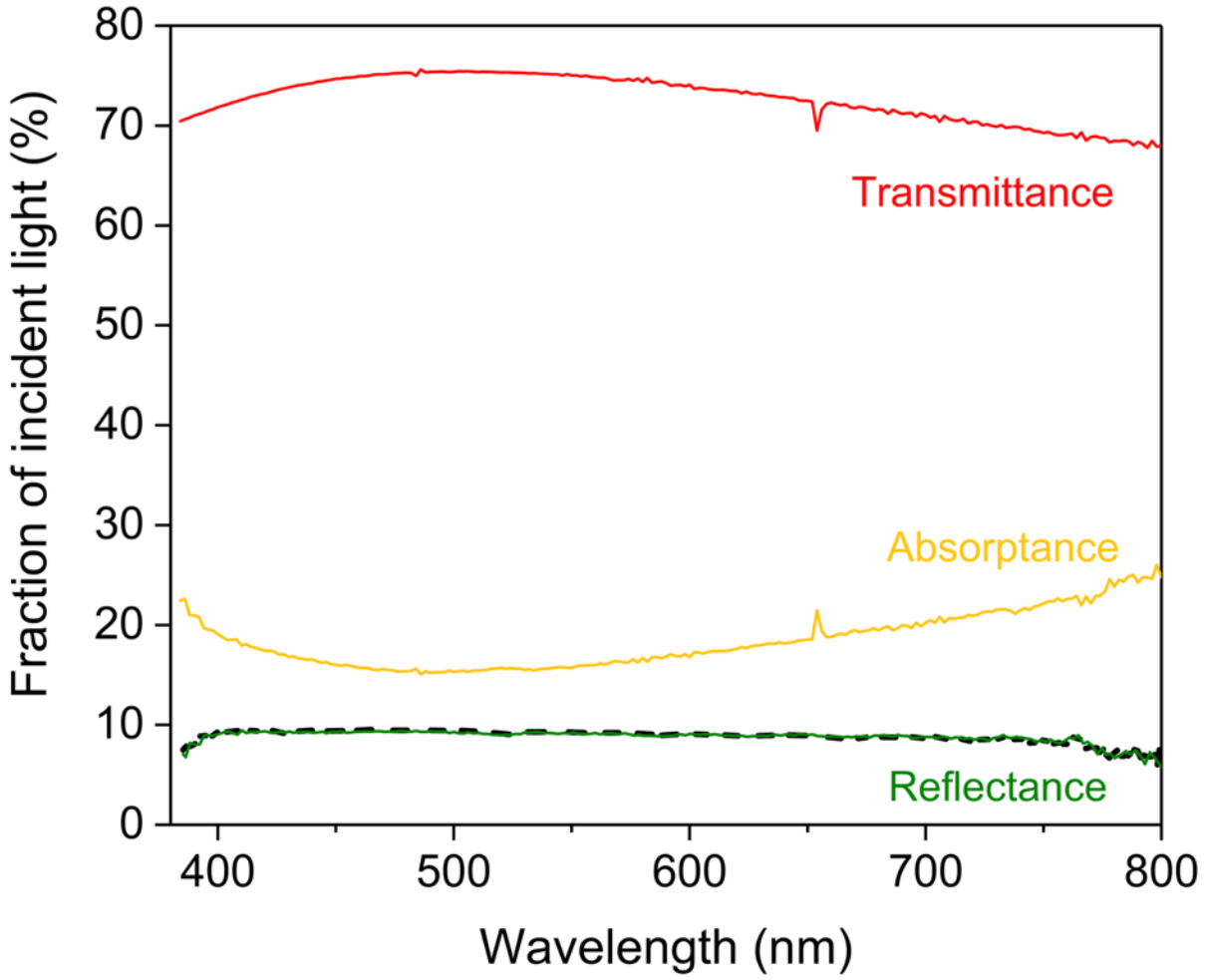

Figure 2.4 Optical transmittance, absorptance, and reflectance of 4 nm TiN coated on a quartz substrate. Since TiN layer is atomically smooth, scattering contribution is negligible. The black dash line is the reflectance of bare quartz which is the sum of contribution from top air/quartz and bottom quartz/air interfaces.

causes a very small change in total reflectance (1-2% decrease) in both dry and wet conditions. By contrast, there is a significant decrease in reflectance on going from dry to wet conditions for both bare and TiN-coated Si. As shown, this decreases 13-23% over the spectral range 400 -900

nm. These results indicate that the quartz window and water layers substantially decreases the reflectance, which is well reproduced by calculations based on the Fresnel equations.[51] (Figure 2.5b) These opposing contributions offset one another and could possibly increase the light intensity that reaches Si when measured in the PEC configuration, as compared to bare Si PV alone.

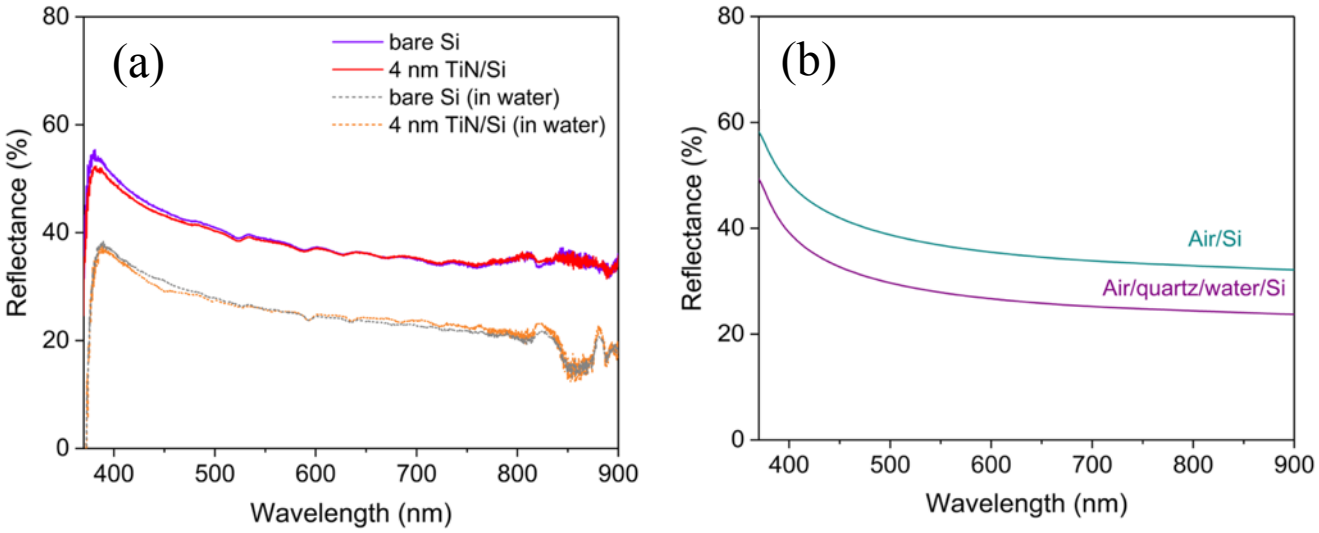

Figure 2.5 Reflectance of (a) bare Si and 4 nm TiN coated Si in air and with 1mm thick water layer. Calculated reflectance of air/Si vs. air/1mm quartz/1 mm water/Si based on the complex-matrix form of Fresnel equations.[51] The small discrepancy between the experimental data and calculation might be attributed to the finite collection angle of objective lens during reflectance measurements and unconsidered Si conductivity in the calculation.

Film properties and interfaces of the Si photoabsorber device were probed using cross-sectional scanning transmission electron microscopy (STEM), Rutherford backscattering spectrometry (RBS), and X-ray photoelectron spectroscopy (XPS, depth profile by Ar^{+}) (Figure

2.6). The cross-sectional STEM high-angle annular dark-field (HAADF) image of the as-deposited NiP_2/TiN/n^+p-Si sample verifies uniform deposition of TiN and NiP_2 with clear edges (Figure 2.6a). This confirms that the 4 nm thick TiN layer is indeed a good diffusion barrier for Si, allowing the formation of nickel phosphide without intermixing of Ni and Si during the high-temperature phosphidation. The high magnification STEM image (Figure 2.6b) reveals that the TiN layer appears to be overall polycrystalline, in-line with a previous report. [42] The high-resolution image of the NiP_2 top layer (Figure 2.6c) shows atomic-scale resolution of NiP_2 growth along the (001) plane. The Fast Fourier Transformed (FFT) STEM image of the large NiP_2 grain (Figure 2.6c, upper inset) reveals the reciprocal space diffraction pattern. This pattern can be assigned to the [100] zone axis of cubic-NiP_2, thus demonstrating that synthesis formed nano-crystalline cubic-NiP_2. Other NiP_2 grains are matched with a [110] or [210] projection view, grown along the c-axis (normal to the surface). X-ray diffraction of a thicker film (>200 nm), indicates the bulk structure is polycrystalline cubic NiP_2 (Figure 2.7), suggesting that the as-prepared thin-film is partially oriented due to kinetic trapping of the polycrystalline product.

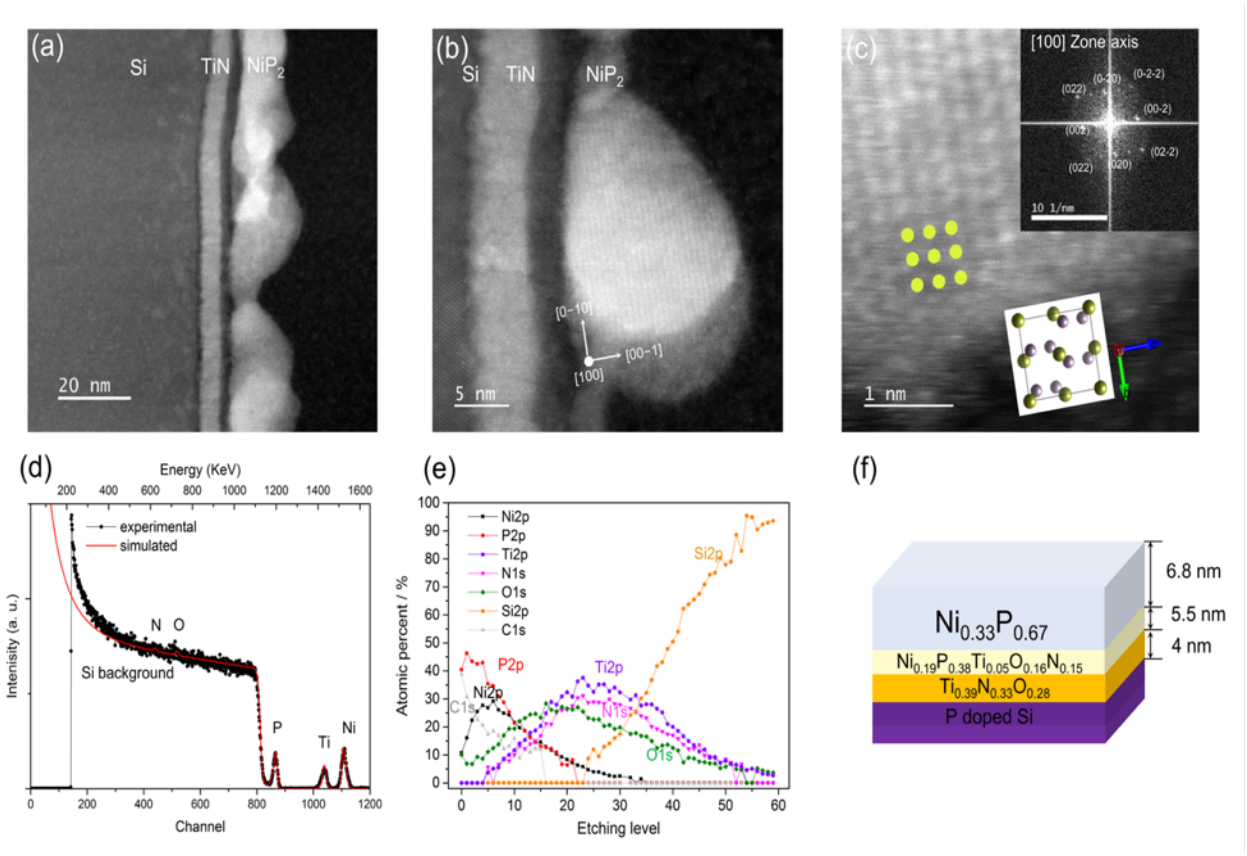

Figure 2.6 Structure and chemical analysis NiP_2/TiN/n^+p-Si photocathode. (a) Cross-sectional STEM high-angle annular dark-field (HAADF) low-magnification image of NiP_2/TiN/n^+p-Si, (b) high-magnification image of device interfaces and (c) atomic resolution image of cubic NiP_2. (Yellow is nickel, and purple is phosphorous) Inset shows FFT pattern of NiP_2 which is well matched with the [100] zone axis of cubic NiP_2. (d) RBS spectrum of NiP_2/TiN/n^+p-Si. (e) XPS depth profile of NiP_2/TiN/n^+p-Si (f) Thickness and chemical profiles of photocathode device based on RBS spectrum and XPS depth profile.

Both RBS and XPS were used to measure the thickness, the interfacial homogeneity, and the elemental composition as a function of depth of each layer (Figure 2.6d-f). The simulated RBS

spectrum indicates that the composition of the top layer is $Ni_{0.33}P_{0.67}$ and contains 5.0×10^{16} atoms/cm^2, which corresponds to a thickness of 6.8 nm when calculated using the theoretical

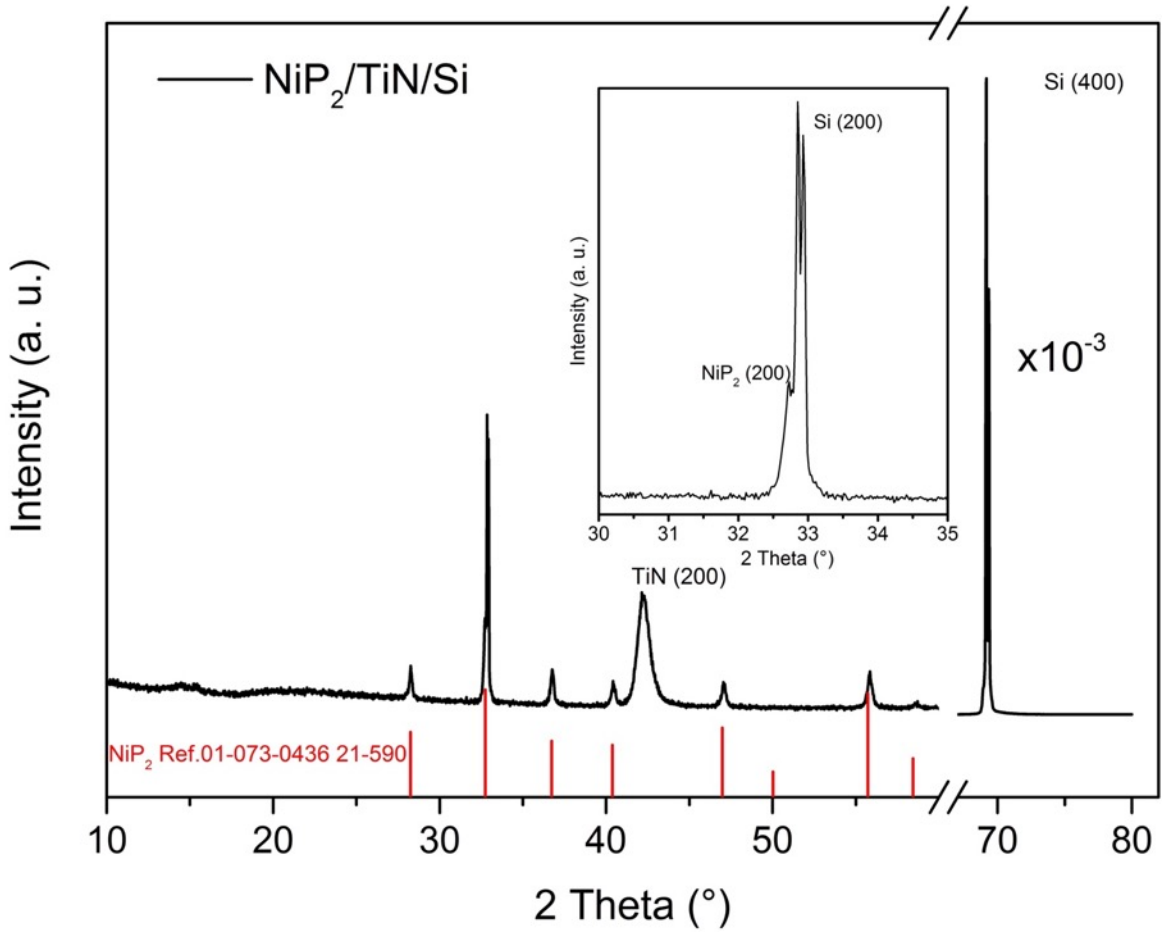

Figure 2.7 X-ray diffraction pattern of NiP_2/TiN/Si. 50 nm TiN was deposited by PLD on a fresh, BOE-etched Si substrate followed by a 150 nm Ni deposition, which was subsequently converted to NiP_2 though the P CVD step described in the main text. TiN only shows a reflection (200) at 42.2 °. A strong reflection of Si (200) and (400) are obtained at 32.8° and 69.1°, respectively. All other reflections are matched with the cubic NiP_2 reference, indicating our synthesis method forms phase-pure cubic NiP_2.

density. The thickness obtained from the RBS simulation is an average over the roughness of cubic NiP_2. The latter is evident in the cross-sectional TEM results (Figure 2.6a-b).

Titanium nitride, in the next layer down, has an average composition and areal density corresponding to $Ti_{0.39}N_{0.33}O_{0.27}$ and 4.2×10^{16} atoms/cm^2. The estimated thickness is 4.0 nm (using the TiN density), similar to the cross-sectional TEM image result, which further shows it has uniform thickness (Figure 2.6a). The ~25% oxygen content of the TiN layer is likely caused by the high temperature of the deposition in a less than perfect vacuum ($4\text{-}7 \times 10^{-4}$ Pa) and limited depth resolution. An interfacial region between TiN and NiP_2 can be seen in the cross sectional TEM image (Figure 2.6a), as the dark layer (low atomic mass) of thickness 2.2 nm (5.5 nm by RBS simulation). This layer has an average composition of $Ni_{0.2}P_{0.39}Ti_{0.05}O_{0.18}N_{0.2}$ and is formed during phosphidation, where Ni and P diffuse into the TiO_x-TiN layer.

XPS depth profiling was also used to investigate the TiN/Si interface (Figure 2.6e), which is seen in TEM to exhibit a clean boundary with the TiN layer. When performed just prior to deposition, the buffered oxide etchant cleaning steps remove silicon oxide from Si, that could increase the ohmic loss at this junction.[49,52] XPS spectra of the Si core level as a function of sputtering time (Figure 2.8) proves that the Si does not contain an oxide impurity.

To evaluate the necessity of the TiN interfacial layer, we fabricated two control samples: 1) nickel phosphide thin-film directly on Si substrate (identical synthesis as Figure 1a, but with the TiN layer absent) and 2) replace the TiN interfacial layer with TiO_2. For the TiO_2 interfacial layer, a thin Ti layer (3 nm) was sputtered on clean Si prior to TiO_2 thin-film deposition (2.5 nm). This Ti layer consumes oxygen to prevent SiO_x formation at the TiO_2 and Si interface.[53]

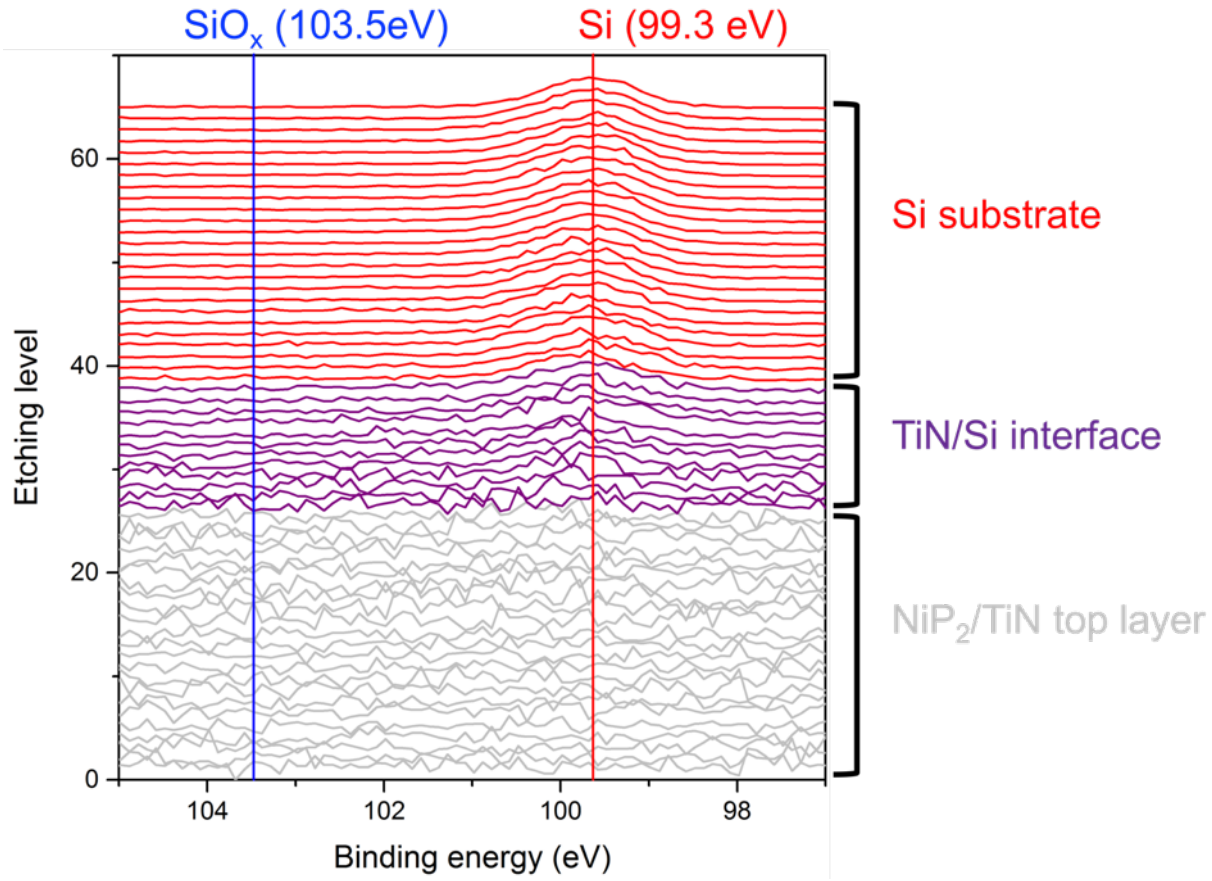

Figure 2.8 XPS depth profile of Si core level spectra on NiP_2/TiN/n^+p-Si photocathode. The intensity of all Si core level spectra was normalized to 1. From the top layer of NiP_2 to the TiN layer, no silicon signals are detected (gray). At the TiN/Si interface (purple), Si signals start to appear at 99.3 eV (red vertical line), which is corresponds to a Si substrate contribution. The Si signal becomes more pronounced as more layers are etched. During the profiling, SiO_x signals were not observed (blue vertical line). It is worth noting that the selected Ar^+ sputtering condition etches the film at less than 1 nm/cycle, therefore it has adequate resolution to detect native oxide from silicon.

TiO_2 was deposited by PLD to allow direct comparison with TiN prepared the same way. The

depth profile (Figure 2.1) of phosphodized nickel film on Si without a passivation layer shows that interdiffusion occurs and almost all of the Ni reacts with Si to form nickel silicide.

A small amount of nickel phosphide is formed only at the very top layer. XPS core level spectra of the top surface (Figure 2.1b) shows the formation of a silicate layer (in addition to the nickel phosphide) that may be the surface oxide of the nickel silicide. In the case of the TiO_2 interfacial layer, the depth profile (Figure 2.9a) shows that nickel phosphide forms at the top, but it has slightly earlier onset of Si compared to that of TiN. When compared with a pristine TiO_2/Ti/Si interface (Figure 2.9b), the amount of oxygen in the TiO_2 layer is also decreased. These results indicate that diffusion of Si and O occurs and can form either $TiSi_x$ or SiO_x at the interface between TiO_2 and Si. These two control samples demonstrate that without a TiN interfacial layer, atomic diffusion occurs across the interface which can be detrimental for other performance metrics. The J-V performance of these half-cell devices is described in the PEC section.

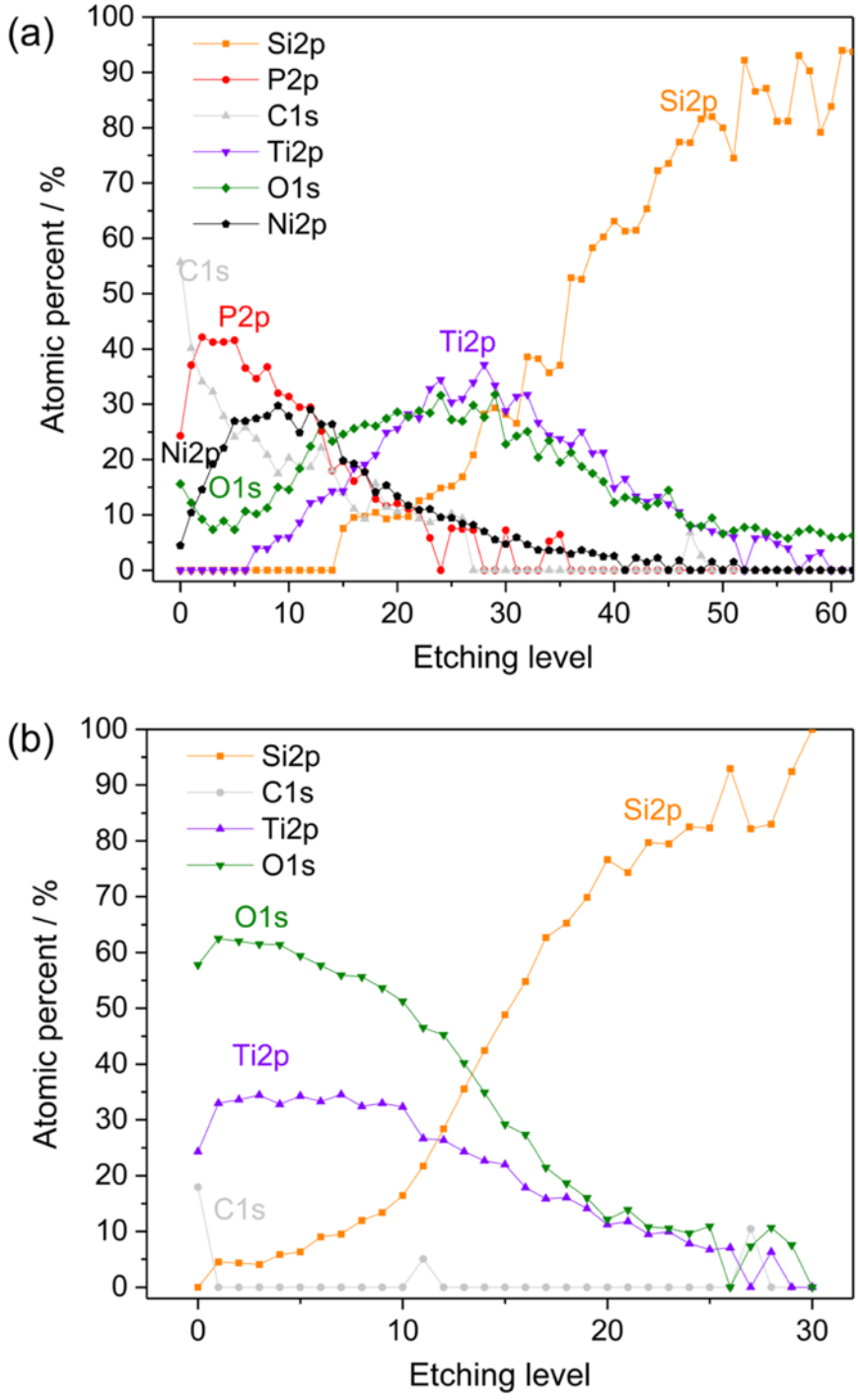

Figure 2.9 XPS depth profile of a) $NiP_2/TiO_2/Ti/n^+p$-Si and b) pristine $TiO_2/Ti/n^+p$-Si photocathode.

To examine the surface morphology of the top catalyst layer of the TiN-protected photocathode, we used a helium ion microscope (HIM) for imaging (Figure 2.10a). [5451] This reveals uniform grains of cubic-NiP_2 with 20 – 30 nm width and 50 – 150 nm length of the individual grains with gaps in between grains. Atomic force microscope (AFM) imaging (Figure 2.10b) reveals additional vertical information.

The AFM image and line profile indicate a thickness variation of the film from 4 nm to 20 nm. Both the HIM and AFM images indicate the conversion from Ni to c-NiP_2 causes the expansion of grains due to the density difference (Ni: 8.9 g/cm^3, c-NiP_2 4.89 g/cm^3), resulting in thickness variation by creating nanometer-scale gaps between grains. Topological information obtained

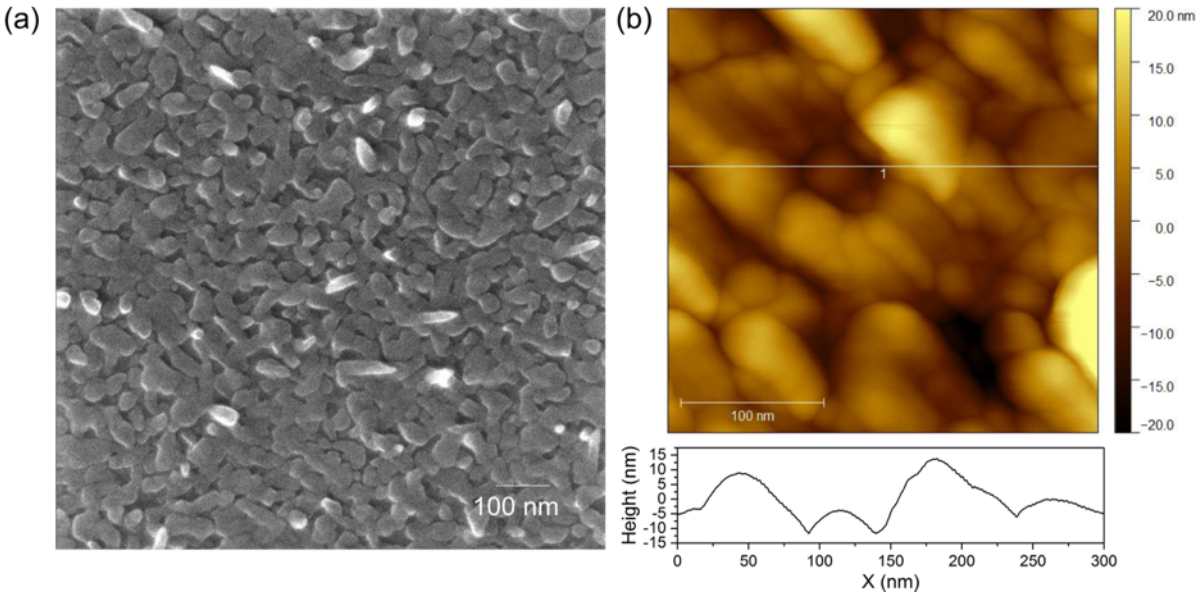

Figure 2.10 Morphologies of thin-film NiP2 catalyst. (a) NiP2 top layer of Helium ion microscope image and (b) AFM image. The bottom of AFM image indicates line profile (line 1). The film has uniform coating but having thickness variation (4-20 nm). Roughness is Rrms = 6.7 nm.

from AFM is also helpful in understanding the true surface area of catalysts. The roughness factor from a larger area (5 × 5 μm) of the AFM profile (Figure 2.11a) is used to evaluate the turnover frequency (TOF) of the cubic-NiP_2 thin-film and compare it with other state-of-the-art catalysts below.

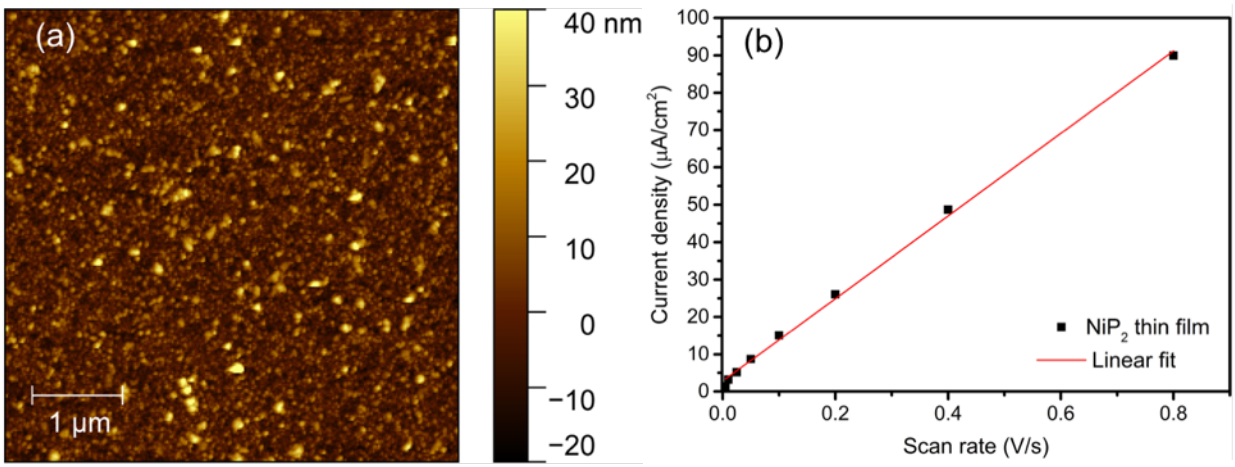

Figure 2.11 Determination of electrochemical surface area. A 5×5 μm atomic force microscope image **(a)** of $NiP_2/TiN/n^+Si$ shows a smooth film. The roughness factor is 1.08 cm^2_{ECSA}/cm^2_{geo}. The capacitive current as a function of scan rate **(b)** and the electrochemical capacitive currents were measured using cyclic voltammograms at 0.1 V vs. RHE where no faradaic processes occur. The intrinsic capacitance of the NiP_2 thin-film is 110 μF cm^{-2}. We assume 40 μF cm^{-2} as a flat surface, the same assumption used by Kibsgaard *et al*[30] allowing for direct comparison to literature values. Roughness factor from the intrinsic capacitance measurement is 2.75 cm^2_{ECSA}/cm^2_{geo}.

Thin-film cubic-NiP_2 catalyst HER activity

The HER activity of the thin-film cubic-NiP_2 catalyst was evaluated on n^+-Si (resistivity 0.005 ohm/cm – 10^{19-20} doping level, University Wafer) as the substrate (fabricated using the same procedure described above). All the electrochemical HER measurements are conducted using a three-electrode cell with 0.5 M sulfuric acid electrolyte. A boron-doped diamond counter electrode (Element Six, Da Beers) and mercury/mercury sulfate reference electrode (single junction Hg/Hg_2SO_4, PINE Instruments) were used. The reference electrode potential was calibrated against the reversible hydrogen electrode (RHE, Pt electrode at 1 atm H_2) before each measurement. To minimize contamination (by Cu^{2+} (from electrical leads) or Hg^{2+} (from the reference electrode)), we used anion exchange membrane (FKS, Fumatech) compartments on both reference and counter electrodes. Electrochemical impedance spectroscopy measurements were conducted to estimate the uncompensated solution resistance (Figure 2.12). To reduce the surface oxide that forms during air exposure, a negative bias was applied to achieve a current density of −10 mA/cm^2 for 10 min before the cyclic voltammetry. Figure 2.13 shows IR-corrected and averaged cyclic voltammograms of cubic-NiP_2 thin-film catalyst, c-NiP_2/TiN/n^+-Si and a benchmark (polycrystalline Pt foil) reveals that the potential required to obtain −10 mA/cm^2 is 167 mV (vs. RHE) and 31 mV for thin-film cubic-NiP_2 catalyst and the benchmark, respectively. The cubic-NiP_2 thin-film catalyst generated H_2 with 100% Faradaic efficiency (Figure 2.14). The applied potential plotted as a function of the logarithm of the current density derived from linear sweep voltammetry (Figure 2.15) indicates a Tafel slope and exchange current density of 41 mV/dec, and 3.0×10^{-6} A/cm$^2_{geo}$, respectively. In order to minimize capacitive charging effects on the Tafel slope, we also measured the steady-state current during

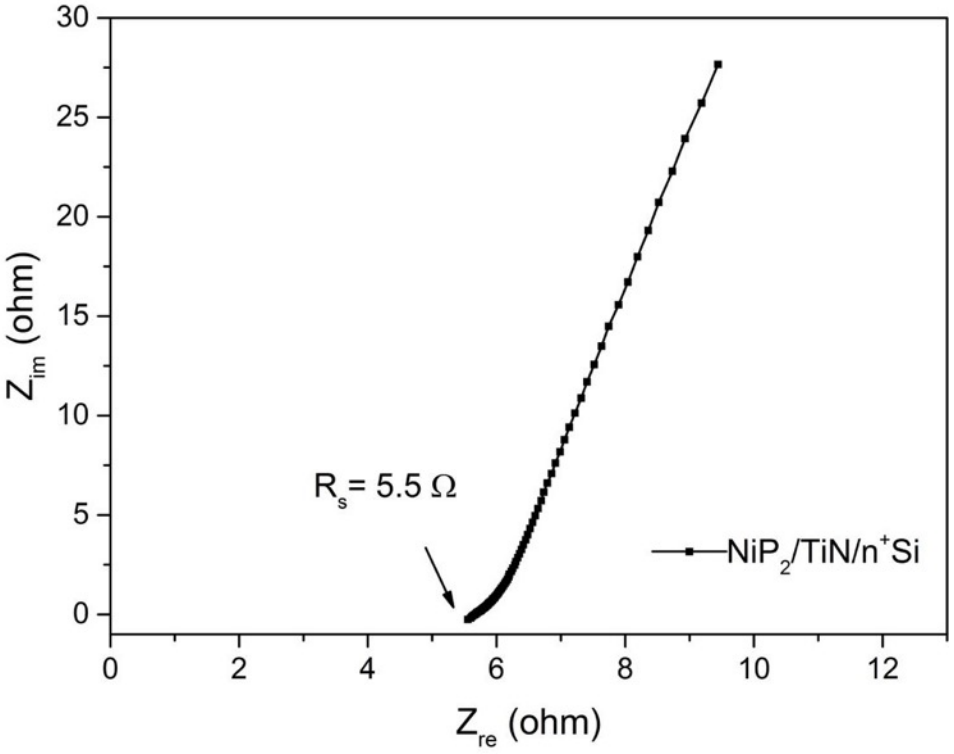

Figure 2.12 Electrochemical impedance spectroscopy (EIS) of the NiP_2 thin-film. Before each CV measurement, EIS was carried out to obtain the solution resistance (R_s), which is used for the *i*R correction. The average R_s obtained was 5.6 ± 0.6 Ω.

chronoamperometry (CA) at various fixed potentials, which gave a Tafel slope of 40 mV/dec (Figure 2.15). The two methods give the same result indicating there is negligible capacitive charging of the thin-film cubic-NiP_2, presumably due to its low roughness factor. The obtained Tafel slope is 20-32% lower than both thick (51 mV/dec) and thin-film (61 mV/dec) polycrystalline cubic-NiP_2 electrocatalysts reported by others.[33,55] This value of the Tafel slope indicates that the Volmer-Heyrovsky mechanism is the likely rate-determining step for HER.[56]

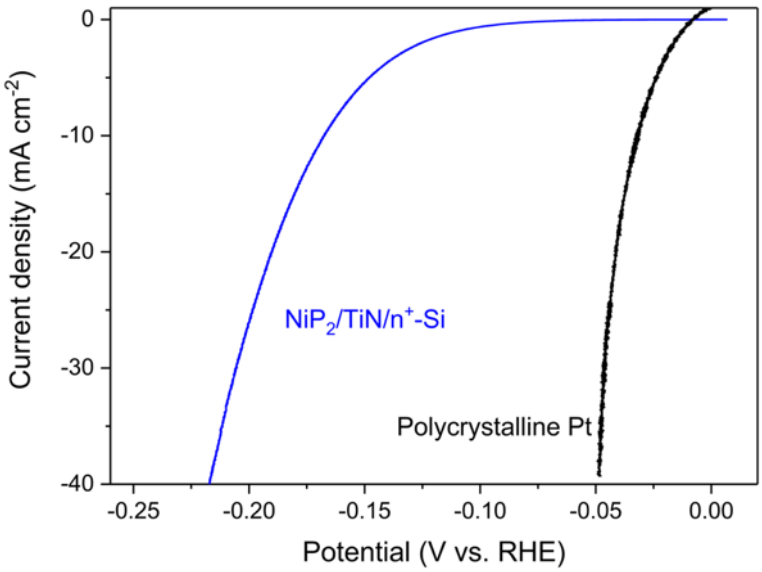

Figure 2.13 Electrochemical activity of thin-film NiP_2 catalyst. IR-corrected averaged cyclic voltammograms (CV) of the NiP_2 thin-film catalyst (NiP_2/TiN/n^+-Si, blue) and polycrystalline Pt (black) for benchmark.

This lower Tafel slope indicates that our thin-film catalyst method produces a better HER efficiency using NiP_2 than other reported methods so far. For comparison, TMP thin-film catalysts (< 50 nm), such as CoP and Ni_2P on Si substrate have overpotentials of 202 mV and 240 mV (vs. RHE) at a current density of −10 mA/cm^2_{geo} based on the geometric surface area, while their Tafel slope is 60 mV/dec and 66 mV/dec, respectively. [28,31,34] This comparison shows that our method for producing cubic-NiP_2 thin-film catalyst on TiN/Si has the highest reported HER activity amongst all thin-film TMP catalysts reported thus far, to our knowledge.

To determine the turnover frequency (TOF) and allow direct comparison of the intrinsic activity of catalysts, the number of active sites is required. Here, we estimated the TOF by

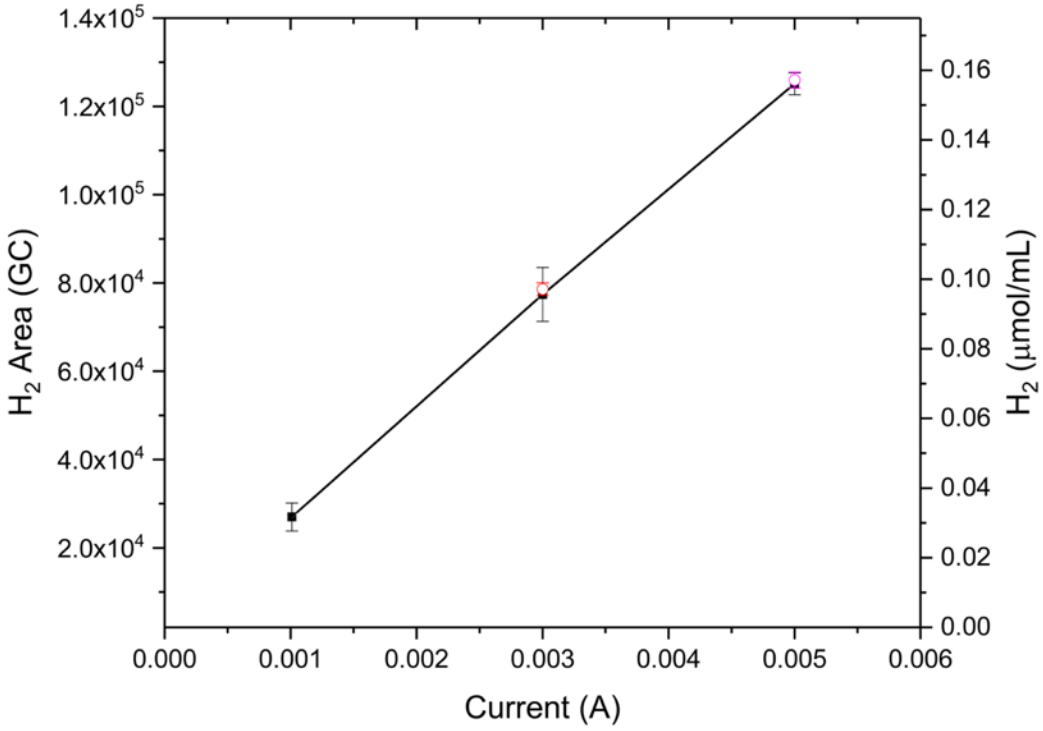

Figure 2.14 Faradaic efficiency test. The linear line is the calibration curve measured by the Pt foil benchmark. Red circle (○) and magenta circle (○) correspond to cubic-NiP_2/TiN layers on n^+-Si and e-Si, respectively. Both samples overlapped the Pt benchmark within the error bars.

electrochemical surface area (ECSA), using the method of Kibsgaard, *et al.* (Figure 2.11b).[27,30] Application of this method yields a TOF of 0.41 H_2 site^{-1} s^{-1} for cubic-NiP_2 thin-films at E= −100mV vs RHE (see detailed calculation in electronic supplementary information). This compares very well with TOFs from other studies of powder-based TMP catalysts, [22,30] summarized in Figure 2.16. For example, the TOF of these thin-films is 1-order of magnitude smaller than that of Ni_5P_4 nanocrystalline-micron particles (3.5 s^{-1} TOF; the best known HER catalyst after Pt) and on par with $Fe_{0.5}Co_{0.5}P$ (0.19 s^{-1} TOF). [22,30]

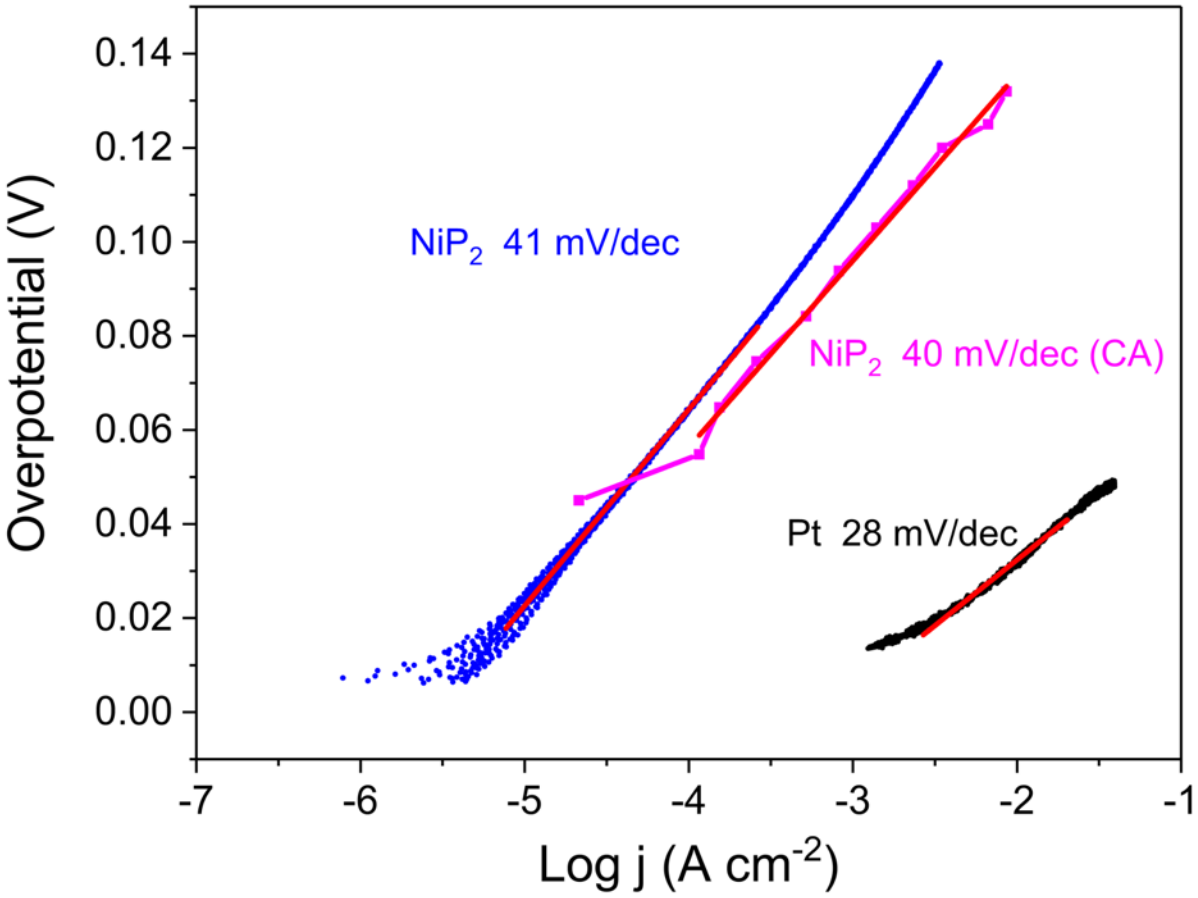

Figure 2.15 Tafel analysis of NiP_2 thin-film and polycrystalline Pt foil as a reference. The Tafel slope and the exchange current density of NiP_2 thin-film catalyst are 41 mV/dec and 3.0 $\times 10^{-6}$ A/cm$^2_{geo}$, respectively. The magenta curve corresponds to the Tafel slope of the NiP_2 thin-film catalyst measured by chronoamperometry at different fixed potentials. For reference, the Tafel slope and exchange current density of a polycrystalline Pt foil were also measured (28 mV/dec and 3.2 $\times 10^{-4}$ A/cm$^2_{geo}$, respectively).

We also estimated the surface area using an AFM image-derived roughness factor (Figure

2.11a), as demonstrated by Hellestern, *et al.* for a thin-film TMP catalyst [31] The obtained roughness factor of thin-film NiP_2 is 1.08 cm^2_{ECSA}/cm^2_{geo}, assuming an average Ni and P surface coverage (i.e. assuming both are active sites) a TOF of 1.04 H_2 $site^{-1}$ s^{-1} is obtained. This estimate points to cubic-NiP_2 as the second most active TMP catalyst reported. This difference could be due to either the ECSA estimate exaggerating the surface area because of a pseudo-capacitance contribution, or conversely, the AFM surface roughness under estimating the true surface area due to small porosity not resolved by AFM (the surface between the agglomerated particles, as seen by STEM in Figure 2.6b).

The low Tafel slope, and exceptional TOF of our cubic-NiP_2 thin-film catalyst, may be attributed to the preferred facet orientation of NiP_2 (001), revealed in the STEM cross-section. The assumption is that this preferentially exposes a higher activity facet compared to a random distribution of orientations (polycrystalline). Conversely, other factors such as a limited mass transport and inaccurate ECSA measurement for thicker films may influence the accuracy of the TOF estimate.

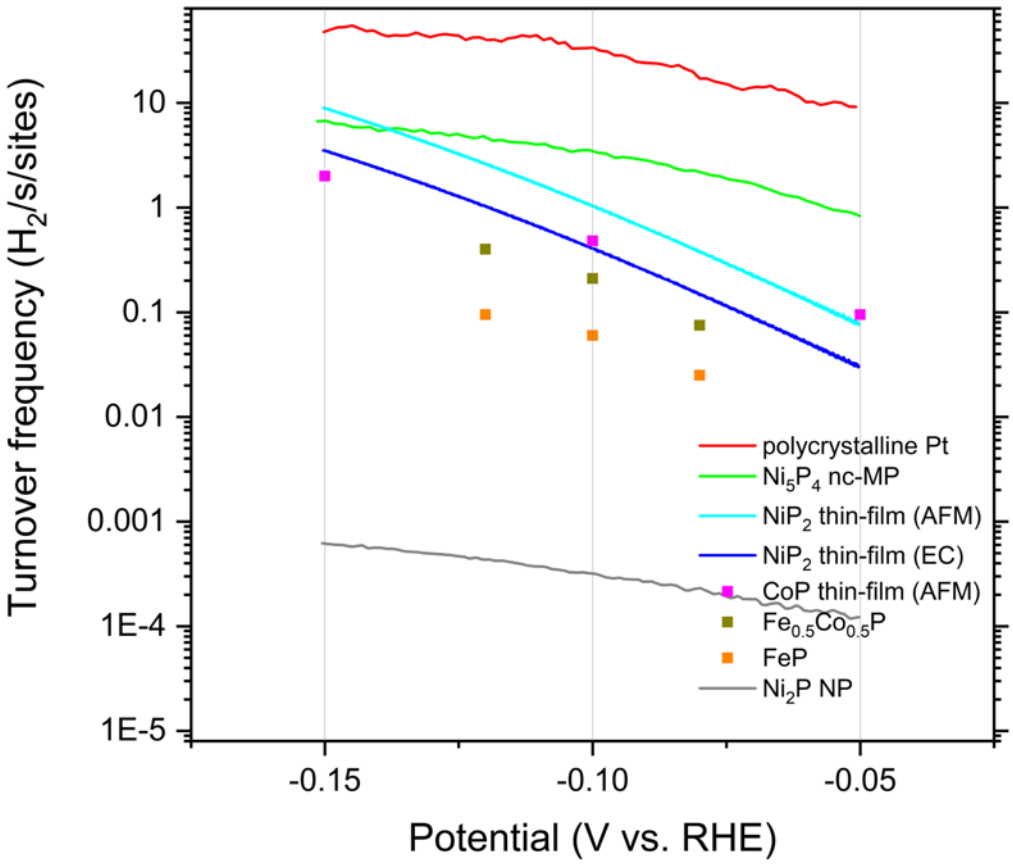

Figure 2.16 TOF comparison of selected transition metal phosphide and the NiP_2 thin-film. TOF of NiP_2 thin-film (EC) is calculated based on ECSA using the methods of Kibsgaard *et al*[31] which used intrinsic capacitance for the determination of electrochemical surface area. For the comparison, TOFs (calculated using the same method described above) of the reported $Fe_{0.5}C_{0.5}P$ and FeP are shown. TOF of the NiP_2 thin-film (AFM) is calculated based on ECSA using the method reported by Hellestern *et al.*[31] A TOF of the CoP thin-film, calculated based on AFM, is also shown for comparison. Furthermore, other TMP catalysts (Ni_2P, Ni_5P_4) and Pt are included for reference.[12]

Photoelectrochemical activity

To estimate the maximum saturation photocurrent and photovoltage of NiP_2/TiN/n^+p-Si, we first probed the photovoltaic properties (short circuit current density, J_{sc} and open-circuit potential, V_{oc}) of bare n^+p-Si (Figure 2.17). Note that the PV properties are lower (J_{sc} ~ 16.3 mA/cm^2 and V_{oc} ~ 525 mV) than a fully optimized commercial Si solar cell (J_{sc} ~ 40 mA/cm^2 and V_{oc} ~ 727 mV) due to the absence of a pp^+ junction, and top anti-reflective and bottom reflective coatings. [57] To determine the influence of the NiP_2 and TiN layers and the alternative TiO_2 interfacial layer, 4 devices were prepared and compared: TiN/n^+p-Si, NiP_x/$NiSi_y$/n^+p-Si (same as Figure 2.1), NiP_2/TiO_2/Ti/n^+p-Si (same as Figure 2.9a), and Pt/TiN/n^+p-Si (benchmark). The benchmark device was fabricated by drop-casting and electroreduction to form nanoparticles of Pt on TiN/n^+p-Si, similar to the method described Chorkendorff and co-workers. [25] This benchmark Pt catalyst should give idealized photoelectrochemical HER activity and uniform, measurable, light loss.

Non-IR corrected J-V curves for the prepared devices are shown in Figure 2.18a for simulated AM 1.5 G illumination. For TiN/n^+p-Si, a photocurrent density of −0.5 mA/cm$^2_{geo}$ (we define V_{onset} as the potential needed to produce this current) and −10 mA/cm$^2_{geo}$ were reached at –400 mV and –700 mV vs RHE, respectively. The obtained saturated photocurrent density (J_{sat}) (~ −17.6 mA/cm$^2_{geo}$) is slightly higher than the silicon PV cell alone (J_{sc} ~ −16.3 mA/cm$^2_{geo}$) as expected from the optical performance of the TiN thin-film on Si in PEC configuration. (Figure 2.17). For the NiP_x/$NiSi_y$/ n^+p-Si, the J-V curve (Figure 2.18a) shifts negative by 175 mV at −10 mA/cm$^2_{geo}$ compared to that of TiN/ n^+p-Si. This shift clearly shows that the absence of TiN results in substantial loss of electrochemical HER performance. This can be attributed to the

formation of $NiSi_y$ on the surface as seen by XPS (Figure 2.1), which is not catalytically active for HER.

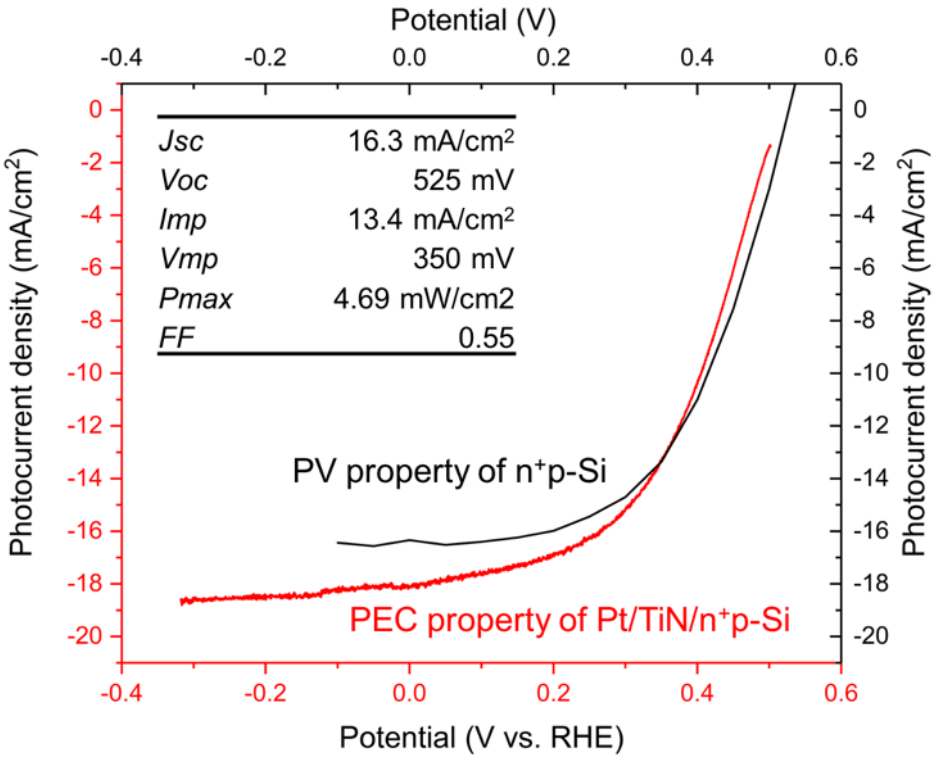

Figure 2.17 A comparison between the *J-V* curve of the as-prepared PEC (Pt/TiN/n^+p-Si, red) and PV (n^+p-Si, black). The inset is the calculated PV properties based on the measured J-V curve.

In the case of NiP_2/TiN/n^+p-Si photocathode, the J-V curve shifts positive (by 910 mV) due to the high HER activity of the cubic NiP_2 thin-film when protected by the TiN interlayer and reaches current densities of −0.5 mA/cm^2_{geo} (V_{onset}) and −10 mA/cm^2_{geo} at 399 mV and 254 mV vs. RHE, respectively. This compares to the benchmark Pt/TiN/n^+p-Si, of only 100 mV and 150 mV at these current densities, respectively. Using the latter photocathode as the reference

electrode potential allows direct extraction of the purely electrochemical overpotential (i.e. disregarding the photovoltage). Comparing $NiP_2/TiO_2/Ti/n^+p$-Si to the $NiP_2/TiN/n^+p$-Si photocathode, both a significantly lower HER activity (170 mV vs. RHE at -10 mA/cm^2) and photocurrent density (13.9 mA/cm^2) are observed. This result is consistent with the XPS depth profiles (Figure 2.9), showing the diffusion of Si and O to form a high resistance SiO_x and a highly absorptive metallic $TiSi_x$ at interfaces. This outcome reinforces the advantage of using TiN vs. TiO_2 as a protection layer to prevent both the deleterious effects from oxygen and silicon diffusion.

Figure 2.18b-c show the separate direct comparison of the photovoltage for $NiP_2/TiN/n^+p$-Si and benchmark photocathodes. The photovoltage of the $Pt/TiN/n^+p$-Si benchmark (532 mV, Figure 2.18b) is similar to V_{oc} of the PV cell, measured in the absence of electrolyte interfaces and catalysis (see Figure 2.17).

Although cubic-NiP_2 has metallic properties (conductivity and opacity), $NiP_2/TiN/n^+p$-Si (Figure 2.18c) shows only a 3% loss of photovoltage (512 mV) due to the cubic-NiP_2 layer. This low value is attributed to the layer thinness (4-20 nm) with nanometer gaps and a clean interface (no nickel silicide). This result agrees with the J-V curves (Figure 2.18a), which show almost the same J_{sat} (-18.5 mA/cm$^2_{geo}$) of the $NiP_2/TiN/n^+p$-Si as the benchmark $Pt/TiN/n^+p$-Si photocathode.

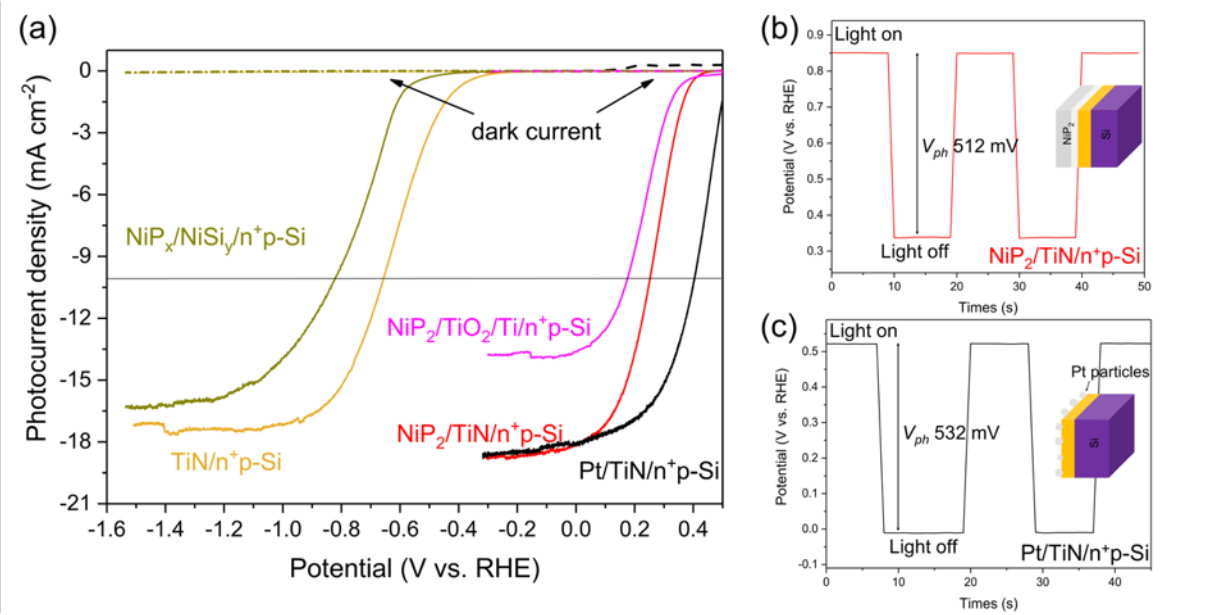

Figure 2.18 Photoelectrochemical performance at simulated AM 1.5 G solar illumination (a) non-IR-corrected *J-V* curve of $NiP_x/NiSi_y/n^+p$-Si, TiN/n^+p-Si, $NiP_2/TiO_2/Ti/n^+p$-Si, $NiP_2/TiN/n^+p$-Si, and $Pt/TiN/n^+p$-Si exposed on simulated solar illumination and dark in 0.5 M H_2SO_4 (scan rate: 10 mV/s). For driving a current density of -10 mA/cm^2, $NiP_2/TiN/n^+p$-Si requires 150 mV overpotential compared to $Pt/TiN/n^+p$-Si. Open-circuit potential measurement under simulated AM 1.5 G illumination and dark for (b) $NiP_2/TiN/n^+p$-Si and (c) benchmark $Pt/TiN/n^+p$-Si.

The above results clearly demonstrate that the combined cubic-NiP_2/TiN thin-film layers have better or comparable catalytic activity than other reported thin-film TMP catalysts when used on photocathodes, and maximal photocurrent density J_{sat} (>100% vs J_{sc} of PV cell, and 100% vs J_{sat} of the benchmark $Pt/TiN/n^+p$-Si photoelectrode). To the best of our knowledge, this is the first report that shows near maximum saturated photocurrent density, while maintaining excellent

catalytic activity in a TMP thin-film catalyst photocathode. In previous reports, using an optimized thickness of CoPS as an HER catalyst ~ 72% J_{sat} was achieved compared to a Pt/n^+p-Si benchmark photoelectrode, while an optimized thickness of CoP achieved ~ 74 % of J_{sat} of the Pt/n^+p-Si benchmark.[31,58]

At wavelengths >550 nm, incident photon-to-current efficiency (IPCE) reveals that NiP_2/TiN/n^+p-Si is > 50% efficient (Figure 2.19). Loss of efficiency at wavelengths below 500 nm is attributed to light absorption in the cubic-NiP_2/TiN thin-film layers, which causes recombination and thus does not contribute to the photovoltage and J_{sat}, in agreement with

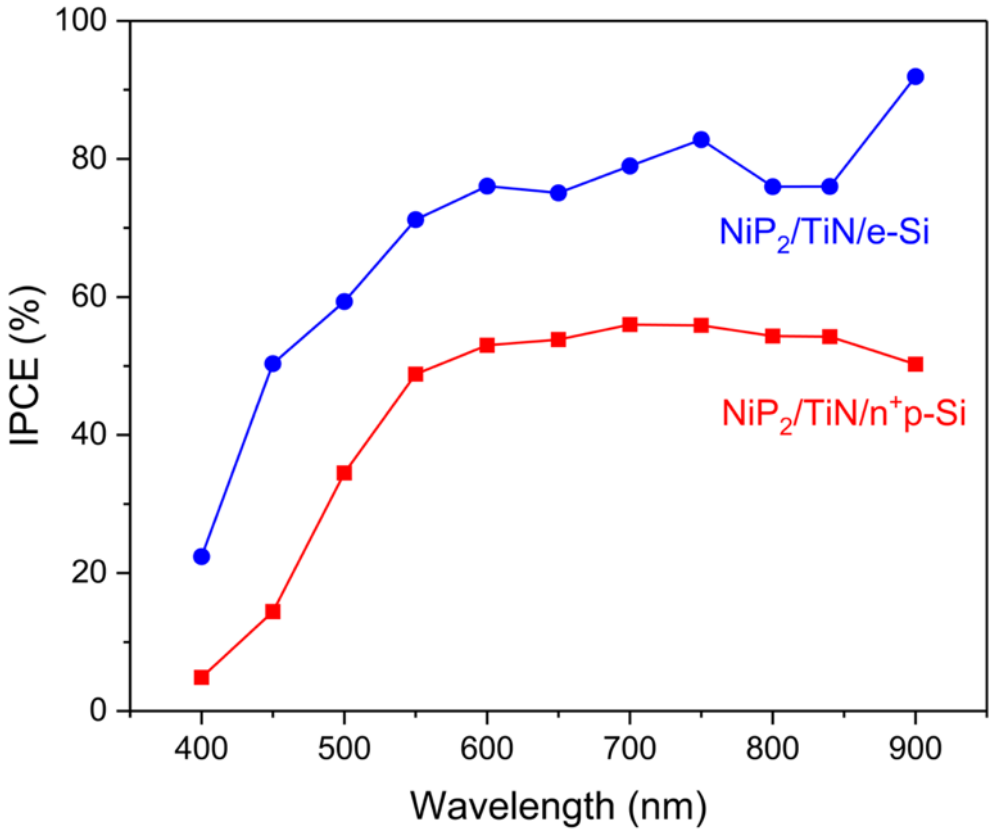

Figure 2.19 Incident photon-to-current efficiency (IPCE) of NiP_2/TiN/n^+p-Si and NiP_2/TiN/e-Si.

observations in literature for surface protected n^+p-Si photoelectrodes.[31]

Photoelectrochemical stability

To demonstrate the photoelectrochemical stability of the device, chronoamperometry (CA) was conducted under simulated 1-sun illumination in 0.5 M H_2SO_4 at 0 applied V vs. RHE (Figure 2.20a). The photocathode maintains a stable H_2 evolution photocurrent (standard deviation, $A_0 \pm 10\%$) without failure for at least 125 hours in acid, which was the maximal duration of our experiments. No long-term degradation on this time scale was detectable. This contrasts with previous reports of other thin-film catalysts which dissolved or delaminated during operation, allowing for corrosion of any newly uncovered photoabsorber. [59,60] We investigated the chemical state of the electrode surface by XPS (2p core levels see Figure 2.20b-d) of our photocathode over time. For the as-prepared sample, the binding energy of $Ni2p_{3/2}$ is 854.6 eV, shifted to higher energies compared to standard nickel phosphides (853.2 eV) reported in NIST or other literature.[34,61] This shift likely occurred due to surface oxidation with the inevitable air exposure between electrolysis and analysis. The major P peak ($2p_{3/2}$ core level) occurs at 129.3 eV close to elemental P, as well as a minor peak at 133.2 eV in the P-O (phosphate) region. For Ti, a low signal-to-noise intensity was observed for the Ti 2p core level, as expected due to conformal coverage of the NiP_2 top layer. As expected, no Si was detected which is attributed to the absence of Si diffusion in the upper layers and the NiP_2/TiN thickness being far beyond the electron escape depth (< 3 nm).[62]

XPS studies at 26 hours of continuous photoelectrolytic operation (Figure 2.20c), reveals P, Si and Ti core level unchanged, but now a chemically reduced Ni state (violet) appears, which is attributed to the catalytically active state of the nickel phosphides during electrolytic HER.[13,54,55] This reduction occurs in parallel with partial removal of the surface P-O (orange). After 125 hours of operation (Figure 2.20d), the surface of oxides of both Ni and P were further reduced, but minor peaks for silicon oxide and titanium oxide were now detected at the top surface (Figure 2.21). In order to verify the source of these elements, gentle sputtering (60 s, 1000 eV Ar^+) was conducted to etch the surface layer, followed by XPS measurement. The sputter cleaning reveals that both silicon and titanium oxides were removed, hence they are found only at the top surface with the electrolyte interface (Figure 2.20d). The surface silicon oxide contamination likely came from the fracture of the Si substrate during disassembly of the epoxy-sealed electrode. Similarly, titanium oxide came from the nanoparticulate TiO_2 additive in the epoxy (Loctite Hysol 1C) required to properly mask the illumination area.[63]

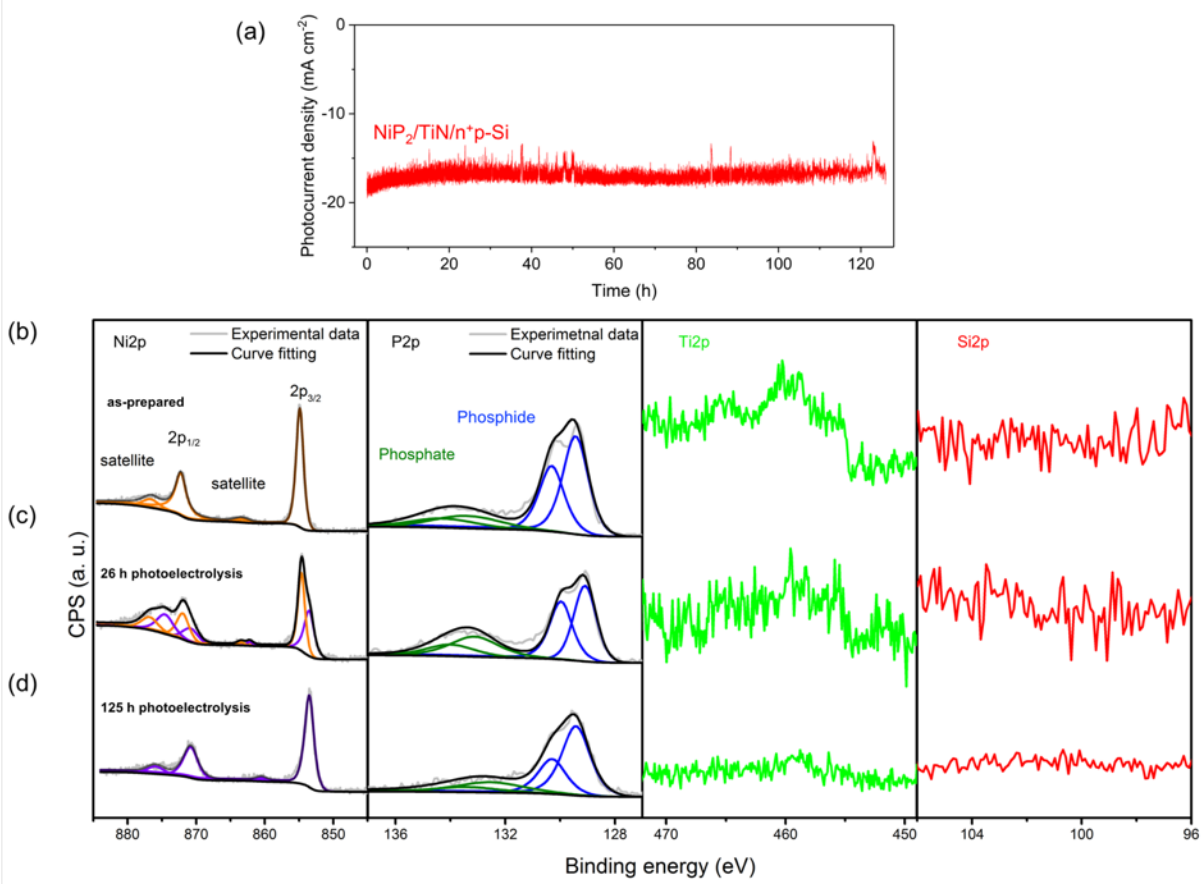

Figure 2.20 Photoelectrochemical stability of $NiP_2/TiN/n^+p$-Si. (a) chronoamperometry (CA) measurement of $NiP_2/TiN/n^+p$-Si photocathode for 125 h continuous illumination at 0 V vs. RHE in 0.5 M H_2SO_4. Time-dependent XPS measurement for (b)as-prepared, (c) after 26 h and (d) after 125h photoelectrolysis of $NiP_2/TiN/n^+p$-Si samples. Ni2p and P2p core level shows experimental data (grey) and fitting envelope (black line), and peak fits corresponding to surface oxidized Ni (orange), metallic Ni (violet), metallic P (blue), and phosphate (green). For Ti2p (light green) and Si2p (red), no noticeable signals have been detected.

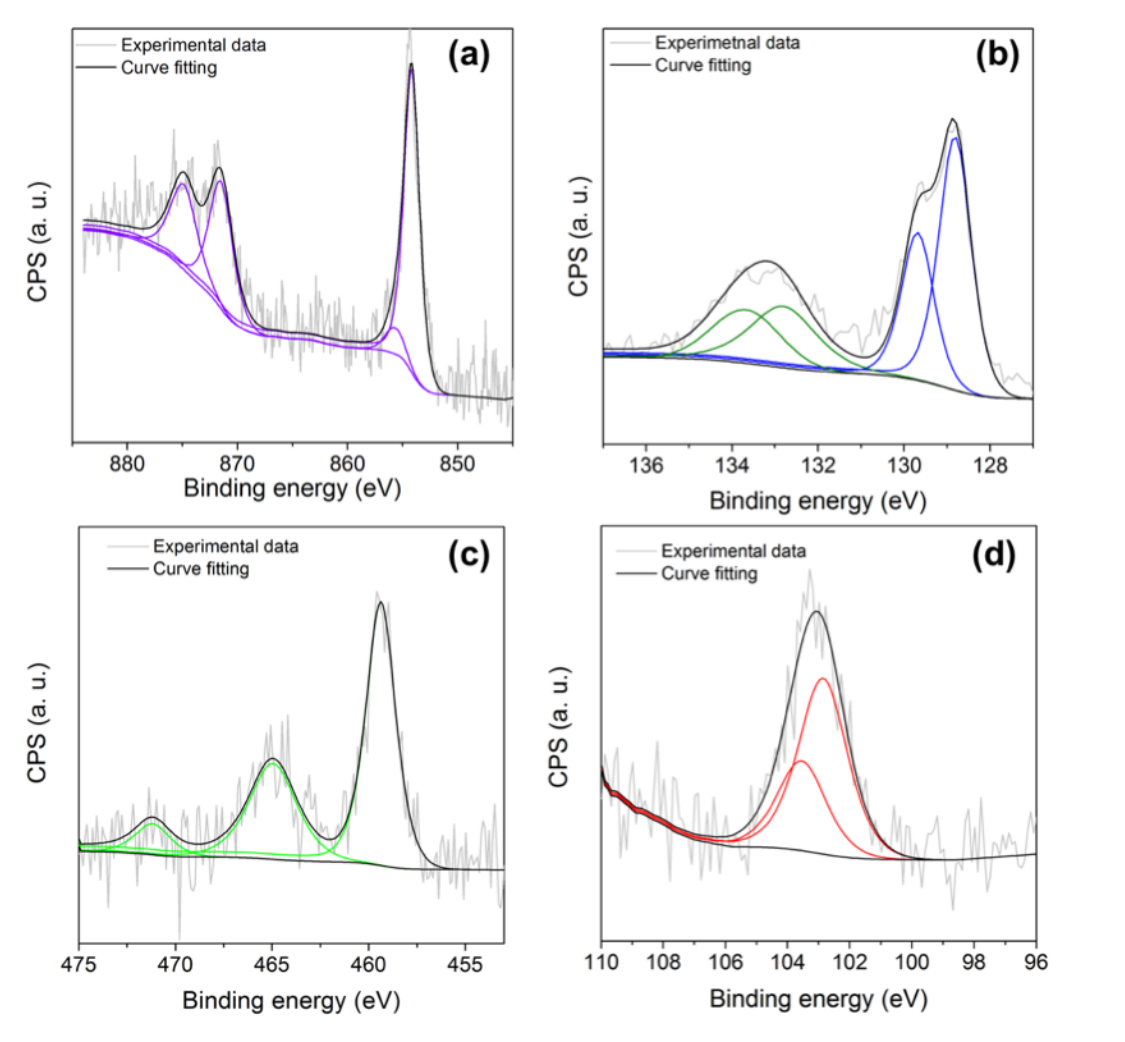

Figure 2.21 XPS top surface analysis of a NiP_2/TiN/n^+p-Si sample run for 125 hours. Binding energy of XPS spectra were selected at (a) Ni2p, (b) P2p, (c) Ti2p, and (d) Si2p core levels. The Ni2p spectra shows a metallic nickel feature of NiP_2 (violet). The P2p spectra has phosphide (blue) with small amount of phosphate (green). The Ti2p spectra exhibits a titanium oxide feature (binding energy of $2p^{3/2}$ is 458.8 eV),[67] and silicon oxide is also detected in the Si2p spectra (red)(binding energy of $2p^{3/2}$ is 103.2 eV).[68] However, gentle sputtering removed these peaks (Figure 2.20d) while the peaks associated with the top-layer of NiP_2 remains, which demonstrates that these are surface contaminants.

Together these time-dependent CA and XPS results demonstrate that the cubic-NiP_2/TiN thin-film layers do not degrade or delaminate during 125 h operation. During photoelectrolysis the catalyst undergoes electrochemical transformation consistent with the expected redox activation for HER.[22,64] We conclude that the materials, the interfaces and the processing methods provide excellent stability during extended photoelectrochemical turnover.

Applicability of thin-film cubic-NiP_2/TiN layers

While a highly efficient thin-film electrocatalyst should decrease the kinetic barrier for HER with negligible parasitic light absorption, overall photoelectrochemical performance often times relies strongly on the photoabsorber's properties. To enhance the photoelectrochemical performance and demonstrate the versatility of the c-NiP_2/TiN catalyst/protection layers, we applied these to a commercially available crystalline Si solar cell. This allows understanding of the correlation between the performance of the cubic-NiP_2/TiN thin-film layers (catalytic activity and negligible light absorption) and the properties of an independently benchmarked and readily available photoabsorber.

In contrast to the in-house fabricated n^+p-Si photoabsorber, the single-crystal Si solar cell (sc-Si) is covered with several front and back antireflective coatings, reflective internal layers and digitated silver metal contacts.[62,65] Before applying the catalyst/protection layers to the sc-Si solar cell, sequential wet-etching steps are required to uncover the pristine Si surface (see Experimental details). The HIM image of the etched sc-Si solar cell (e-Si) shows the micro-pyramidal morphology of Si which is commonly used for the high efficiency Si solar cell (Figure

2.22a).[65] Elemental XPS analysis demonstrates the presence of only Si (residual O from the native oxide and adventitious C) and the absence of other expected surface element impurities (Ag, Al) (Figure 2.22b-d), consistent with the successful removal of the surface layers (Figure 2.22a). Standard PV properties of sc-Si, e-Si, and n^+p-Si in the absence of electrolyte are compared in Figure 2.23 and summarized in Table 2.1. These results reveal that commercial sc-

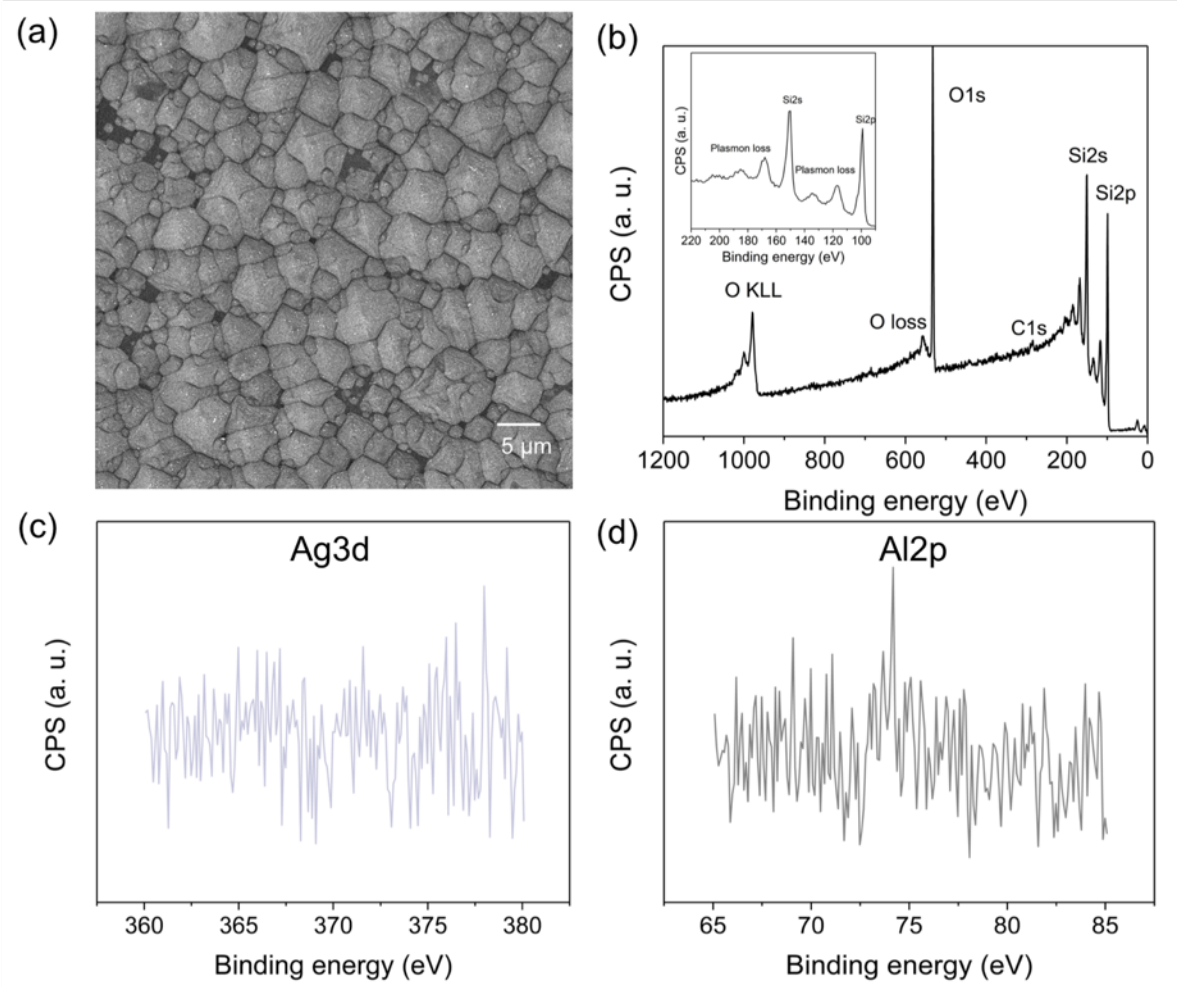

Figure 2.22 (a) Helium ion microscope image of sequentially etched Si solar cell substrate (e-Si). Inset shows plasmon loss peaks from Si2s and Si2p. X-ray photoelectron spectra of e-Si (b) survey (c) Ag3d core level, and (d) Al2p core level.

Si and e-Si produce doubled J_{sc} compared to that of the in-house produced n^+p-Si. The e-Si sample has a ~10% lower J_{sc} than sc-Si, due to the removal of the surface coatings. In contrast, the V_{oc} is not substantially different between the in-house fabricated n^+p-Si and the e-Si solar cell, while the sc-Si does show a slight improvement over the e-Si. The most obvious difference between the e-Si and sc-Si is the decreased fill factor, which is attributed to the removal of the top anti-reflective coatings and digitated metal silver contact.

Cubic-NiP_2/TiN thin-film layers were then fabricated on the e-Si substrate using the same

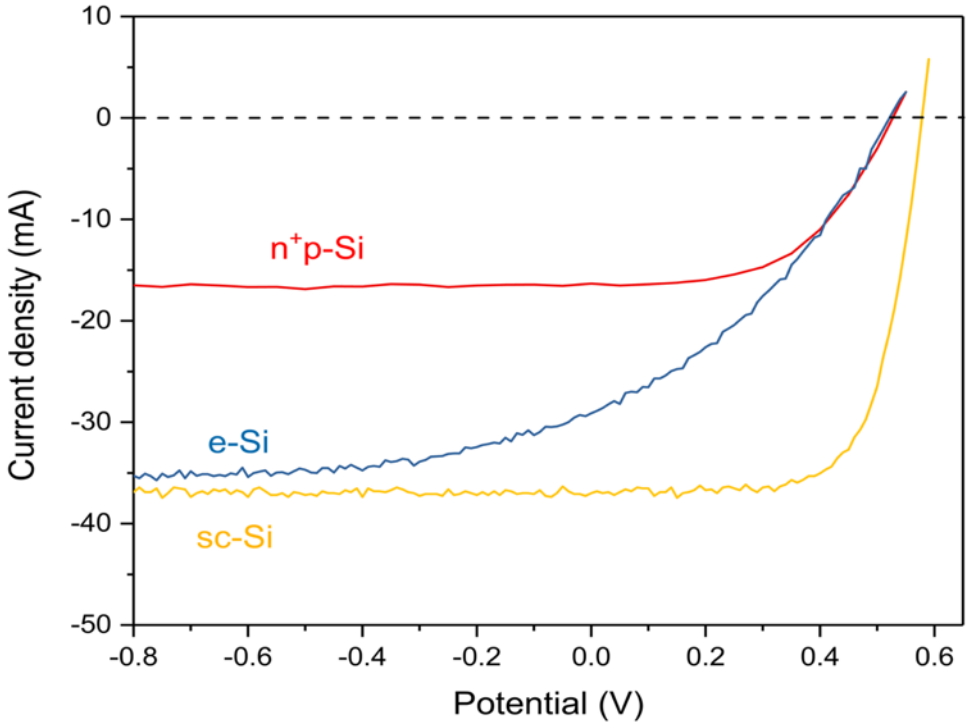

Figure 2.23 J-V curve of a different Si-based PV substrates.

method described above. A HIM image of this junction (Figure 2.24a) shows the same Si micropyramidal structure as on the pristine e-Si with no additional morphologies, indicating uniform coverage by the catalyst/protection layers. A high magnification image (Figure 2.24a,

inset) reveals NiP_2 grain sizes in the interval of 20 – 40 nm, similar to that of the in-house junction, NiP_2/TiN/n^+p-Si (Figure 2.10a). Comparing the non-IR corrected photoelectrochemical J-V curve of NiP_2/TiN/e-Si (Figure 2.24b), it reaches current densities of −0.5 mA/cm$^2_{geo}$ (V_{onset}) and −10 mA/cm$^2_{geo}$ at 405 mV and 313 mV vs. RHE, respectively. Between 0 and -0.4 V vs. RHE a constant photocurrent density is achieved of mean value −36.3 mA/cm^2 (J_{sat}) with 100% Faradaic efficiency (Figure 2.14). J_{sat} of NiP_2/TiN/e-Si is two-times higher than the J_{sat} using the in-house fabricated PV junction, NiP_2/TiN/n^+p-Si, at the given potential; indicating that the c-NiP_2/TiN catalyst/protection layers can effectively be applied to PV-optimized commercial grade solar cells without losses in photoabsorber properties. When the IPCE is measured at 0 V vs. RHE (Figure 2.19), it is over 70% at wavelengths above 500 nm. Comparing the PV (electrolyte-

	n^+p-Si	**e-Si**	**sc-Si**
J_{sc}	−16.3 mA/cm^2	−35.2 mA/cm^2	−37.3 mA/cm^2
V_{oc}	0.525 V	0.530 V	0.580 V
FF	0.55	0.22	0.67
Efficiency	4.69%	4.10%	14.29%

Table 2.1 Summary of PV properties for different Si-based PV substrates

free) properties of the bare e-Si substrate to those of the NiP_2/TiN/e-Si, J_{sat} is slightly increased and 98% of photovoltage is retained (**Error! Reference source not found.**), analogous to the o bservations for the n^+p-Si

substrate. This clearly demonstrates that our newly developed cubic-NiP_2/TiN thin-film catalyst/protection layers do not compromise the photoelectrochemical properties and is directly applicable to high efficiency, commercial-grade single crystal Si photoabsorbers.

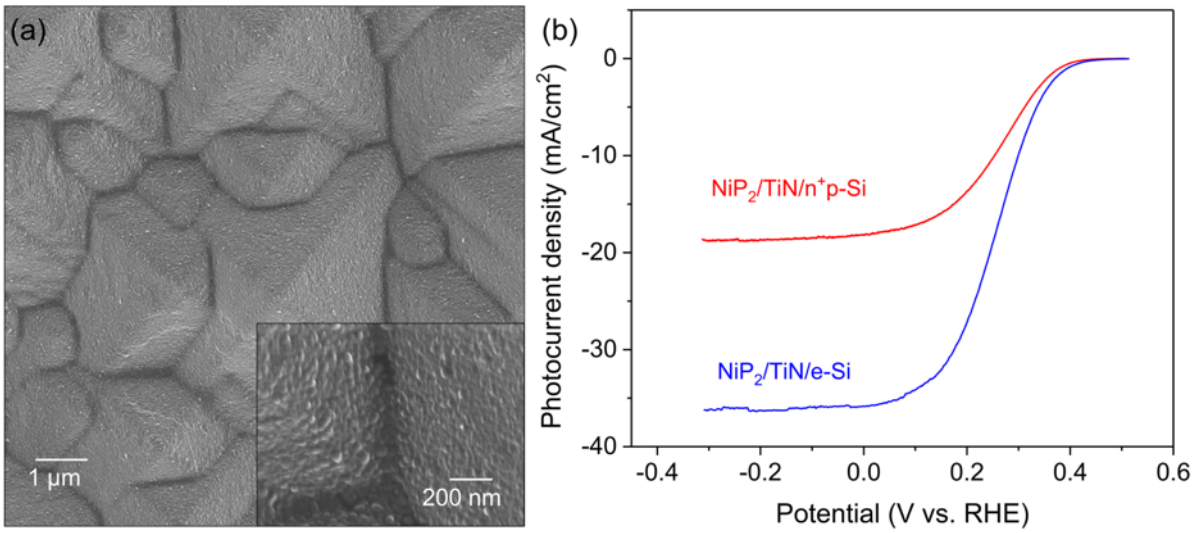

Figure 2.24 (a) Helium ion microscope image of NiP_2 surface obtained from commercial micropyramid Si solar cell substrate (NiP_2/TiN/e-Si). High-magnification image of inset shows uniform coverage of NiP_2 grains. (b) Photoelectrochemical performance (Non IR-corrected J-V curve) of NiP_2/TiN/n^+p-Si and NiP_2/TiN/e-Si exposed on simulated 1.5 AM G illumination in 0.5 M H_2SO_4 (Scan rate: 10 mA/cm^2).

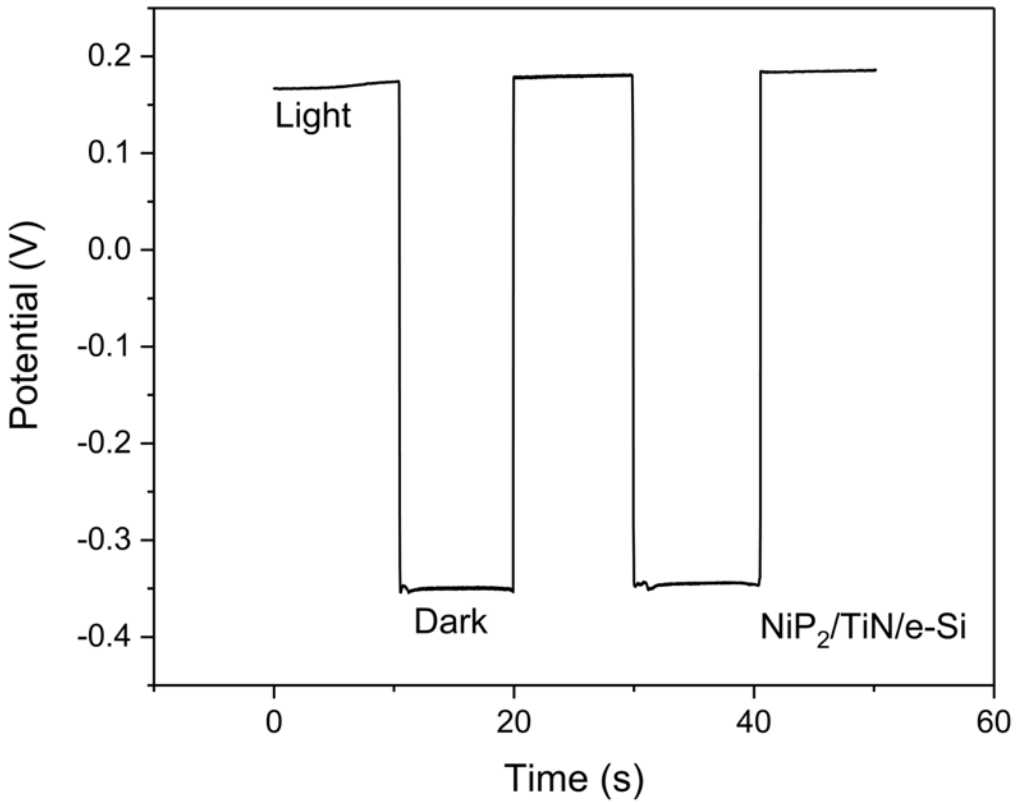

Figure 2.25 Open-circuit potential measurement under simulated AM 1.5 G illumination and dark for NiP_2/TiN/e-Si, Vph is 520 mV

2.5 Conclusions

We have developed a successful fabrication route to nano-crystalline thin-films of cubic-NiP_2 on a TiN-protected Si photocathode that allows efficient PEC water splitting using low cost materials. The elemental and structural analysis conducted by STEM, RBS, and XPS demonstrates the importance of the TiN interfacial layer as a necessary component to inhibit elemental diffusion during photoelectrode fabrication. The specific advantages of TiN are demonstrated relative to a commonly used TiO_2 interfacial layer. The latter underperforms relative to TiN because it is incapable of preventing atomic diffusion during the high temperature

synthesis. Cross-sectional STEM analysis identified partially oriented NiP_2 along the (001) plane, which may contribute to its superior HER performance. HER activity when normalized to two independent surface area estimates indicates excellent TOF (0.41 to 1.04 H_2 $site^{-1}$ s^{-1}) for the NiP2 thin-film. Photoelectrochemical studies confirm that the saturated photocurrent density is not compromised by the metallic NiP_2 and TiN layers, while maintaining high catalytic activity for HER. The corrosion resistance of cubic-NiP_2/TiN thin-film layers demonstrates stable activity for over 125 hours without deleterious changes to the performance during the test. When these catalyst/protection layers are applied to a commercial-grade high efficiency Si photoabsorber, it retains high photoelectrochemical performance, thereby showing the applicability of this strategy to highly-engineered commercial solar cell. The facile implementation of the cubic-NiP_2/TiN thin-film catalyst/protection layers opens an opportunity to investigate their implementation onto other highly engineered photoabsorbers (such as multijunction Si, and high-efficiency III-V semiconductors). In conclusion, our work illustrates the opportunity to improve long term operation of photoelectrochemical systems using earth-abundant materials. Precious metals are not necessary, neither for catalysis nor durability of the electrolyte/catalyst/photoabsorber interfaces. These advances bring energy conversion from sunlight into fuels closer to reality

2.6 Acknowledgements

This work was supported by a joint DOE-EERE (energy Efficiency and Renewable Energy)/NSF-CBET (Chemical, Bioengineering, Environmental, and Transport systems) award

number 1433492 and continuation award from DOE-EERE number DE -EE0008083. This research used resources of the Center for Functional Nanomaterials, which is a U.S. DOE Office of Science Facility, at Brookhaven National Laboratory under Contract No. DE-SC0012704. We thank R. Thorpe for measuring RBS spectra, and J. Tracey, and Dr. D. M. O'Carroll for helping with reflectance measurements.

2.7 References

(1) Jacobson, M. Z.; Colella, W. G.; Golden, D. M. Cleaning the Air and Improving Health with Hydrogen Fuel-Cell Vehicles. *Science* **2005**, *308* (5730), 1901–1905.

(2) Christopher, K.; Dimitrios, R. A Review on Exergy Comparison of Hydrogen Production Methods From Renewable Energy Sources. *Energy Environ. Sci.* **2012**, *5* (5), 6640–6651.

(3) Lewis, N. S.; Nocera, D. G. Powering the Planet: Chemical Challenges in Solar Energy Utilization. *PNAS* **2006**, *103* (43), 15729–15735.

(4) Bard, A. J.; Fox, M. A. Artificial Photosynthesis: Solar Splitting of Water to Hydrogen and Oxygen. *Acc. Chem. Res.* **1995**, No. 28, 141–145.

(5) Fujishima, A.; Honda, K. Electrochemical Photolysis of Water at a Semiconductor Electrode. *Nature* **1972**.

(6) Turan, B.; Becker, J.-P.; Urbain, F.; Finger, F.; Rau, U.; Haas, S. Upscaling of Integrated Photoelectrochemical Water-Splitting Devices to Large Areas. *Nat Comms* **2016**, *7* (1), 12681.

(7) Nordmann, S.; Berghoff, B.; Hessel, A.; Zielinsk, B.; John, J.; Starschich, S.; Knoch, J. Record-High Solar-to-Hydrogen Conversion Efficiency Based on a Monolithic All-Silicon Triple-Junction IBC Solar Cell. *Sol. Energy Mater. Sol. Cells* **2019**, *191*, 422–426.

(8) Urbain, F.; Tang, P.; Carretero, N. M.; Andreu, T.; Gerling, L. G.; Voz, C.; Arbiol, J.; Morante, J. R. A Prototype Reactor for Highly Selective Solar-Driven CO 2 Reduction to Synthesis Gas Using Nanosized Earth-Abundant Catalysts and Silicon Photovoltaics. *Energy Environ. Sci.* **2017**, *10* (10), 2256–2266.

(9) Urbain, F.; Smirnov, V.; Becker, J.-P.; Rau, U.; Ziegler, J.; Kaiser, B.; Jaegermann, W.; Finger, F. Application and Modeling of an Integrated Amorphous Silicon Tandem Based Device for Solar Water Splitting. *Sol. Energy Mater. Sol. Cells* **2015**, *140*, 275–280.

(10) Jia, J.; Seitz, L. C.; Benck, J. D.; Huo, Y.; Chen, Y.; Ng, J. W. D.; Bilir, T.; Harris, J. S.; Jaramillo, T. F. Solar Water Splitting by Photovoltaic-Electrolysis with a Solar-to-Hydrogen Efficiency Over 30. *Nat Comms* **2016**, *7*, 13237.

(11) Hu, S.; Shaner, M. R.; Beardslee, J. A.; Lichterman, M.; Brunschwig, B. S.; Lewis, N. S. Amorphous TiO2 Coatings Stabilize Si, GaAs, and GaP Photoanodes for Efficient Water Oxidation. *Science* **2014**, *344* (6187), 1005–1009.

(12) Seger, B.; Tilley, S. D.; Pedersen, T.; Vesborg, P. C. K.; Hansen, O.; Grätzel, M.; Chorkendorff, I. Silicon Protected with Atomic Layer Deposited TiO2: Conducting Versus Tunnelling Through TiO2. *J. Mater. Chem. A* **2013**, *1* (47), 15089–15094.

(13) Fan, R.; Mao, J.; Yin, Z.; Jie, J.; Dong, W.; Fang, L.; Zheng, F.; Shen, M. Efficient and Stable Silicon Photocathodes Coated with Vertically Standing Nano-MoS2 Films for Solar Hydrogen Production. *ACS Appl. Mater. Interfaces* **2017**, *9* (7), 6123–6129.

(14) Britto, R. J.; Benck, J. D.; Young, J. L.; Hahn, C.; Deutsch, T. G.; Jaramillo, T. F. Molybdenum Disulfide as a Protection Layer and Catalyst for Gallium Indium Phosphide Solar Water Splitting Photocathodes. *J. Phys. Chem. Lett.* **2016**, *7* (11), 2044–2049.

(15) Urbain, F.; Smirnov, V.; Becker, J.-P.; Lambertz, A.; Yang, F.; Ziegler, J.; Kaiser, B.; Jaegermann, W.; Rau, U.; Finger, F. Multijunction Si Photocathodes with Tunable Photovoltages From 2.0 v to 2.8 v for Light Induced Water Splitting. *Energy Environ. Sci.* **2016**, *9* (1), 145–154.

(16) Urbain, F.; Smirnov, V.; Becker, J.-P.; Finger, F. Impact of Light-Induced Degradation on the Performance of Multijunction Thin-Film Silicon-Based Photoelectrochemical Water-Splitting Devices. *Cryst. Growth Des.* **2016**, *1* (5), 832–836.

(17) Voiry, D.; Salehi, M.; Silva, R.; Fujita, T.; Chen, M.; Asefa, T.; Shenoy, V. B.; Eda, G.; Chhowalla, M. Conducting MoS_2 Nanosheets as Catalysts for Hydrogen Evolution Reaction. *Nano Lett.* **2013**, *13* (12), 6222–6227.

(18) Laursen, A. B.; Patraju, K. R.; Whitaker, M. J.; Retuerto, M.; Sarkar, T.; Yao, N.; Ramanujachary, K. V.; Greenblatt, M.; Dismukes, G. C. Nanocrystalline Ni_5P_4 : A Hydrogen Evolution Electrocatalyst of Exceptional Efficiency in Both Alkaline and Acidic Media. *Energy Environ. Sci.* **2015**, *8* (3), 1027–1034.

(19) Wang, X.; Kolen'ko, Y. V.; Bao, X. Q.; Kovnir, K.; Liu, L. One-Step Synthesis of Self-Supported Nickel Phosphide Nanosheet Array Cathodes for Efficient Electrocatalytic Hydrogen Generation. *Angew. Chem. Int. Ed. Engl.* **2015**, *54* (28), 8188–8192.

(20) Prévot, M. S.; Sivula, K. Photoelectrochemical Tandem Cells for Solar Water Splitting. *J. Phys. Chem. C* **2013**, *117* (35), 17879–17893.

(21) Seger, B.; Pedersen, T.; Laursen, A. B.; Vesborg, P. C. K.; Hansen, O.; Chorkendorff, I. Using TiO_2 As a Conductive Protective Layer for Photocathodic H_2 Evolution. *J. Am. Chem. Soc.* **2013**, *135* (3), 1057–1064.

(22) Seger, B.; Laursen, A. B.; Vesborg, P. C. K.; Pedersen, T.; Hansen, O.; Dahl, S.; Chorkendorff, I. Hydrogen Production Using a Molybdenum Sulfide Catalyst on a Titanium-Protected N+P-Silicon Photocathode. *Angew. Chem. Int. Ed.* **2012**, *51* (36), 9128–9131.

(23) Yan, Y.; Xia, B.; Xu, Z.; Wang, X. Recent Development of Molybdenum Sulfides as Advanced Electrocatalysts for Hydrogen Evolution Reaction. *ACS Catal.* **2014**, *4* (6), 1693–1705.

(24) Huang, Z.; Chen, Z.; Chen, Z.; Lv, C.; Meng, H.; Zhang, C. $Ni_{12}P_5$ Nanoparticles as an Efficient Catalyst for Hydrogen Generation via Electrolysis and Photoelectrolysis. *ACS Nano* **2014**, *8* (8), 8121–8129.

(25) Bao, X. Q.; Cerqueira, M. F.; Alpuim, P.; Liu, L. Silicon Nanowire Arrays Coupled with Cobalt Phosphide Spheres as Low-Cost Photocathodes for Efficient Solar Hydrogen Evolution. *Chem. Commun.* **2015**, *51* (53), 10742–10745.

(26) Seh, Z. W.; Kibsgaard, J.; Dickens, C. F.; Chorkendorff, I.; Nørskov, J. K.; Jaramillo, T. F. Combining Theory and Experiment in Electrocatalysis: Insights Into Materials Design. *Science* **2017**, *355* (6321), eaad4998.

(27) Kibsgaard, J.; Tsai, C.; Chan, K.; Benck, J. D.; Nørskov, J. K.; Abild-Pedersen, F.; Jaramillo, T. F. Designing an Improved Transition Metal Phosphide Catalyst for Hydrogen Evolution Using Experimental and Theoretical Trends. *Energy Environ. Sci.* **2015**, *8* (10), 3022–3029.

(28) Hellstern, T. R.; Benck, J. D.; Kibsgaard, J.; Hahn, C.; Jaramillo, T. F. Engineering Cobalt Phosphide (CoP) Thin Film Catalysts for Enhanced Hydrogen Evolution Activity on Silicon Photocathodes. *Adv. Energy Mater.* **2015**, No. 4, 1501758.

(29) Wang, H.; Deutsch, T.; Welch, A.; Turner, J. A. The Stability of Illuminated P-GaInP$_2$ Semiconductor Photoelectrode. *Int. J. Hydrogen Energy* **2012**, *37* (19), 14009–14014.

(30) Chen, F.; Zhu, Q.; Wang, Y.; Cui, W.; Su, X.; Li, Y. Efficient Photoelectrochemical Hydrogen Evolution on Silicon Photocathodes Interfaced with Nanostructured NiP$_2$ Cocatalyst Films. *ACS Appl. Mater. Interfaces* **2016**, *8* (45), 31025–31031.

(31) Laursen, A. B.; Kegnæs, S.; Dahl, S.; Chorkendorff, I. Molybdenum Sulfides—Efficient and Viable Materials for Electro - and Photoelectrocatalytic Hydrogen Evolution. *Energy Environ. Sci.* **2012**, *5* (2), 5577–5591.

(32) Read, C. G.; Callejas, J. F.; Holder, C. F.; Schaak, R. E. General Strategy for the Synthesis of Transition Metal Phosphide Films for Electrocatalytic Hydrogen and Oxygen Evolution. *ACS Appl. Mater. Interfaces* **2016**, *8* (20), 12798–12803.

(33) Butz, R.; Rubloff, G. W.; Ho, P. S. Chemical Bonding and Reactions at Ti/Si and Ti/Oxygen/Si Interfaces. *Journal of Vacuum Science & Technology A* **1982**, *1* (2), 771–775.

(34) Colgan, E. G.; Gambino, J. P.; Hong, Q. Z. Formation and Stability of Silicides on Polycrystalline Silicon. *Mater. Sci. Eng., R* **1996**, *16* (2), 43–96.

(35) Qin, M.; Poon, V. M. C.; Ho, S. C. H. Investigation of Polycrystalline Nickel Silicide Films as a Gate Material. *J. Electrochem. Soc.* **2001**, *148* (5), G271–G274.

(36) Lee, R. T. P.; Yang, L. T.; Liow, T. Y.; Tan, K. M.; Lim, A. E. J.; Ang, K. W.; Lai, D. M. Y.; Hoe, K. M.; Lo, G. Q.; Samudra, G. S.; et al. Nickel-Silicide:Carbon Contact Technology for N-Channel MOSFETs with Silicon-Carbon Source/Drain. *IEEE Electron Device Lett.* **2008**, *29* (1), 89–92.

(37) He, Q.; Huang, W. M.; Gao, X. Y.; Hong, M. H. Numerical Investigation of CO2 Laser Heating for Annealing Ni/Ti Multilayer Thin Films. *Smart Mater. Struct.* **2005**, *14* (6), 1320–1324.

(38) Jiang, H.; Petersson, C. S.; Nicolet, M. A. Thermal Oxidation of Transition Metal Silicides. *Thin Solid Films* **1986**, *140* (1), 115–130.

(39) van Gurp, G. J.; Langereis, C. Cobalt Silicide Layers on Si. I. Structure and Growth. *J. Appl. Phys.* **1975**, *46* (10), 4301–4307.

(40) Biunno, N.; Narayan, J.; Hofmeister, S. K.; Srivatsa, A. R.; Singh, R. K. Low-Temperature Processing of Titanium Nitride Films by Laser Physical Vapor Deposition. *Appl. Phys. Lett.* **1989**, *54* (16), 1519.

(41) Libardi, J.; Grigorov, K. G.; Massi, M.; da Silva Sobrinho, A. S.; Pessoa, R. S.; Sismanoglu, B. Diffusion of Silicon in Titanium Dioxide Thin Films with Different Degree of Crystallinity: Efficiency of TiO_2 And TiN Barrier Layers. *Vacuum* **2016**, *128*, 178–185.

(42) Avasarala, B.; Haldar, P. Electrochemical Oxidation Behavior of Titanium Nitride Based Electrocatalysts Under PEM Fuel Cell Conditions. *Electrochimica Acta* **2010**, *55* (28), 9024–9034.

(43) Pan, Z.; Xiao, Y.; Fu, Z.; Zhan, G.; Wu, S.; Xiao, C.; Hu, G.; Wei, Z. Hollow and Porous Titanium Nitride Nanotubes as High-Performance Catalyst Supports for Oxygen Reduction Reaction. *J. Mat. Chem. A* **2014**, *2* (34), 13966–13975.

(44) Choi, S. K.; Chae, W.-S.; Song, B.; Cho, C.-H.; Choi, J.; Han, D. S.; Choi, W.; Park, H. Photoelectrochemical Hydrogen Production on Silicon Microwire Arrays Overlaid with Ultrathin Titanium Nitride. *J. Mater. Chem. A* **2016**, *4* (36), 14008–14016.

(45) Catellani, A.; Calzolari, A. Plasmonic Properties of Refractory Titanium Nitride. *Phys. Rev. B* **2017**, *95* (11), 115145.

(46) Chase, M. W., Jr; Curnutt, J. L.; Downey, J. R., Jr; McDonald, R. A.; Syverud, A. N.; Valenzuela, E. A. JANAF Thermochemical Tables, 1982 Supplement. *J. Phys. Chem. Ref. Data* **1982**, *11* (3), 695–940.

(47) Nebel, C. E. Photocatalysis: a Source of Energetic Electrons. *Nat. Mater.* **2013**, *12* (9), 780–781.

(48) Li, C.-T.; Li, S.-R.; Chang, L.-Y.; Lee, C.-P.; Chen, P.-Y.; Sun, S.-S.; Lin, J.-J.; Vittal, R.; Ho, K.-C. Efficient Titanium Nitride/Titanium Oxide Composite

Photoanodes for Dye-Sensitized Solar Cells and Water Splitting. *J. Mater. Chem.* **2015**, *3* (8), 4695–4705.

(49) FILMETRICS. Reflectance Calculator Https://Www.Filmetrics.com/Reflectance-Calculator. October 8, 2018.

(50) Esposito, D. V.; Levin, I.; Moffat, T. P.; Talin, A. A. H_2 Evolution at Si-Based Metal–Insulator–Semiconductor Photoelectrodes Enhanced by Inversion Channel Charge Collection and H Spillover. *Nat. Mater.* **2013**, *12* (6), 562–568.

(51) Ros, C.; Andreu, T.; Hernández-Alonso, M. D.; Penelas-Pérez, G.; Arbiol, J.; Morante, J. R. Charge Transfer Characterization of ALD-Grown TiO2 Protective Layers in Silicon Photocathodes. *ACS Appl. Mater. Interfaces* **2017**, *9* (21), 17932–17941.

(52) Postek, M. T.; Vladar, A. E. Helium Ion Microscopy and Its Application to Nanotechnology and Nanometrology. *Scanning* **2008**, *30* (6), 457–462.

(53) Jiang, P.; Liu, Q.; Sun, X. NiP_2 Nanosheet Arrays Supported on Carbon Cloth: an Efficient 3D Hydrogen Evolution Cathode in Both Acidic and Alkaline Solutions. *Nanoscale* **2014**, *6* (22), 13440–13445.

(54) Shinagawa, T.; Garcia-Esparza, A. T.; Takanabe, K. Insight on Tafel Slopes From a Microkinetic Analysis of Aqueous Electrocatalysis for Energy Conversion. *Sci. Rep.* **2015**, *5* (1), 163.

(55) Smith, D. D.; Cousins, P. J.; Masad, A.; Waldhauer, A.; Westerberg, S.; Johnson, M.; Tu, X.; Dennis, T.; Harley, G.; Solomon, G.; et al. Generation III High Efficiency Lower Cost Technology: Transition to Full Scale Manufacturing; IEEE, 2012; pp 1594–1597.

(56) Cabán-Acevedo, M.; Stone, M. L.; Schmidt, J. R.; Thomas, J. G.; Ding, Q.; Chang, H.-C.; Tsai, M.-L.; He, J.-H.; Jin, S. Efficient Hydrogen Evolution Catalysis Using Ternary Pyrite-Type Cobalt Phosphosulphide. *Nat. Mater.* **2015**, *14* (12), 1245–1251.

(57) Walter, M. G.; Warren, E. L.; McKone, J. R.; Boettcher, S. W.; Mi, Q.; Santori, E. A.; Lewis, N. S. Solar Water Splitting Cells. *Chem. Rev.* **2010**, *110* (11), 6446–6473.

(58) Mei, B.; Permyakova, A. A.; Frydendal, R.; Bae, D.; Pedersen, T.; Malacrida, P.; Hansen, O.; Stephens, I. E. L.; Vesborg, P. C. K.; Seger, B.; et al. Iron-Treated NiO as a Highly Transparent P-Type Protection Layer for Efficient Si-Based Photoanodes. *J. Phys. Chem. Lett.* **2014**, No. 5, 3456–3461.

(59) Naumkin, A. V.; Kraut-Vass, A.; Gaarenstroom, S. W.; Powell, C. J. NIST X-Ray Photoelectron Spectroscopy Database. **2000**.

(60) Hochella, M. F., Jr.; Carim, A. H. A Reassessment of Electron Escape Depths in Silicon and Thermally Grown Silicon Dioxide Thin Films. *Surface Science* **1988**, *197* (3), L260–L268.

(61) Döscher, H.; Young, J. L.; Geisz, J. F.; Turner, J. A.; Deutsch, T. G. Solar-to-Hydrogen Efficiency: Shining Light on Photoelectrochemical Device Performance. *Energy Environ. Sci.* **2016**, *9* (1), 74–80.

(62) Laursen, A. B.; Wexler, R. B.; Whitaker, M. J.; Izett, E. J.; Calvinho, K. U. D.; Hwang, S.; Rucker, R.; Wang, H.; Li, J.; Garfunkel, E.; et al. Climbing the Volcano of Electrocatalytic Activity While Avoiding Catalyst Corrosion: Ni 3P, a Hydrogen Evolution Electrocatalyst Stable in Both Acid and Alkali. *ACS Catal.* **2018**, *8* (5), 4408–4419.

(63) Saga, T. Advances in Crystalline Silicon Solar Cell Technology for Industrial Mass Production. *NPG Asia Mater.* **2010**, *2* (3), 96–102.

(64) Chen, Z.; Dinh, H. N.; Miller, E. Photoelectrochemical Water Splitting: Standards, Experimental Methods, and Protocols. *Springer Science & Business media: New York* **2013**.

(65) Zhen Song; Jan Hrbek, A.; Richard Osgood. Formation of TiO2 Nanoparticles by Reactive-Layer-Assisted Deposition and Characterization by XPS and STM. *Nano Lett.* **2005**, *5*, 1327–1332.

(66) Gross, T.; Ramm, M.; Sonntag, H.; Unger, W.; Weijers, H. M.; Adem, E. H. An XPS Analysis of Different SiO2 Modifications Employing a C 1s as Well as an Au 4f7/2 Static Charge Reference. *Surf. Interface Anal.* **1992**, *18*, 59–64.

Chapter 3: Highly efficient and durable III-V semiconductor-catalyst photocathodes via a transparent protection layer

3.1 Abstract

Durable performance and high efficiency in water photolysis are great challenges not yet co-achieved in photoelectrochemical cells (PEC). Although photovoltaic cells made from III-V semiconductors can achieve high optical-electrical conversion efficiency, their functional integration with electrocatalysts and operational lifetime remain great challenges. Herein, an ultra-thin TiN layer was used as diffusion barrier to protect a buried junction n^+p-$GaInP_2$ photocathode, allowing elevated temperatures for catalyst growth of Ni_5P_4 as nano-islands. The resulting PEC half-cell showed negligible absorption loss, with saturated photocurrent density and H_2 evolution equivalent to the PtRu decorated benchmark photocathode. Durability tests showed undiminished photocathode operation over 120 h, the limit of testing and exceeding previous benchmarks. Etching to remove electrodeposited copper, an introduced contaminant, restored full performance, demonstrating operational ruggedness. The TiN layer expands the synthesis conditions and protects against corrosion for stable operation of III-V PEC devices, while the Ni_5P_4 catalyst replaces costly noble metal catalysts.

3.2 Introduction

Solar energy is, by far, the largest underutilized source of CO_2-free energy.[1] If collected without loss, it could supply the global yearly energy consumed by humans in

less than 2 hours.[2] If coupled with energy storage,[3] for instance through emerging solar-driven water splitting processes, this resource could accelerate future renewable energy usage.[4-6] Photoelectrochemical water splitting using a single bandgap photoabsorber is limited in efficiency to <12%, while a tandem configuration (two coupled photoabsorbers) with optimized bandgaps may achieve up to 27-28% solar-to-hydrogen efficiency (STH).[7,8] $GaInP_2$ is the preeminent PV material, possessing excellent electronic properties and an ideal bandgap (1.8 eV) for use as the top (exposed) junction in a tandem PEC device.[7,8] However, it is susceptible to rapid corrosion in electrolytes under PEC operating conditions.[9-11] Numerous attempts have been made to protect $GaInP_2$ in PECs under hydrogen evolution reaction (HER) conditions.[10,12,13] For example, a thin film of MoS_2 was coated onto p-$GaInP_2$ as a catalyst and protection layer, using a strategy similar to that developed for protection of Si photocathodes.[14,15] This protection layer stabilizes the photocathode for 70 h, but started to show decrease of activity.[10] Additionally, significant parasitic absorption by MoS_2 and unconverted Mo (~40%) limits the maximum photocurrent density of the $GaInP_2$ by 30%. Using a so-called graded approach ($MoS_2/MoO_zS_y/MoO_x$), the optical losses can be reduced. Addition of (transparent) TiO_2 at the interface provides longer term stability from corrosion. The resulting g-MoS_2/TiO_2/p-$GaInP_2$ junction achieves saturated photocurrent on par with the unmodified benchmark (bare $GaInP_2$ plus PtRu), indicating this approach is successful for improving transparency. However, the sample maintained the initial photocurrent density for 20 h, but not tested further hence leaving corrosion stability unanswered.[12] This method is limited in scope by the choice of materials and inter-diffusional mixing at the interface of

the catalyst/protection/photoabsorber during fabrication especially at elevated temperatures. Hence, it precludes the use of buried junctions with n^+-$GaInP_2$ (10-20 nm) layers, which are responsible for increasing the photovoltage by as much as 550 mV.[16] Therefore, there is still a need for new catalyst-protection layers that do not compromise the $GaInP_2$ interface, while providing protection under the harsh water splitting conditions.

In our previous work, we demonstrated that titanium nitride (TiN) forms an excellent protection layer for Si-photocathodes under harsh synthesis conditions and has very high stability >125 h.[17] TiN has excellent physical and chemical properties, including high conductivity, hardness, and corrosion-resistance.[18] Additionally, TiN is superior to both TiO_x/Ti and TiO_2 as a diffusion barrier. It forms clean interfaces between the photoabsorber and platinum-group-metal-free (PGM-free) HER catalysts (*e.g.*, transition metal phosphides).[17,19,20]

Herein, we employ two approaches to obtain high HER activity without compromising the relevant optical performance, while increasing the stability of the buried junction n^+p-$GaInP_2$ photoabsorber. Our approach utilizes a combination of: 1) an ultra-thin TiN film deposited on n^+p-$GaInP_2$ (TiN/n^+p-$GaInP_2$) to obtain a clean and stable interface, and 2) a dispersed and partly transparent catalyst film of crystalline Ni_5P_4 nano-islands (Ni_5P_4/TiN/n^+p-$GaInP_2$). Together these approaches achieve photoactivity for HER that is comparable to the benchmark photocathode: PtRu nanoparticles on n^+p-$GaInP_2$ (PtRu/n^+p-$GaInP_2$). The partly transparent nano-island Ni_5P_4/TiN/n^+p-$GaInP_2$

photocathode exhibits a slightly improved onset photocurrent (120 mV) and an identical saturated photocurrent as the PtRu/n^+p-$GaInP_2$ benchmark.

Future commercial PECs will need to deal with contamination from various metal impurities in the electrolyte that deposit on the electrodes. We developed an effective cleaning treatment to remove surface contamination from electro-deposited Cu ions on the photocathode, which was introduced by copper electrical leads in contact with the electrolyte through epoxy crack. A simple acid wash was developed to selectively etch Cu from the surface and expose the underlying Ni_5P_4, which restores the photocurrent density to its original level. Despite repeating the reactivation procedure twice, the device maintained undiminished performance for 120h without failure or net loss in photocurrent, limited only by the duration of the test. The high activity and operational stability even after using acid washes to remove common contaminants, is consistent with our previous results on NiP_2/TiN/Si photocathodes,[17] indicating that this protection approach may be generally applicable to other PEC devices.

3.3 Experimental

Chemicals Red P (98.9%, Alfa Aesar), Ni ingot (99.99%, Kurt J lesker), TiN target (99.5%, Kurt Lesker), H_2SO_4 (99.99%, Sigma-Aldrich), Triton X100 Omnipur grade (Simga) Chemicals were used without further purification.

Metal Organic Vapor Pressure Epitaxy (MOVPE) for buried junction n^+p-$GaInP_2$ growth

Semiconductor samples were grown by atmospheric pressure MOVPE on a custom-built reactor. The GaAs substrates were cleaved into ~25 mm x 25 mm squares and then etched in NH_4OH : H_2O_2 : H_2O (2:1:10 by volume) for two minutes before loading into the reactor. The source gases included trimethylgallium, triethylgallium, triethylindium and trimethylaluminum for the group-III elements; phosphine and arsine for the group-Vs; diethylzinc and carbon tetrachloride for the p-type dopants; and dilute hydrogen selenide for the n-type dopant. Films were grown at 700°C and at growth rates of ~2-4.5 μm/hr, in a total hydrogen carrier flow of ~6 slpm. The reactor was heated to growth temperature under an arsine overpressure, and at the end of the growth cooled back to room temperature under a phosphine overpressure.

Starting from the substrate, the layer structure included a GaAs/$Al_{0.3}Ga_{0.7}As$ seed layer; a 200 nm p^+ $Al_{0.27}Ga_{0.24}In_{0.49}P$ minority carrier confinement layer; a 1 μm p-type $GaInP_2$ base layer; and a ~25 nm n^{++} $GaInP_2$ emitter layer. The compositions and thicknesses are nominal, but based on regular calibrations of the reactor.

After growth, a gold back contact was electroplated to the substrate, after a short etch in NH_4OH : H_2O_2 : H_2O (2:1:10 by volume) to remove any accumulated residue from the growth.

Pulsed laser deposition of TiN $GaInP_2$ on GaAs substrates were cleaned with Buffered Oxide Etchant (BOE) 6:1vol. NH_4F/HF for 30 s prior to introduction into the PLD vacuum chamber. Pulsed laser ablated the TiN target using a KrF excimer laser Compex 205 (λ = 248 nm d = 7 cm, 10 Hz, 2.5 – 5 J cm^{-2}; Coherent). Base pressure and temperature were kept at 5-6 × 10^{-4} Pa, 130°C, respectively.

Thermal evaporation of nickel Custom built thermal evaporator was used with W boat (Kurt J. Lesker). 3 nm of Ni deposition carried out at a rate of 1.0-1.5 Å/s as determined by quartz crystal microbalance (QCM).

Chemical vapor phosphidation Evacuated quartz ampoule with red P (3-5 mg) was sealed at 1 $\times 10^{-3}$ Pa similar to previous work.[1] The quartz ampoule was heated to 380 °C at 10 °C/min with a hold for 40 min and quenching at 280 °C.

PtRu deposition The PtRu benchmark catalyst was deposited by "flash" sputtering in a custom-built vacuum chamber. A 1.3 Pa UHP argon background was established and sputtering performed at 20 W. The sample was occluded by a shutter during a 2-minute break-in period. The brief duration, "flash" sputtering of PtRu was executed through pneumatic actuation of the shutter to expose the sample to the sputtering plume for a 2-second period.

Optical measurements All reflectance spectra were measured with a 300 W Xe arc lamp (Newport) as the light source and collected by Flame S spectrometer (Ocean Optics) equipped with integrating sphere (SI photonics). $BaSO_4$ and PTFE was used as a reference standard. Transmittance spectra were measured with an HP-8452A Diode Array spectrophotometer.

Physical characterizations Helium ion microscopy images were collected by an Orion Plus Helium Ion Microscope (ZEISS) operating at a 30 kV acceleration voltage and an ion beam current around 1 pA. X-ray photoelectron spectra were collected by a Thermo K-Alpha spectrometer with a flood gun for charge compensation. All spectra energy was calibrated against adventitious carbon (284.8eV). The TEM specimen was prepared using the Helios

focused ion beam. A ~500 nm thick amorphous carbon protection layer was first deposited by electron beam on the surface of Ni_5P_4 to ensure ideal contrast during HAADF imaging. STEM/EDS mappings were performed on the Themis Z S/TEM, operating at 300 kV with a probe current of ~450 pA. Pixel size and dwell time is 0.1*0.1 nm^2 and 24 μs, respectively. High-resolution HAADF/STEM images were taken from the Nion UltraSTEM with an acceleration voltage of 60 kV. Probe convergence half angle was 30 mrad. HAADF signal was collected from 80 mrad and above.

Electrode assembly The electrical contact of the prepared electrodes was made on the back side of the Au coated GaAs substrate with copper wire using silver paint (SPI supplies). The wire was then inserted into a Pyrex glass tube, and sealed with a mixture of epoxy resin (Loctite Hysol 1C or Loctite EA e-120HP). Electrode areas were measured with a digital photograph and ImageJ analysis. Typical electrode areas ranged between 0.1–0.2cm^2.

Photoelectrochemical measurements LSVs were performed in a 1x5cm^2 glass cuvette cell (FireflySci, Inc.) in 0.5 M H_2SO_4 with 1mM Triton X-100 using a Solartron potentiostat. Durability measurements were performed in a custom built three-electrode glass cell in 0.5M H_2SO_4 using a Bio-logic potentiostat (VSP-300). The working electrodes were illuminated by 300W Xe arc lamp which is calibrated against the $GaInP_2$ reference cell (NREL) before each measurement. For the durability test, the photoelectrode (working electrode) locates 5mm away from the quartz viewport. For counter and reference electrode, a IrO_x wire electrode (Alfa Aesar) and mercury/mercury sulfate reference electrode (single junction Hg/Hg_2SO_4, BASi) were used.

IPCE measurements The detailed procedure is reported elsewhere.[2] Briefly, a 300 W xenon arc lamp (67005, Newport) was used and monochromatic illumination provided by a monochromator (SP-50, Acton) with 10-nm increments from 300 to 750 nm. The light intensity was measured at each wavelength using a calibrated Si photodiode (S1336-8BQ, Hamamatsu). The averaged illuminated current was used and subtracted the dark current to obtain the photocurrent at each wavelength.

Faradaic Efficiency Measurement. The detail method was described elsewhere.[1] Briefly, hydrogen was quantified on an automated online GC (HP 5890 Series II). N_2 was used as a carrier gas. The calibration curve was constructed from constant current electrolysis of water (0.5M H_2SO_4 electrolyte) with flame-annealed Pt foil as working electrode and IrO_x mesh as counter electrode, separated by a Nafion membrane. At steady state, samples of the headspace were taken (averaged, n=3 at 10-minute intervals). The faradaic efficiency of the HER for Ni_5P_4/TiN/$GaInP_2$ was measured in a similar fashion at -1mA. The value reported corresponds to the average (n=3) of the headspace hydrogen concentration.

3.4 Results and discussions

We fabricated a buried junction n^+p-$GaInP_2$ on a GaAs (100) miscut 4° toward <111>B substrate wafer by epitaxial growth in a metal organic vapor phase epitaxy (MOVPE) reactor.[21,22] Before performing the surface modification, we studied the effect of various etching solutions (acid, alkaline) for removing the surface oxides on $GaInP_2$ to form a clean and stable interface layer. X-ray photoelectron spectroscopy (XPS) was performed on the bare and etched surface

(Figure 3.1). Peak fitting and reference standards confirm that the bare $GaInP_2$ has surface oxides (when exposed to ambient conditions), assigned as Ga_2O_3, In_2O_3, and PO_x which introduce an interfacial layer with low conductivity. Several etching solutions effectively removed the Ga_2O_3 and PO_x signals, but varying residual amount of In_2O_3 was observed for all etchants. Among the tested etching solutions, the *buffered* NH_4F/HF oxide etchant was the most efficient at removing

all three of the surface oxides, while not dissolving the $GaInP_2$ substrate.[23] Hence, it was used for the final cleaning.

Figure 3.2(a) and (b) shows helium ion microscope (HIM) images of the TiN/n^+p-$GaInP_2$ and Ni_5P_4/TiN/n^+p-$GaInP_2$ surfaces.[24] The clean and featureless image in Figure 3.2(a) demonstrates the TiN protection layer conformally coats the n^+p-$GaInP_2$ photoabsorber. On the other hand, Figure 3.2(b) shows that the Ni_5P_4 layer consists of uniform size crystallites, approximately 20-

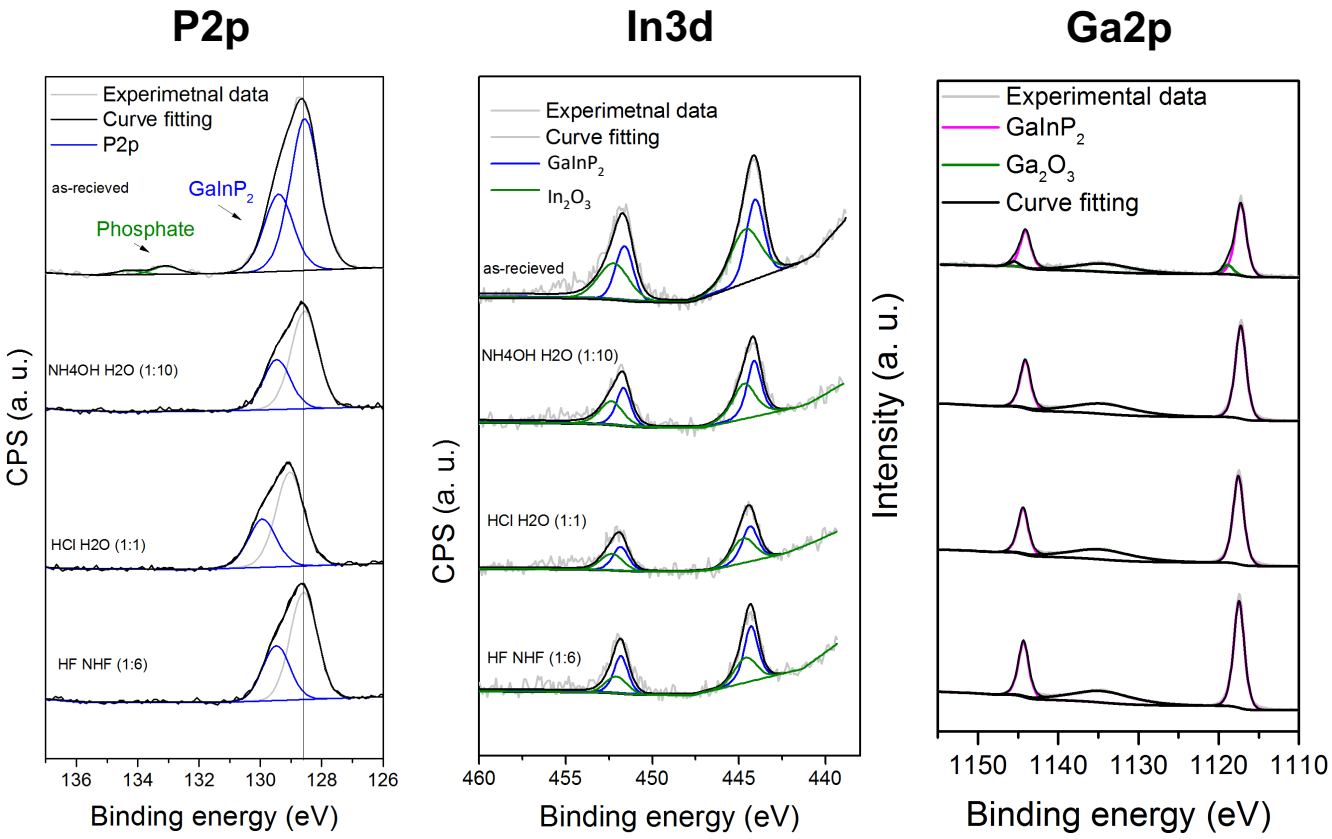

Figure 3.1 XPS core level spectra (P2p, In3d, and Ga2p) of $GaInP_2$ surface after etching the surface oxide using different etching solutions: As-received, diluted NH_4OH, concentrated HCl, and NH_4/HF buffered oxide etchant.

30 nm in diameter, that are irregularly spaced (randomly oriented). These "nano-islands" have similar size and morphology as cubic-NiP_2 on Si(100), as we previously reported. [17] The non-conformal coating of Ni_5P_4 was produced by design, as it serves to minimize undesired parasitic absorption that occurs when using conformal coatings of this conducting material. Optical measurements were performed on Ni_5P_4/TiN deposited on quartz (q-SiO_2) as well as n^+p-$GaInP_2$ substrates to confirm the spectral losses. Figure 3.2(c) shows the transmittance (T%), reflectance (R%), and absorptance (A%) of the Ni_5P_4/TiN/q-SiO_2. We assumed scattering (S%) is negligible for a polished quartz substrate.[17] The measured absorptance is only 10–15% in the range of 350–700nm wavelengths, which is typical for $GaInP_2$.[12] Comparing the reflectance of bare $GaInP_2$ to Ni_5P_4/TiN/n^+p-$GaInP_2$ (Figure 3.2(d)), reveals that the light loss caused by absorption in the catalyst and protection layers is compensated by a decrease in reflectance. This indicates that the catalyst-protection layer acts as a partial anti-reflective coating. The chemical states of the catalyst and interfacial layer were evaluated by X-ray photoelectron spectroscopy (XPS). Figure 3.3 shows the XPS core level spectra of Ni2p, P2p, Ga2p, and In3d. Both the Ni2p and P2p core levels show the presence of partially oxidized elements. Spectral fitting best describes these as partially oxidized Ni (NiO_x, $2p_{3/2}$: 854.8eV) and phosphorus-oxide (PO_x, $2p_{3/2}$: 132.3 eV), resulting from air-exposure during catalyst synthesis, as previously reported for these catalysts[17,25,26] In addition, a majority component of partially oxidized $Ni^{+\delta}$ ($2p_{3/2}$: 853.8 eV) and reduced $P^{-\delta}$ ($2p_{3/2}$: 129.3 eV) is ascribed to Ni_5P_4, in agreement with previous assignments [17,25,26] Core level spectra in the Ga2p and In3d region show no Ga or In signals, as expected based on

the known mean free path of photoelectrons.[27,28] This confirms that the ultra-thin TiN layer is both conformal and sufficiently robust to prevent atomic diffusion during catalyst formation. Cross-sectional images taken by scanning transmission electron microscopy using high angle

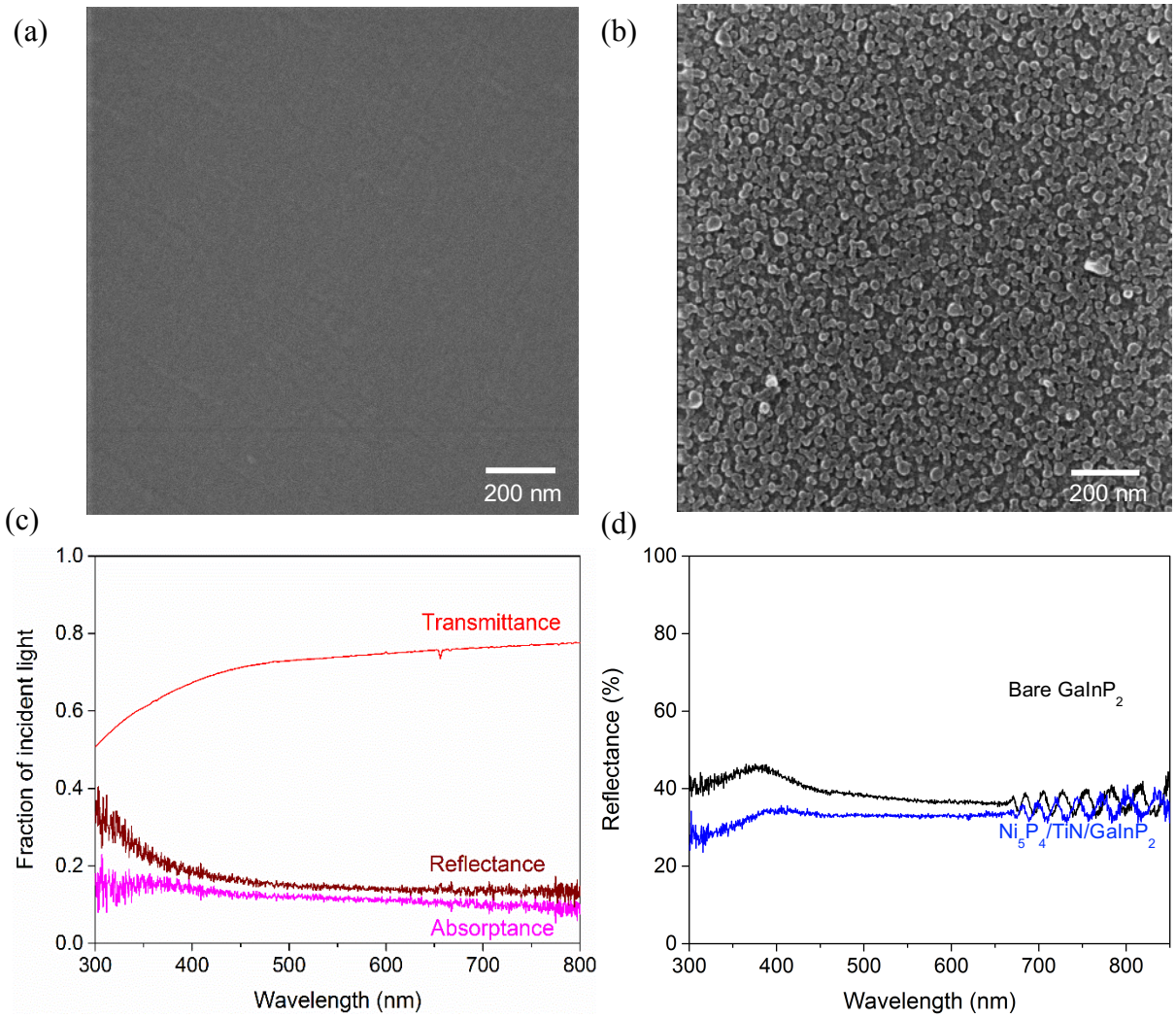

Figure 3.2 Surface morphologies and optical measurements. Helium ion microscope (HIM) image of (a) TiN modified $GaInP_2$ and (b) Ni_5P_4 on TiN/$GaInP_2$. (c) Optical transmittance (red), reflectance (wine) and absorptance (Margenta) of Ni_5P_4/TiN layer on quartz substrate. (d) Reflectance of unmodified bare $GaInP_2$ and Ni_5P_4/TiN modified $GaInP_2$.

annular dark field (STEM-HAADF) and energy dispersive spectroscopy (EDS) maps (Figure 3.4) of the top 80 nm of the device shows the elemental distribution and architecture of the interface. The strong localization of catalyst, protection layer and photoabsorber layers is

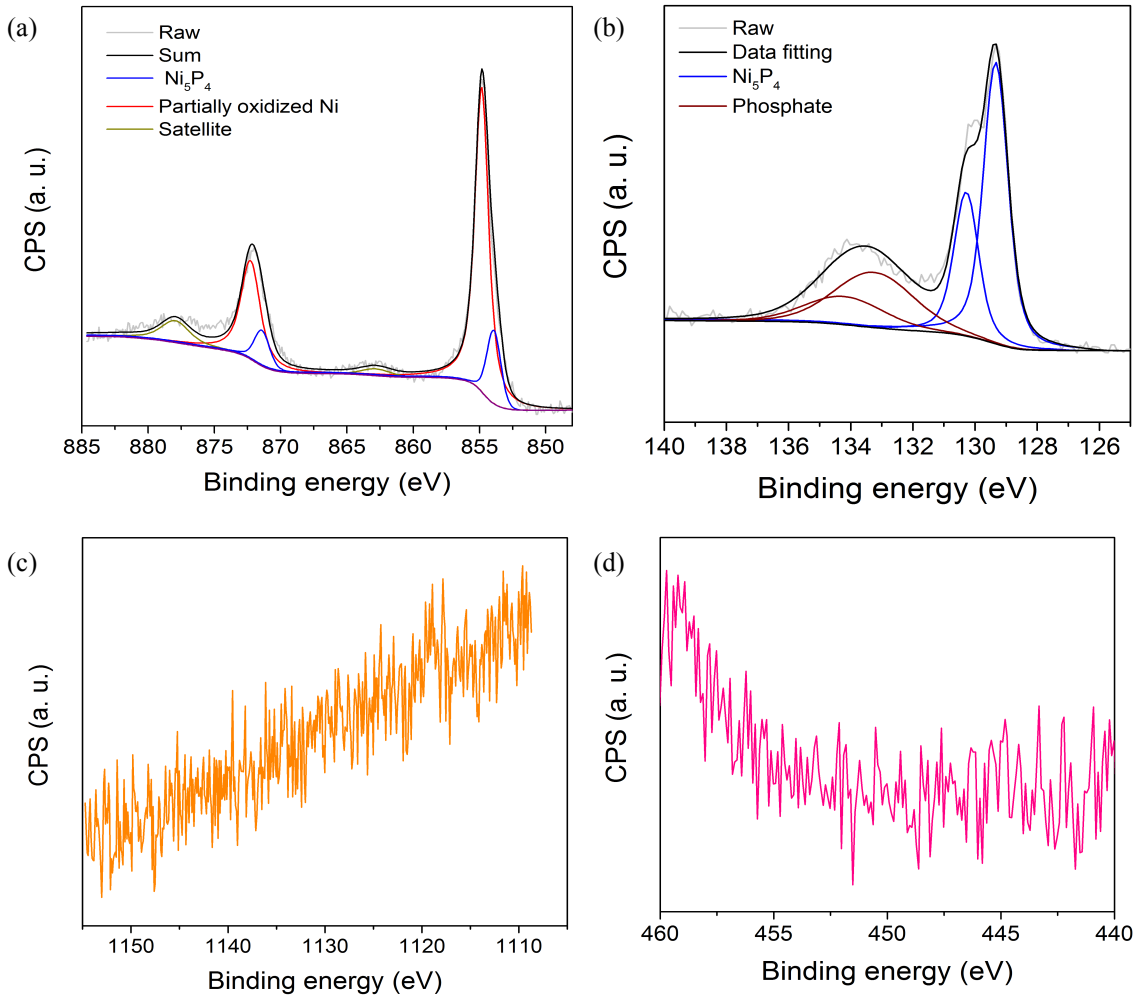

Figure 3.3 X-ray photoelectron spectra of Ni_5P_4/TiN/$GaInP_2$. (a) Ni2p core level. Peaks were deconvoluted to $Ni2p_{3/2}$, and $Ni2p_{1/2}$ for both Ni_5P_4 (blue), and partially oxidized Ni (red). (b) P2p core level. Peaks were deconvoluted to $P2p_{3/2}$, and $P2p_{1/2}$ for both Ni_5P_4(blue), and phosphate (wine). (c) Ga2p core level (d) In3d core level.

demonstrated and in agreement with the HIM images. The formation of crystalline Ni_5P_4 nano-islands was verified by lattice fringe distances of 0.340 and 0.274 (±0.02) nm (Figure 3.5), matching the (110) and (004) d-spacing of Ni_5P_4 respectively. A Fast Fourier Transform (FFT) of the high magnification image (Figure 3.5, inset) also matched the [2-20] zone axis. This is further confirmed by X-ray diffraction analysis of a thick Ni_5P_4 film on Si(100) (using the same synthesis) clearly showing polycrystalline Ni_5P_4 (Figure 3.6). The HAADF image also reveals a 3-4 nm layer under the catalyst of lower contrast. STEM EDS of Ti and N elemental maps identifies this as the TiN protection layer. The absence of both Ga and In (Figure 3.4) in this layer confirms the diffusion barrier properties of TiN during catalyst synthesis. The O-map shows a significant intensity in the TiN region, indicating that the TiN layer contains a

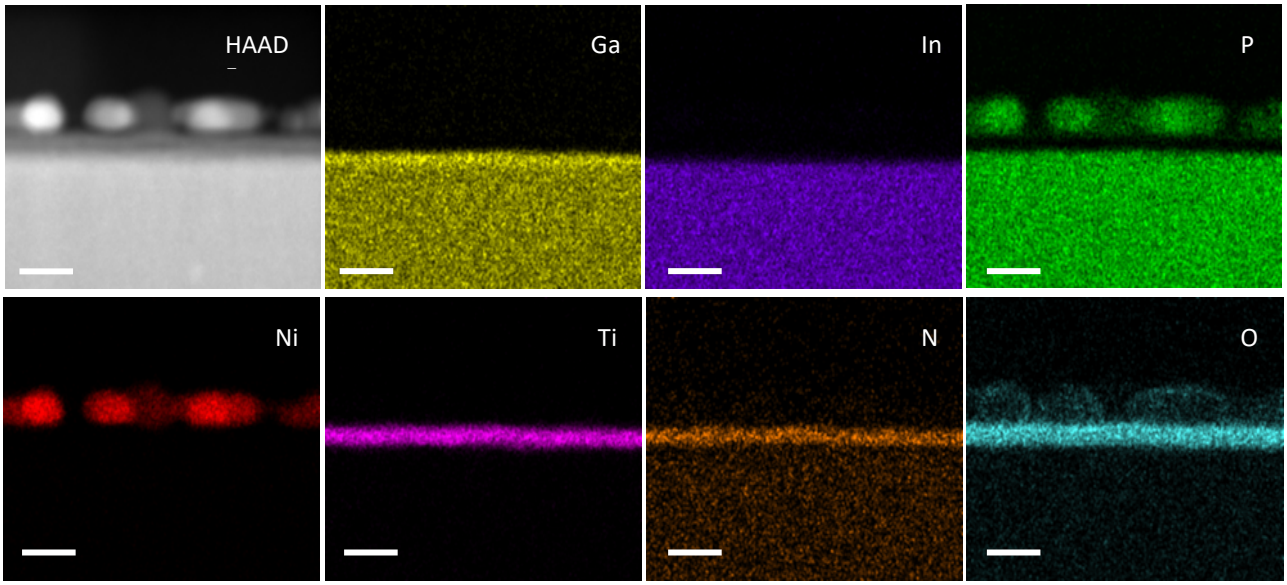

Figure 3.4 Cross-sectional STEM high angle annular dark field (HAADF) image of Ni_5P_4/TiN/$GaInP_2$ and EDS elemental maps of Ga (yellow), In (purple), P (green), Ni (red), Ti (magenta), N (orange), and O (cyan). Scale bars are 20 nm.

significant amount of oxygen. The relatively low temperature (120^0C) and imperfect vacuum level $1x10^{-3}$ Pa during the deposition may be the origin of the relatively high oxygen content in TiN.[29] The presence of an oxide shell covering the Ni_5P_4 catalyst, confirms the XPS assignment of surface nickel (NiO_x) and phosphorus (PO_x) oxides. Ni and P EDS maps confirm the 20–

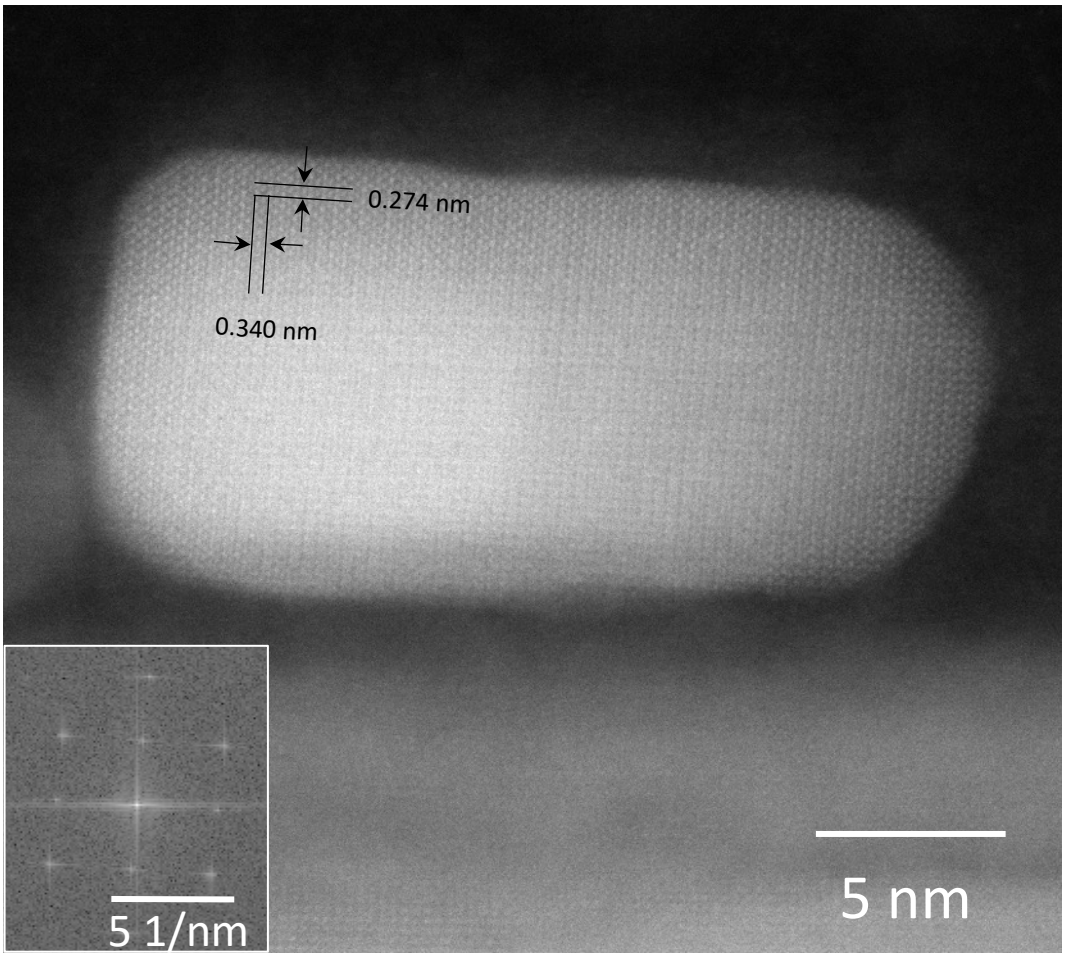

Figure 3.5 High-magnification STEM-HAADF image of a representative Ni_5P_4 island. The measured d-spacing are 0.340 and 0.274 nm, which are matched with (110), and (004) planes of Ni_5P_4. The inset image is FFT of STEM image which is well matched with [2-20] zone axis.

30nm particle diameter.

Photoelectrochemical activity was evaluated in a three-electrode configuration in 0.5M H_2SO_4 with a 1mM Triton X-100 electrolyte (to suppress bubble formation) using simulated 1.5

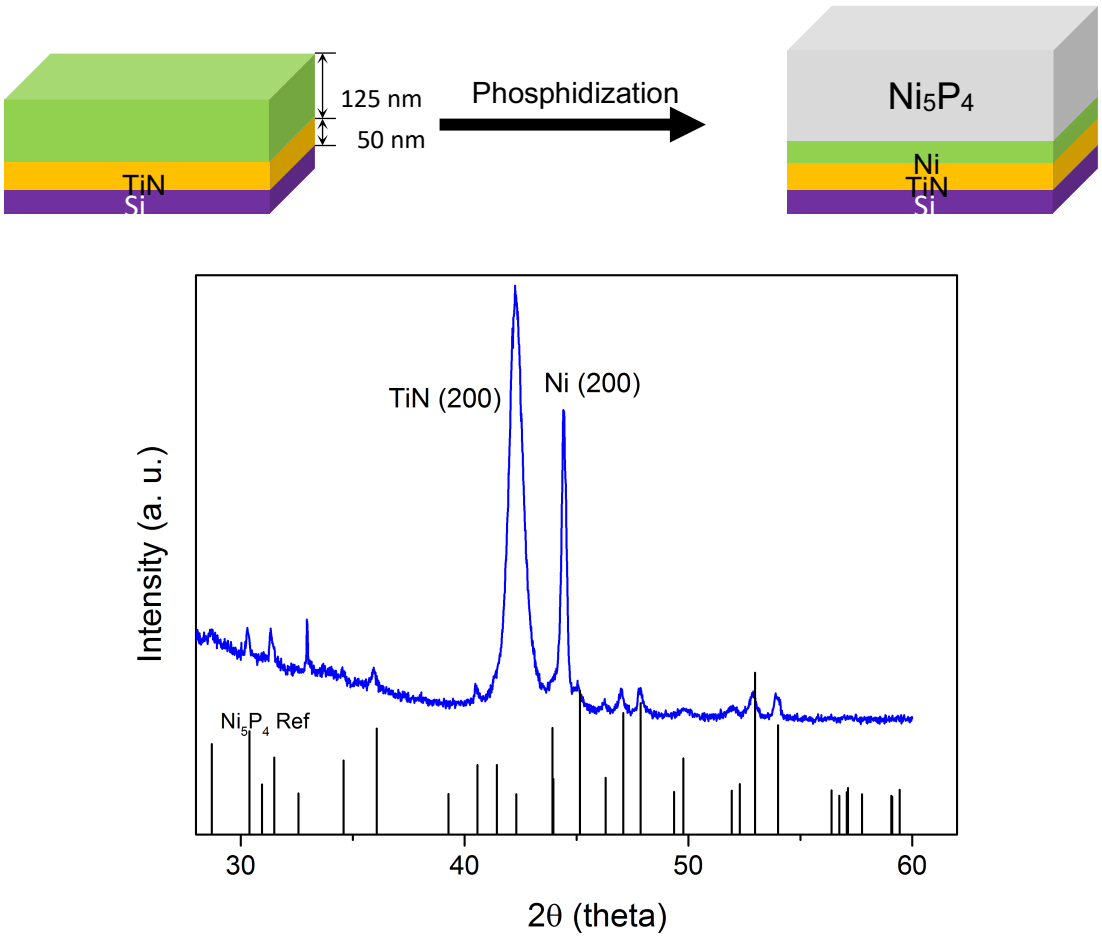

Figure 3.6 Reaction scheme of thick (125nm) Ni_5P_4/Ni/TiN/Si sample preparatio, and X-ray diffraction (XRD) pattern of the thick Ni_5P_4/Ni/TiN/Si sample. When thick Ni_5P_4 films were fabricated, XRD patterns are well matched with reference pattern (PDF 01-089-2588). TiN shows a reflection (200) at 42.2 °, and unreacted Ni shows a reflection (200) at 44.5 °. Unreacted Ni expect to be fully consumed when phosphidation occur with thin-film of Ni (~3nm).

AM G solar illumination (calibrated against a NREL certified $GaInP_2$ reference cell). The catalytic activity of the PtRu/n^+p-$GaInP_2$ benchmark was tested starting with a non-uniform coating of PtRu alloy nanoparticles (2-5nm diameter)[12] This PtRu alloy nanoparticle catalyst is known to outperform both Pt or Ru alone[20] and shows negligible current loss by parasitic absorption.[12] Figure 3.8(a) shows the linear sweep voltammograms (LSVs) of both Ni_5P_4/TiN/n^+p-$GaInP_2$ and PtRu/n^+p-$GaInP_2$. The J-V curve shows the photocurrent onset reaches -1 mA/cm^2 at 1.04 V for Ni_5P_4/TiN/$GaInP_2$ and 0.92 V for the PtRu/$GaInP_2$ benchmark. The positive shift of the photocurrent onset observed for Ni_5P_4/TiN/$GaInP_2$ is likely due to the low intrinsic overpotential of Ni_5P_4 and high loading compared to Pt that we previously reported.[30] The slightly poorer fill factor compared to the PtRu benchmark is probably due to lower charge injection caused by the low crystallinity of TiN.[12,17] An identical saturated photocurrent density (J_{sat} ~ 8.3 mA/cm^2) reveals that the nano-island morphology of the Ni_5P_4 catalyst and ultra-thin TiN are highly transparent and thus do not compromise the limiting photocurrent density. Also, Figure 3.7 shows that the Faradaic efficiency for H_2 production for Ni_5P_4/TiN-n^+p-$GaInP_2$ at saturated current density is 100%, in agreement with electrocatalysis on

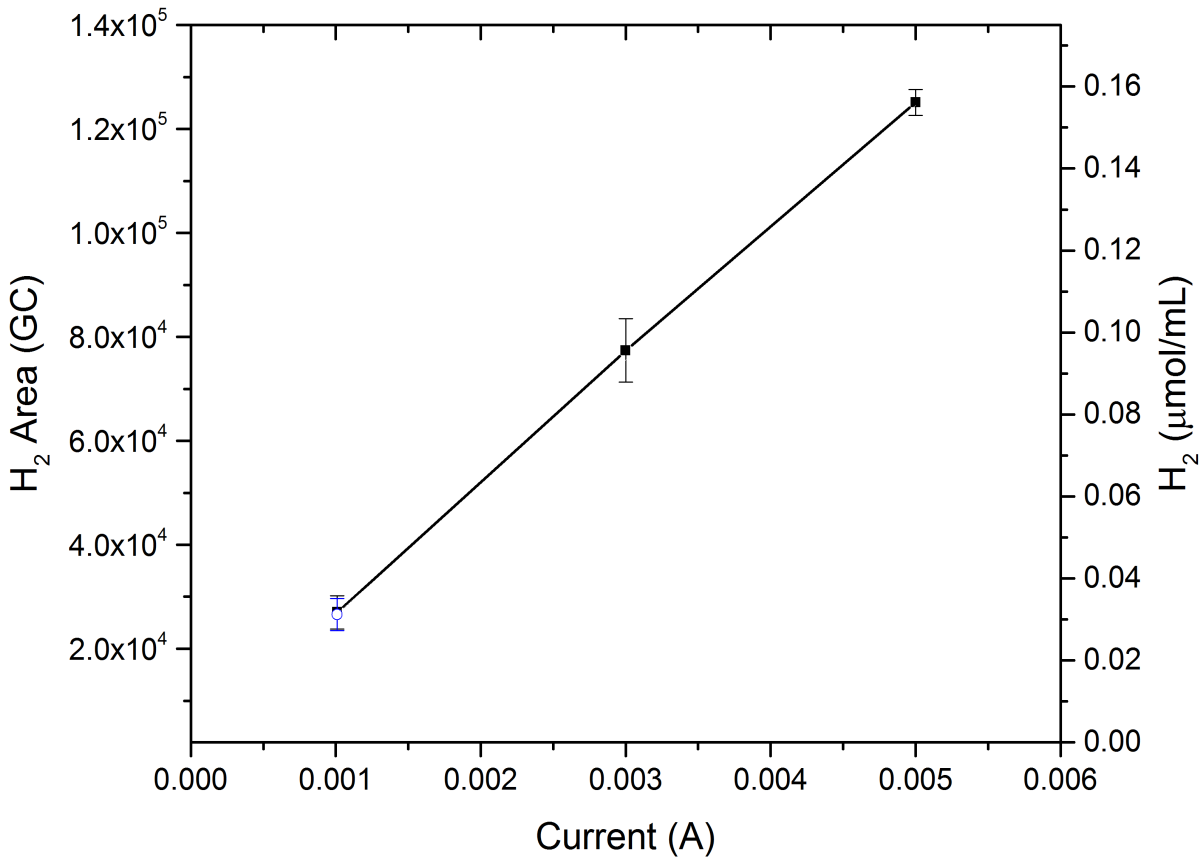

Figure 3.7 Faradaic efficiency test of the calibration curve and Ni_5P_4/TiN/n^+p-$GaInP_2$. A calibration curve (Black, steady-state H_2 as a function of constant current density) was obtained with the Pt foil benchmark.[1] Blue circle corresponds to Ni_5P_4/TiN/n^+p-$GaInP_2$ at a constant current at 0.001 A. The results overlapped with the Pt benchmark within the error bars.

pure Ni_5P_4.[30] Incident photon to current efficiency (IPCE) was measured using the underfill illumination method, allowing accurate control of the device illumination area.[31] The IPCE measurements (Figure 3.8(b)) confirms the nearly identical spectrally resolved photon-conversion efficiency of the nano-island Ni_5P_4/TiN-n^+p-$GaInP_2$ and PtRu/n^+p-$GaInP_2$, in the

range of 375-700nm. Ni_5P_4/TiN/n^+p-$GaInP_2$ show a small increase in IPCE from 300-375nm, which may be attributed to the reduced reflection in this range (Figure 3.2). The IPCE was integrated over a reference solar irradiance standard (global, air mass, 1.5, ASTM G173-3), and used to determine an accurate saturated current density (J^{IPCE}) of ~ 10.2 mA/cm^2 for both photocathodes. This value is higher than that observed by the LSV measurements, which is

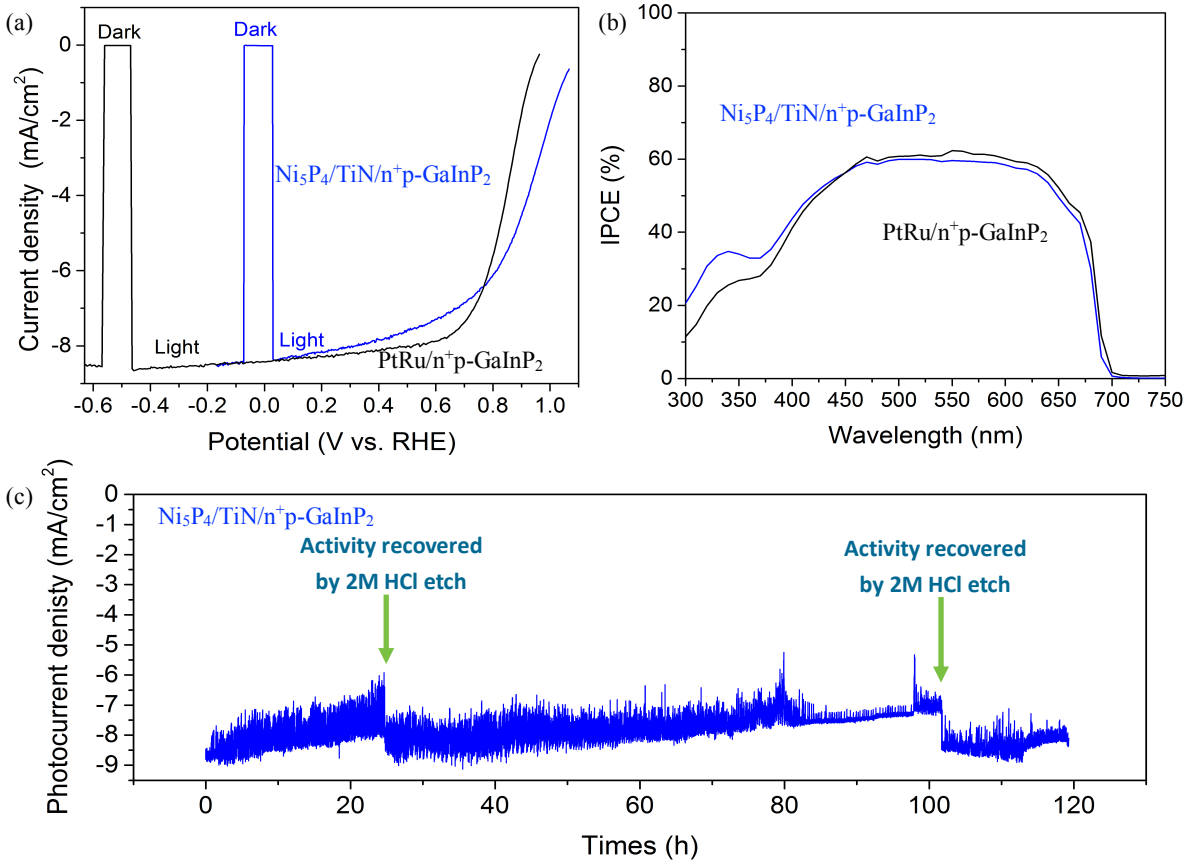

Figure 3.8 (a) LSVs of Ni_5P_4/TiN/n^+p-$GaInP_2$, and PtRu/n^+p-$GaInP_2$ under light and dark conditions. Scan rate was 20 mV/s (b) IPCE of Ni_5P_4/TiN/n^+p-$GaInP_2$, and PtRu/n^+p-$GaInP_2$. (c) CA of Ni_5P_4/TiN/n^+p-$GaInP_2$ at 0.25 V vs. RHE. Time course shows intentional drift caused by electro-plating of Cu onto photocathode and its removal by etching at 24h and 104h.

attributed to slight discrepancies in the active device-area when masked by epoxy for the LSV measurements. Photoelectrochemical stability of the devices was evaluated using chronoamperometry (CA) at + 0.25V vs RHE in 0.5M H_2SO_4 using a copper leads as contact on working electrode. This potential was selected close to the onset of J_{sat} to allow easy monitoring of small changes to device performance during the test and to avoid exaggeration of device

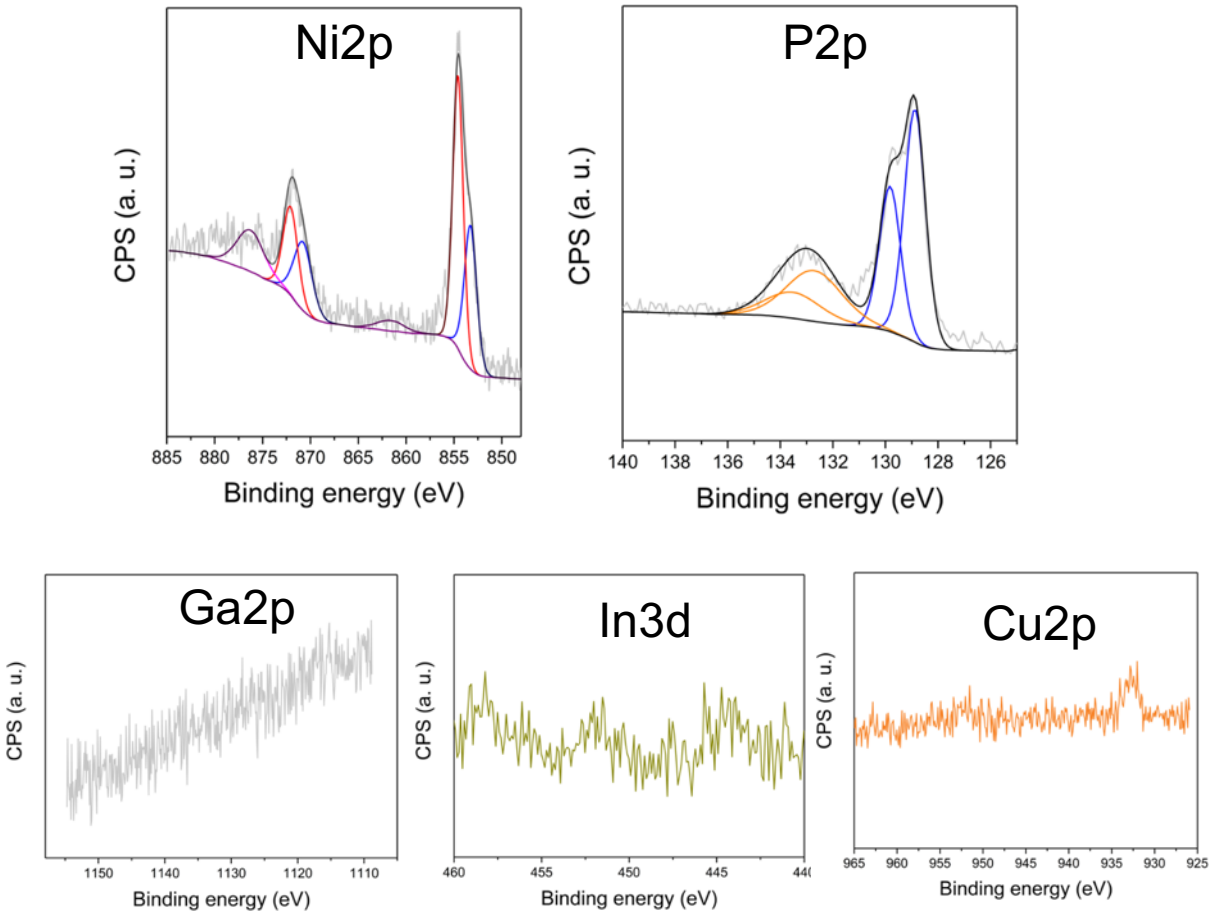

Figure 3.9 X-ray photoelectron spectra of 2M HCl (3s) etched Cu contaminated Ni_5P_4/TiN/n^+p-$GaInP_2$ sample. Cu signal is substantially decreased and Ni and P S/N ratios are recovered.

stability. Figure 3.8(c) shows the CA of Ni_5P_4/TiN/n^+p-$GaInP_2$ photocathode, showing a slow decrease in photocurrent over the first 24h. Post-reaction XPS after this time shows accumulation of metallic Cu plating (Figure 3.9). The source of the Cu contamination was identified as dissolution of the Cu wire and plating on the cathode. The Cu could be selectively removed by

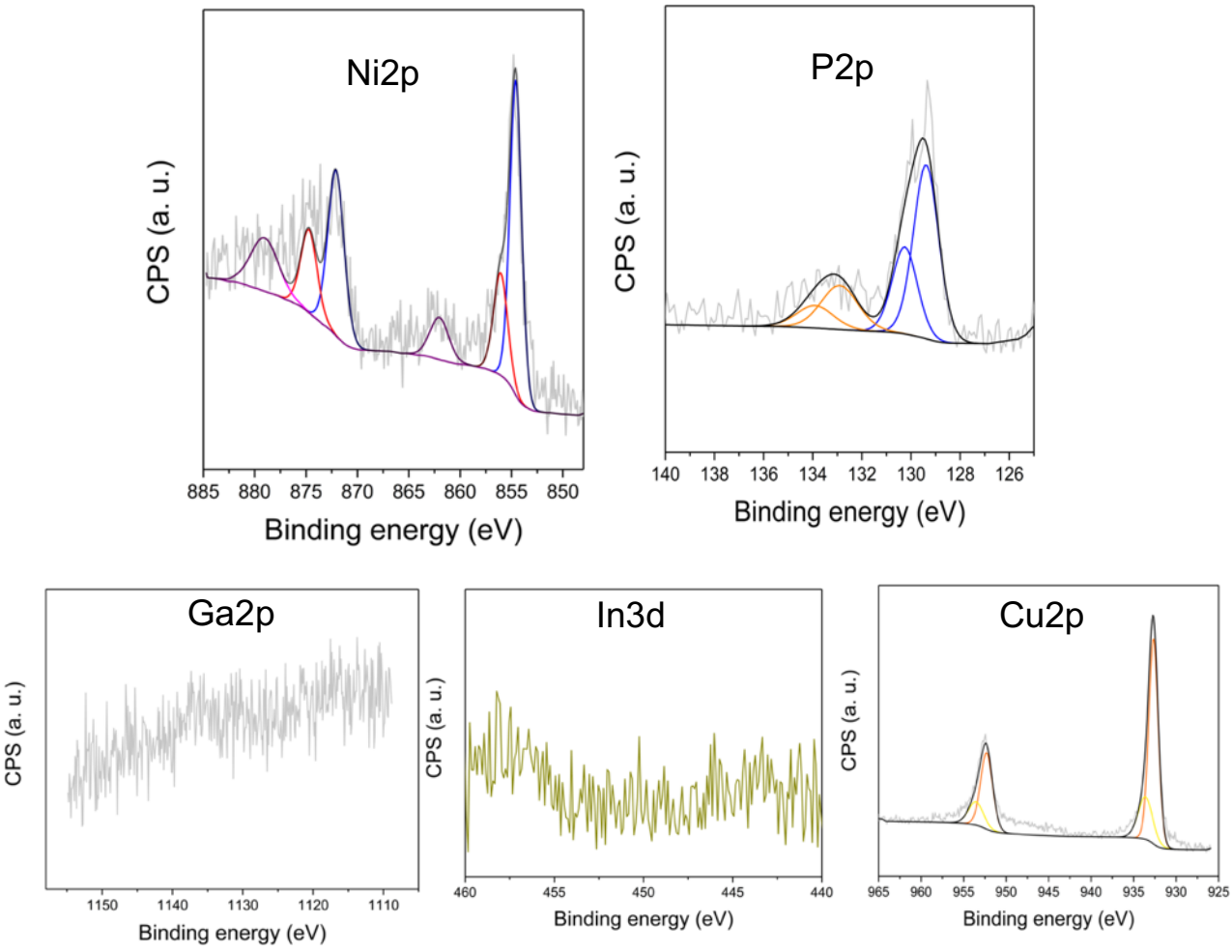

Figure 3.10 X-ray photoelectron spectra of Cu contaminated Ni_5P_4/TiN/n^+p-$GaInP_2$ sample after durability test. Cu2p core level spectra show a clear Cu signal while S/N ratio of Ni and P are decreased.

immersing in 2M HCl for 3s. XPS analysis (Figure 3.9) shows the effective removal of Cu and re-exposure of Ni_5P_4. The CA experiment was continued in the same configuration and the original photocurrent was restored, followed again by slow deterioration in photocurrent over the next 80h (104 h total). The surface was again examined by XPS and found to be contaminated with Cu (data not shown). The HCl etching was repeated and the removal of Cu was confirmed by XPS and the CA continued. Again, the original operating current was restored. After removal of the Cu contaminant, stable device performance was recorded for an additional 20 h with no evidence of current loss before termination of the CA run at 120h (Figure 3.8(c)). By contrast, CA analysis of PtRu/n^+p-$GaInP_2$ (Figure 3.11) shows the photocurrent decreases within 3h, even in the presence of a more cathodically passivating applied potential (-0.78 V vs. RHE). This decrease is primarily due to photo-corrosion/dissolution of $GaInP_2$ in the acidic electrolyte.[9] In conclusion, the nano-island Ni_5P_4-TiN catalyst-protection layer performs on par with the PGM-nanoparticle catalyst without protection layer, with respect to catalytic activity and limiting photocurrent density, while exhibiting greatly superior corrosion stability in electrolyte and even tolerance to mild etching to remove Cu contamination.

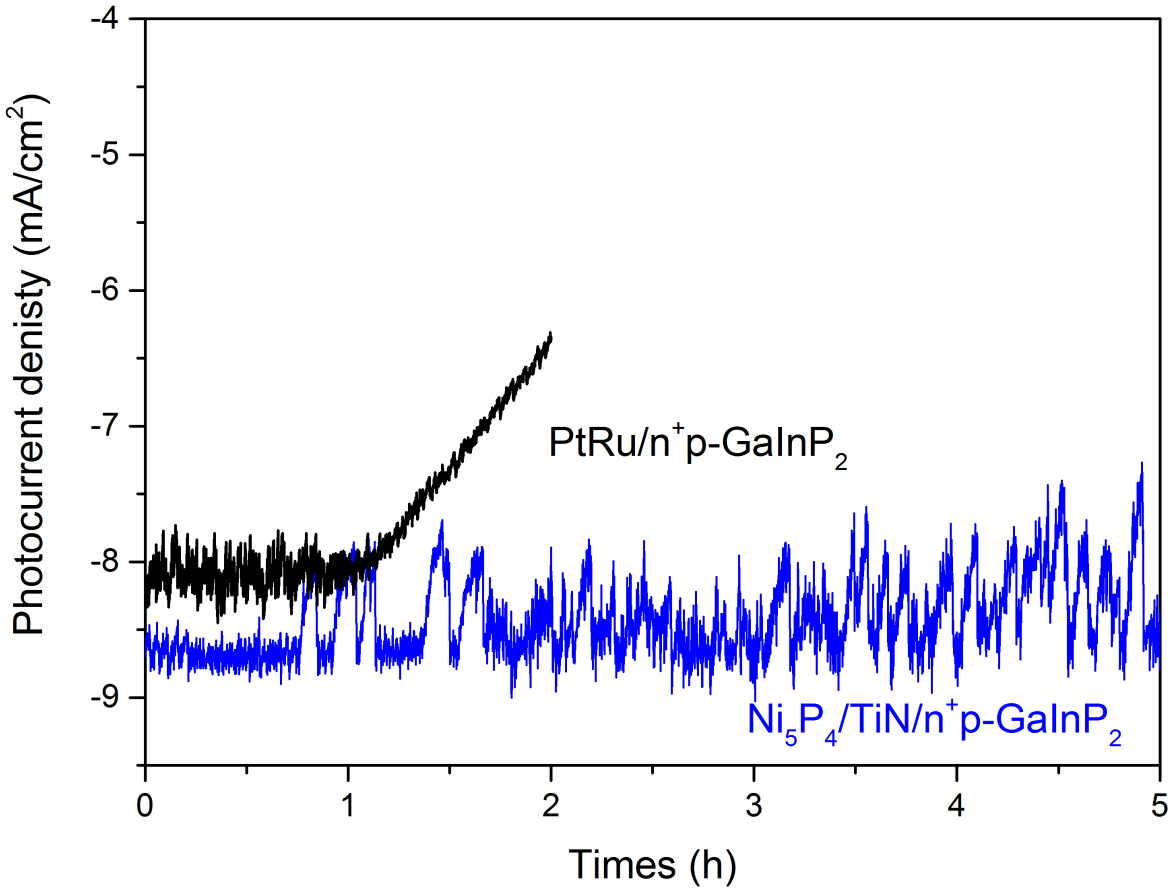

Figure 3.11 5 hours chronoamperograms of PtRu/n$^+$p-GaInP$_2$ and Ni$_5$P$_4$/TiN/n$^+$p-GaInP$_2$ in 0.5 M H_2SO_4. Potential was held at -0.78 V vs. RHE, and +0.25 V vs. RHE for of PtRu/n$^+$p-GaInP$_2$ and Ni$_5$P$_4$/TiN/n$^+$p-GaInP$_2$, respectively.

3.5 Conclusions

In summary, we describe the fabrication and performance of a PGM-free photocathode consisting of highly transparent nano-islands of Ni_5P_4 synthesized on a TiN protection layer on top of n$^+$p-GaInP$_2$. STEM/EDS and XPS analysis reveal a conformal, ultra-thin, TiN coating that

effectively hinders interatomic-diffusion during the high temperature catalyst synthesis. Faradaic efficiency and saturated photocurrent density identical to that of state-of-the art PtRu/n^+p-$GaInP_2$ benchmark is achieved. The resulting photocathode has negligible parasitic absorption and reflection losses. We show that the catalyst-protection layer provides superior operational stability for at least 120h with undiminished performance. Etching, to remove copper surface contamination on the operating photocathode, restores the original photocurrent and HER activity, demonstrating the potential for ruggedness and extended lifetime essential for commercial applications.

3.6 Acknowledgments

This work was supported by the U.S. Department of Energy, Office of Energy Efficiency and Renewable Energy, Fuel Cell Technologies Office Award#DE-EE0008083.

Authors thank to Thermo Fisher Scientific for TEM sample preparation and STEM/EDS mapping.

3.7 References

(1) Peters, G. P.; Andrew, R. M.; Boden, T.; Canadell, J. G.; Ciais, P.; Le Quéré, C.; Marland, G.; Raupach, M. R.; Wilson, C. The Challenge to Keep Global Warming Below 2 °C. *Nature Climate Change 2012 3:1* **2012**, *3* (1), 4.

(2) Lewis, N. S.; Nocera, D. G. Powering the Planet: Chemical Challenges in Solar Energy Utilization. *PNAS* **2006**, *103* (43), 15729–15735.

(3) Wang, X.; Palazoglu, A.; El-Farra, N. H. Operational Optimization and Demand Response of Hybrid Renewable Energy Systems. *Applied Energy* **2015**, *143*, 324–335.

(4) Turner, J.; Sverdrup, G.; Mann, M. K.; Maness, P. C.; Kroposki, B.; Ghirardi, M.; Evans, R. J.; Blake, D. Renewable Hydrogen Production. *Int. J. Energy Res.* **2008**, *32* (5), 379–407.

(5) Navarro, R. M.; Sánchez-Sánchez, M. C.; Alvarez-Galvan, M. C.; del Valle, F.; Fierro, J. L. G. Hydrogen Production From Renewable Sources: Biomass and Photocatalytic Opportunities. *Energy Environ. Sci.* **2009**, *2* (1), 35–54.

(6) Goto, Y.; Hisatomi, T.; Wang, Q.; Higashi, T.; Ishikiriyama, K.; Maeda, T.; Sakata, Y.; Okunaka, S.; Tokudome, H.; Katayama, M.; et al. A Particulate Photocatalyst Water-Splitting Panel for Large-Scale Solar Hydrogen Generation. *Joule* **2018**, *2* (3), 509–520.

(7) Kocha, S. S.; Montgomery, D.; Peterson, M. W.; Turner, J. A. Photoelectrochemical Decomposition of Water Utilizing Monolithic Tandem Cells. *Sol. Energy Mater. Sol. Cells* **1998**, *52* (3-4), 389–397.

(8) Prévot, M. S.; Sivula, K. Photoelectrochemical Tandem Cells for Solar Water Splitting. *J. Phys. Chem. C* **2013**, *117* (35), 17879–17893.

(9) Khaselev, O.; Turner, J. A. Electrochemical Stability of P - GaInP2 in Aqueous Electrolytes Toward Photoelectrochemical Water Splitting. *J. Electrochem. Soc.* **1998**, *145* (10), 3335–3339.

(10) Britto, R. J.; Benck, J. D.; Young, J. L.; Hahn, C.; Deutsch, T. G.; Jaramillo, T. F. Molybdenum Disulfide as a Protection Layer and Catalyst for Gallium Indium Phosphide Solar Water Splitting Photocathodes. *J. Phys. Chem. Lett.* **2016**, *7* (11), 2044–2049.

(11) Gu, J.; Yan, Y.; Young, J. L.; Steirer, K. X.; Neale, N. R.; Turner, J. A. Water Reduction by a P-GaInP2 Photoelectrode Stabilized by an Amorphous TiO2 Coating and a Molecular Cobalt Catalyst. *Nat. Mater.* **2016**, *15* (4), 456–460.

(12) Gu, J.; Aguiar, J. A.; Ferrere, S.; Steirer, K. X.; Yan, Y.; Xiao, C.; Young, J. L. O.; Al-Jassim, M.; Neale, N. R.; Turner, J. A. O. A Graded Catalytic–Protective Layer for an Efficient and Stable Water-Splitting Photocathode. *Nature Energy* **2017**, *2* (2), 16192.

(13) Wang, Y.; Schwartz, J.; Gim, J.; Hovden, R.; Mi, Z. Stable Unassisted Solar Water Splitting on Semiconductor Photocathodes Protected by Multifunctional GaN Nanostructures. *ACS Energy Letters* **2019**, 1541–1548.

(14) Laursen, A. B.; Pedersen, T.; Malacrida, P.; Seger, B.; Hansen, O.; Vesborg, P. C. K.; Chorkendorff, I. MoS 2 —an Integrated Protective and Active Layer on N + P-Si for Solar H 2 Evolution. *Phys. Chem. Chem. Phys.* **2013**, *15* (46), 20000–20004.

(15) Benck, J. D.; Lee, S. C.; Fong, K. D.; Kibsgaard, J.; Sinclair, R.; Jaramillo, T. F. Designing Active and Stable Silicon Photocathodes for Solar Hydrogen Production Using Molybdenum Sulfide Nanomaterials. *Adv. Energy Mater.* **2014**, *4* (18).

(16) Young, J. L.; Steiner, M. A.; Döscher, H.; France, R. M.; Turner, J. A.; Deutsch, T. G. Direct Solar-to-Hydrogen Conversion via Inverted Metamorphic Multi-Junction Semiconductor Architectures. *Nature Energy* **2017**, *2* (4), 17028.

(17) Hwang, S.; Porter, S. H.; Laursen, A. B.; Yang, H.; Li, M.; Manichev, V.; Calvinho, K. U. D.; Amarasinghe, V.; Greenblatt, M.; Garfunkel, E.; et al. Creating Stable Interfaces Between Reactive Materials: Titanium Nitride Protects Photoabsorber–Catalyst Interface in Water-Splitting Photocathodes. *J. Mat. Chem. A* **2019**, *7* (5), 2400–2411.

(18) Biunno, N.; Narayan, J.; Hofmeister, S. K.; Srivatsa, A. R.; Singh, R. K. Low-Temperature Processing of Titanium Nitride Films by Laser Physical Vapor Deposition. *Appl. Phys. Lett.* **1989**, *54* (16), 1519.

(19) Libardi, J.; Grigorov, K. G.; Massi, M.; da Silva Sobrinho, A. S.; Pessoa, R. S.; Sismanoglu, B. Diffusion of Silicon in Titanium Dioxide Thin Films with Different Degree of Crystallinity: Efficiency of TiO2 And TiN Barrier Layers. *Vacuum* **2016**, *128*, 178–185.

(20) McKone, J. R.; Pieterick, A. P.; Gray, H. B.; Lewis, N. S. Hydrogen Evolution From Pt/Ru-Coated P-Type WSe2 Photocathodes. *J. Am. Chem. Soc.* **2012**, *135* (1), 223–231.

(21) MacLeod, B. A.; Steirer, K. X.; Young, J. L.; Koldemir, U.; Sellinger, A.; Turner, J. A.; Deutsch, T. G.; Olson, D. C. Phosphonic Acid Modification of GaInP2 Photocathodes Toward Unbiased Photoelectrochemical Water Splitting. *ACS Appl. Mater. Interfaces* **2015**, *7* (21), 11346–11350.

(22) Friedman, D. J.; Kurtz, S. R.; Bertness, K. A.; Kibbler, A. E.; Kramer, C.; Olson, J. M.; King, D. L.; Hansen, B. R.; Snyder, J. K. Accelerated Publication 30.2% Efficient GaInP/GaAs Monolithic Two-Terminal Tandem Concentrator Cell. *Prog. Photovolt. Res. Appl.* **1995**, *3* (1), 47–50.

(23) Lee, C.-T.; Shiao, H.-P.; Yeh, N.-T.; Tsai, C.-D.; Lyu, Y.-T.; Tu, Y.-K. Thermal Reliability and Characterization of InGaP Schottky Contact with Ti/Pt/Au Metals. *Solid-State Electronics* **1997**, *41* (1), 1–5.

(24) Postek, M. T.; Vladar, A. E. Helium Ion Microscopy and Its Application to Nanotechnology and Nanometrology. *Scanning* **2008**, *30* (6), 457–462.

(25) Kibsgaard, J.; Tsai, C.; Chan, K.; Benck, J. D.; Nørskov, J. K.; Abild-Pedersen, F.; Jaramillo, T. F. Designing an Improved Transition Metal Phosphide Catalyst for Hydrogen Evolution Using Experimental and Theoretical Trends. *Energy Environ. Sci.* **2015**, *8* (10), 3022–3029.

(26) Laursen, A. B.; Wexler, R. B.; Whitaker, M. J.; Izett, E. J.; Calvinho, K. U. D.; Hwang, S.; Rucker, R.; Wang, H.; Li, J.; Garfunkel, E.; et al. Climbing the Volcano of Electrocatalytic Activity While Avoiding Catalyst Corrosion: Ni 3P, a Hydrogen Evolution Electrocatalyst Stable in Both Acid and Alkali. *ACS Catal.* **2018**, *8* (5), 4408–4419.

(27) Tanuma, S.; Powell, C. J.; Penn, D. R. Calculations of Electron Inelastic Mean Free Paths. III. Data for 15 Inorganic Compounds Over the 50–2000 eV Range. *Surf. Interface Anal.* **1991**, *17* (13), 927–939.

(28) Lebedev, M. V.; Calvet, W.; Kaiser, B.; Jaegermann, W. Synchrotron Photoemission Spectroscopy Study of P-GaInP2(100) Electrodes Emersed From Aqueous HCl Solution Under Cathodic Conditions. *J. Phys. Chem. C* **2017**, *121* (16), 8889–8901.

(29) Chowdhury, R.; Vispute, R. D.; Jagannadham, K.; Narayan, J. Characteristics of Titanium Nitride Films Grown by Pulsed Laser Deposition. *J. Mater. Res.* **1996**, *11* (6), 1458–1469.

(30) Laursen, A. B.; Patraju, K. R.; Whitaker, M. J.; Retuerto, M.; Sarkar, T.; Yao, N.; Ramanujachary, K. V.; Greenblatt, M.; Dismukes, G. C. Nanocrystalline Ni5P4 : A Hydrogen Evolution Electrocatalyst of Exceptional Efficiency in Both Alkaline and Acidic Media. *Energy Environ. Sci.* **2015**, *8* (3), 1027–1034.

(31) Döscher, H.; Young, J. L.; Geisz, J. F.; Turner, J. A.; Deutsch, T. G. Solar-to-Hydrogen Efficiency: Shining Light on Photoelectrochemical Device Performance. *Energy Environ. Sci.* **2016**, *9* (1), 74–80.

Chapter 4: $SrNbO_2N$ Thin Films as Photoanodes for Solar-driven Water Oxidation

4.1 Abstract

Photoelectrochemical (PEC) water splitting devices for storing solar energy as hydrogen/oxygen products are widely sought at large-scale. However, to realize this goal, two essential requirements are fabrication using earth-abundant elements and a multi-junction configuration using wide and narrow bandgap (tunable) photoabsorbers to efficiently collect the solar spectrum. In this study, we investigated methods to create thin films of bandgap-tunable oxynitrides, targeting $SrNbO_2N$ as the wide bandgap photoabsorber in tandem with silicon. Herein we report synthesis of $SrNbO_2N$ thin-films on crystalline silicon using TaN to prevent inter-diffusion at high temperature. The optical band gap (1.9 eV), work function (E_{vac}-E_F = -4.90 eV), and the valance energy level (E_F-E_{val} = -1.76eV) were experimentally determined for this n-type semiconductor and used to construct the energy level diagram and their band edge positions needed for water oxidation. Photoelectrochemical oxidation of ferrocyanide was employed as a low barrier redox couple in solution to determine the significant influence that oxynitride thickness, crystallite size, and electrochemical surface roughness play in photoanode performance across a wide range of these variables. Finally, photoelectrochemical water oxidation was performed with RuO_x water oxidation catalyst. These materials and metrics provide the basis for PEC applications.

4.2 Introduction

The intermittent nature of most renewable energy sources requires a need for large-scale energy storage. Energy can be stored safely, conveniently, and with high density as chemical bonds. H2 derived from solar water splitting devices is one key preferred renewable energy carrier allowing for conventional gas transport and long-term storage before conversion to electricity via fuel cells.[1] Current photoelectrochemical (PEC) devices for water electrolysis suffer from one or more pitfalls, including low stability, high cost, and/or low efficiency. Devices, to address these problems have been investigated, comprised of two sequential solar light absorbers (semiconductors) bonded to two catalysts for the oxygen evolution reaction (OER) and hydrogen evolution reaction (HER). This tandem photoabsorber/OER/HER catalysts approach can increase the theoretical solar to hydrogen (STH) efficiency from 12% to 22%.[2] Improvements are required, because even best-in-class systems using this approach run only tens to hundreds of hours before failure[3] and most operate below <17% efficiency.[4,5] Of the four most common PEC configurations for water splitting,[6] the "artificial leaf" configuration[7] has gained popularity due to its simple design and ease of scaling. This configuration can be further simplified by the elimination of ohmic contacts to create a wireless device, but at the cost of lower efficiency. To improve performance of this configuration, while still maintaining simplicity, the requirements addressed herein include: better spectral matching of the semiconductors, formation of optically thin films with low scattering losses and diffusion barriers.

Tandem cell photoabsorbers employing single crystal silicon (E_g = 1.1 eV) as the low bandgap material require a wide bandgap material for optimal solar capture efficiency

(approximately 1.8 eV).[8] Many perovskite oxynitrides have bandgaps that lie near this value [9-11] and have been found to be good candidates for PEC devices.[12-16] Partial or full incorporation of nitrogen into an oxide host lattice reduces the bandgap considerably by adding N 2p electronic states that are less electronegative than the O 2p dominated valence band maximum, for example lowering the gap from 3.9 eV to 2.1 eV as one coverts from from $Sr2Nb_2O_7$ to $SrNbO_2N$.[17]

Porous and thick films of SrNbO2N have been created from pre-synthesized microparticles using electrophoretic deposition[18] or a particle transfer method on conductive electrodes,[13,19] and these photoanodes carry out PEC water splitting if supplemented with an externally applied bias.[13] Both methods are capable of testing the pre-synthesized powders but they often result in unstable interfaces between particle and conductive substrate,[20] and they leave one with limited control of the thickness and roughness that are needed to optimize attenuation and carrier diffusion lengths for metal nitride and metal oxide semiconductors.[21-23] Thin-film fabrication methods allow control of these variables, and are well suited for use with crystalline Si to create a tandem device. However, due to the high-temperature needed for ammonolysis to convert the oxide into an oxynitride, it has been extremely challenging to make a SrNbO2N film without intermixing at the Si interface.[24] Kawashima et al.,[20] demonstrated the formation of a crystalline film of nominally SrNbO2N on a Nb substrate, but significant reduction to Nb4+ occurred resulting in parasitic absorption in the near-IR and low PEC performance. A recent study from Kikuchi et al.,[25] demonstrated one-step epitaxial growth of $SrNbO_2N$ on $SrTiO_3$ by RF reactive sputtering. This study showed that $SrNbO_2N$ has an indirect bandgap (1.81 eV) and low carrier mobility, despite a low electron mass, due to the trapping of electrons in grain boundaries.[25] In that work, some variables (such as film thickness) were not

optimized with respect to photoelectrochemical responses. To achieve higher incident photon-to-current efficiency (IPCE) in these materials, these properties need to be fully understood.

In this work, thin-film cubic TaN was prepared as an interfacial diffusion barrier between Strontium niobium oxide thin-films and crystalline Si substrate prior to ammonolysis to $SrNbO_2N$. Cubic-TaN has metallic properties needed for low impedance interfaces, and due to its high density and low formation energy (per atom),[26,27] it has been widely used as a diffusion barrier for metals on Si under high-temperature processing conditions.[27,28] We characterized the valence and conduction electronic states of $SrNbO_2N$ with emphasis on the determination of the states near the Fermi level and their position relative to water redox potentials. Using the photoelectrochemical oxidation of ferrocyanide as a function of film thickness and roughness, we demonstrated that these variables significantly affect the photovoltage and photocurrent performance of $SrNbO_2N$. We compare it to the OER activity under 0.1 M KOH with and without catalyst coating.

4.3 Experimental

Materials

$Sr(NO_3)_2$ (Sigma, 99.99%), $NbCl_5$ (Alfa, 99.9%), citric acid (Sigma, 99%), TaN target (Kurt J. Lesker, 99.5%), n^+-Si (100) (University wafer, As-doped, 0.005 ohm cm^{-1}) and 200 proof ethanol (Fisher Scientific, 100%) were used as received.

Preparation of the $SrNbO_2N$/TaN thin film on Si and quartz

n^+-Si (100) substrates were cleaned with acetone, ethanol, and deionized water followed by 5 min in a Buffered Oxide Etch (BOE) solution, 6:1 vol. NH_4F/HF, prior to introduction into a pulsed laser deposition (PLD) vacuum chamber. Pulsed laser ablation of TaN and $Sr_2Nb_2O_7$ targets were carried out using a KrF excimer laser Compex 205 (λ = 248 nm, d = 7 cm, 10 Hz, 2.5 – 5 J cm^{-2}; Coherent).[29] The chamber base pressure was kept at $5 – 7 \times 10^{-4}$ Pa. TaN deposition was carried out using the TaN target under a partial pressure of ultra-high purity nitrogen (P_{N2}: 6.7 Pa, 700 °C). Except for the X-ray diffraction study, the thickness of TaN was maintained in the range of 5-10 nm. $Sr_2Nb_2O_7$ target was ablated at P_{N2}: 26.7 Pa, 700 °C right after the TaN deposition. Only the ablation time was varied for different thicknesses of the oxide films. The films were converted to the oxynitride, $SrNbO_2N$, by a post-anneal in a tube furnace (NH_3 atmosphere at 250 mL/min, 840°C dwell for 1-2 h, and 20°C/min ramp up). The $Sr_2Nb_2O_7$ target for PLD was prepared by uniaxially pressing (105 MPa) $Sr_2Nb_2O_7$ powder, then sintering at 1400°C for 15 h with a 10°C/min ramp and cool. Details of the $Sr_2Nb_2O_7$ powder synthesis are reported elsewhere.[24] For optical measurements, $SrNbO_2N$/TaN layers were deposited on a quartz substrate (Advalue technology, USA) as noted above, except that the ammonolysis anneal was limited to 820 °C to prevent atomic diffusion of SiO_2.

Physical/chemical characterizations

X-ray diffraction (XRD) was carried out on a Bruker D8 Advance (Cu Kα1, 0.02° step size, 15-20 sec dwell time). Rutherford backscattering spectrometry (RBS) were collected using the Rutgers 1.7 MV General Ionex Tandetron. The incident beam energy was 2.0 MeV, and recoiled helium ions were measured with a standard ORTEC Si surface barrier detector

(scattering angle (δ) = 163°, energy resolution ~17 keV). The RBS data were analyzed using the SIMNRA program. [30] Helium ion microscopy was carried out in an Orion Plus Helium Ion Microscope (ZEISS). Operating acceleration voltage and ion beam current are at a 30 kV and 1 pA, respectively. Atomic force microscopy (AFM) images were generated with a Park Systems NX-10 with a Nanosensors PPP-NCHR tip in electrostatic force mode at room temperature in air. Work functions are extracted from the contact potential difference between the sample surface and the AFM/KPFM (Kelvin probe force microscopy) tip (MikroMasch NSC15/CR-AU). The latter was derived from ultraviolet photoelectron spectroscopy (work function = 4.25 eV). For X-ray photoelectron spectroscopy measurements, a Thermo K-Alpha spectrometer was used with charge compensation; spectra were calibrated against adventitious carbon (284.8 eV). UV-vis diffuse reflectance was carried out on $SrNbO_2N$/TaN/quartz using a 300 W Xe arc lamp (Oriel) with integrating sphere (Si photonics) equipped with Flame S detector (Ocean Optics).

Photoelectrochemical measurements

Photoelectrochemical oxidation of ferrocyanide was measured in a 1x5 cm^2 glass cuvette cell (FireflySci, Inc.) in 0.1 M $K_4[Fe(CN)_6]$/1 mM $K_3[Fe(CN)_6]$ with 0.1 M KOH (pH 13.0) using a Bio-logic potentiostat (VSP-300). The working electrodes were illuminated by simulated 1.5 AM G generated by a 300 W Xe arc lamp (ORIEL), which was calibrated against a $GaInP_2$ reference solar cell (NREL). The distance between the glass window and the working electrode was kept at 1 mm. Pt wire (BASi) was used for the counter electrode, and a mercury/mercury oxide (1 M NaOH) reference electrode (CH Instrument) was used. The reference electrode

potential was calibrated against the reversible hydrogen electrode (RHE, freshly cleaned Pt electrode at 1 atm. H_2) before each measurement. For RuO_x deposition, 0.48 mM of $RuCl_3 \cdot xH_2O$ was dissolved in 1 M potassium phosphate buffer, and passing 200 $\mu C/cm^2$ under the dark condition.

4.4 Results and discussions

To investigate the crystal structure of the $SrNbO_2N$ film and underlying TaN interfacial layer, X-ray diffraction was employed. For this purpose, thicker TaN (~ 100 nm) and $SrNbO_2N$ (~ 200 nm) films were prepared on Si (100) substrates to obtain clear diffraction patterns. XRD patterns of fabricated $SrNbO_2N$/TaN, and TaN films on Si were compared to reference patterns cubic-TaN (PDF 01-089-5196) and $SrNbO_2N$ (PDF 01-073-7849) (Figure 4.(a)). The XRD pattern of TaN/Si (black) is well matched with the reference pattern of cubic-TaN (magenta), which indicate that the given deposition conditions form phase pure cubic-TaN. XPS analysis of TaN/Si also confirms that the major Ta oxidation state appears close to that expected for Ta^{3+} (23.8 eV) and it contains lattice N^{3-} (396.9 eV) (Figure 4.1). Due to the high-temperature ammonolysis, $SrNbO_2N$/TaN films (blue) have high crystallinity and the diffraction pattern of $SrNbO_2N$ is well matched with that of the $SrNbO_2N$ reference pattern, which confirms that the fabricated film is phase pure. No additional XRD peaks resulting from undesired impurities such as $TaSi_2$ or $SrSiO_3$ are present, confirming that the TaN film is a good diffusion barrier under high-temperature ammonolysis conditions.

The elemental composition of the $SrNbO_2N$ film was measured by RBS on a thick $SrNbO_2N$ film with a thin TaN layer to minimize the heavy element contribution from Ta

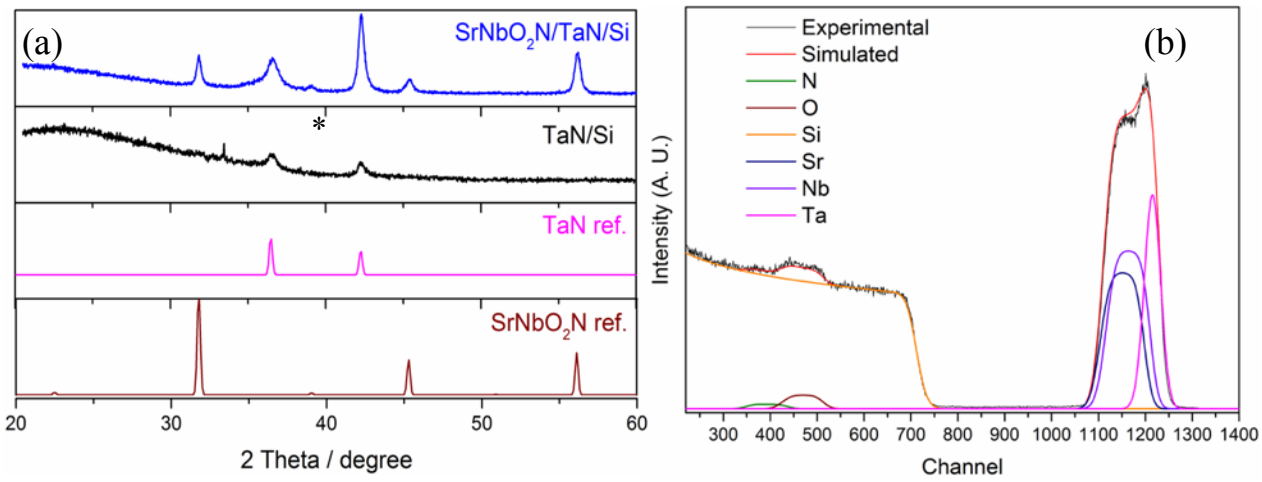

Figure 4.1 (a) X-ray diffraction for (top to bottom) $SrNbO_2N$/TaN/Si, TaN/Si, and reference patterns of cubic-TaN, and $SrNbO_2N$. *: Si(200) diffraction (b) Rutherford backscattering spectrum of $SrNbO_2N$/TaN/Si film. Simulated model was used to match the experimental $SrNbO_2N$/TaN/Si data.

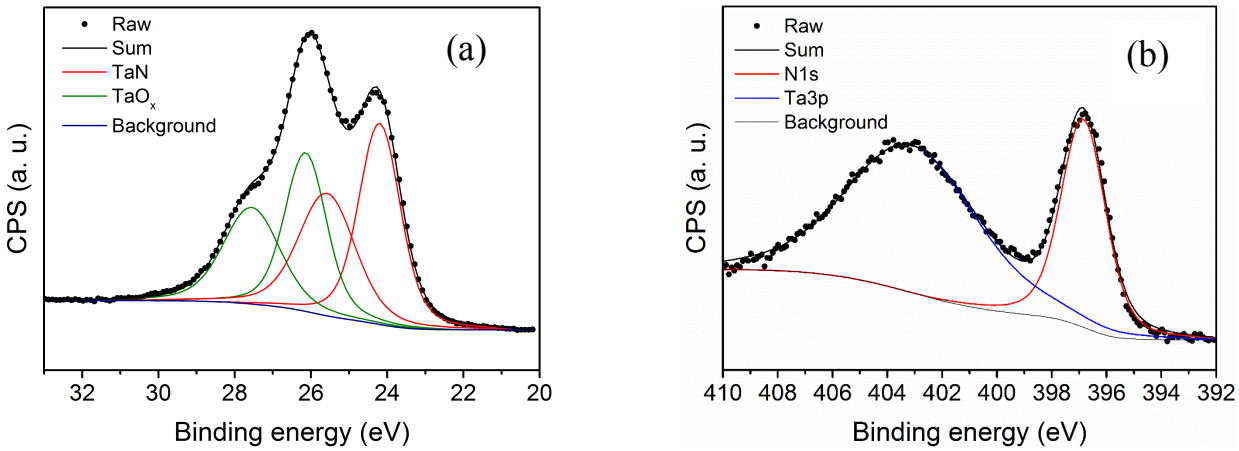

Figure 4.1 X-ray photoelectron spectra of TaN on Si. (a) Ta4f, and (b) N1s. In Ta4f, there are two species, TaN and surface TaO_x which are deconvoluted to $Ta4f_{7/2}$, and $Ta4f_{5/2}$. The N1s spectrum overlaps with Ta3p. The binding energy of 396.9 eV indicates lattice N^{3-}.

(which overlaps with Sr and Nb for thicker Ta-based films). Figure 4.1(b) indicates that the

composition of the sample can be described as a single layer of approximate composition, $SrNbO_{2.25}N_{0.92}$ with a thin $Ta_{0.4}N_{0.3}O_{0.3}$ interfacial layer. The equal ratio of Sr to Nb confirms the PLD target deposition and that the post-anneal heating does not cause significant diffusion of Sr or Nb into SrO_x or NbO_xN_y. RBS results also confirm the incorporation of N into the film, however, it is worth noting that the strong background from the Si substrate decreases the accuracy of N determination.[31] More detailed analysis of anion species is described below section.

Chemical states of $SrNbO_2N$ film

Probing the chemical states of $SrNbO_2N$ is important to identify defects (e.g., Nb^{4+}) that can act as trap sites during photoelectrochemical reactions.[20,32] Figure 4.2 shows Nb3d, Sr3d, N1s, and O1s XPS core level spectra. In the $SrNbO_2N$ film, the Nb3d spectra are comprised of a sharp doublet at 206.5 and 209.2 eV corresponding to the expected spin-orbit coupling of $3d_{5/2}$ and $3d_{3/2}$, respectively. The shape, intensity, and location of this doublet is similar to that reported for Nb^{5+} in bulk $Sr_2Nb_2O_7$[33] and $SrNbO_2N$.[34] Further confirmation of the Nb^{5+} valence comes from a report showing that this doublet matches that reported in a recent study of Mg-doped $SrNbO_2N$, which claimed substantial suppression of Nb^{4+} after substitution of Mg in the B site.[18] The Sr3d spectra were deconvoluted to a sharp doublet at binding energies 135.3 eV and 133.6 eV, attributable to the spin-orbit coupling of $Sr3d_{3/2}$ and $Sr3d_{5/2}$, respectively for the Sr^{2+} oxidation state.[35] For the N1s core level spectra, the observed peak with binding energy near 396 eV demonstrates the substitution of lattice nitride (N^{3-}) into the oxide lattice, which is quite

distinct from that caused by physisorbed surface nitrogen(~400 eV).[13] The strong N1s peak and absence of Nb^{4+} indicate that the fabricated films have stoichiometry $SrNbO_{3-x}N_x$ (x =

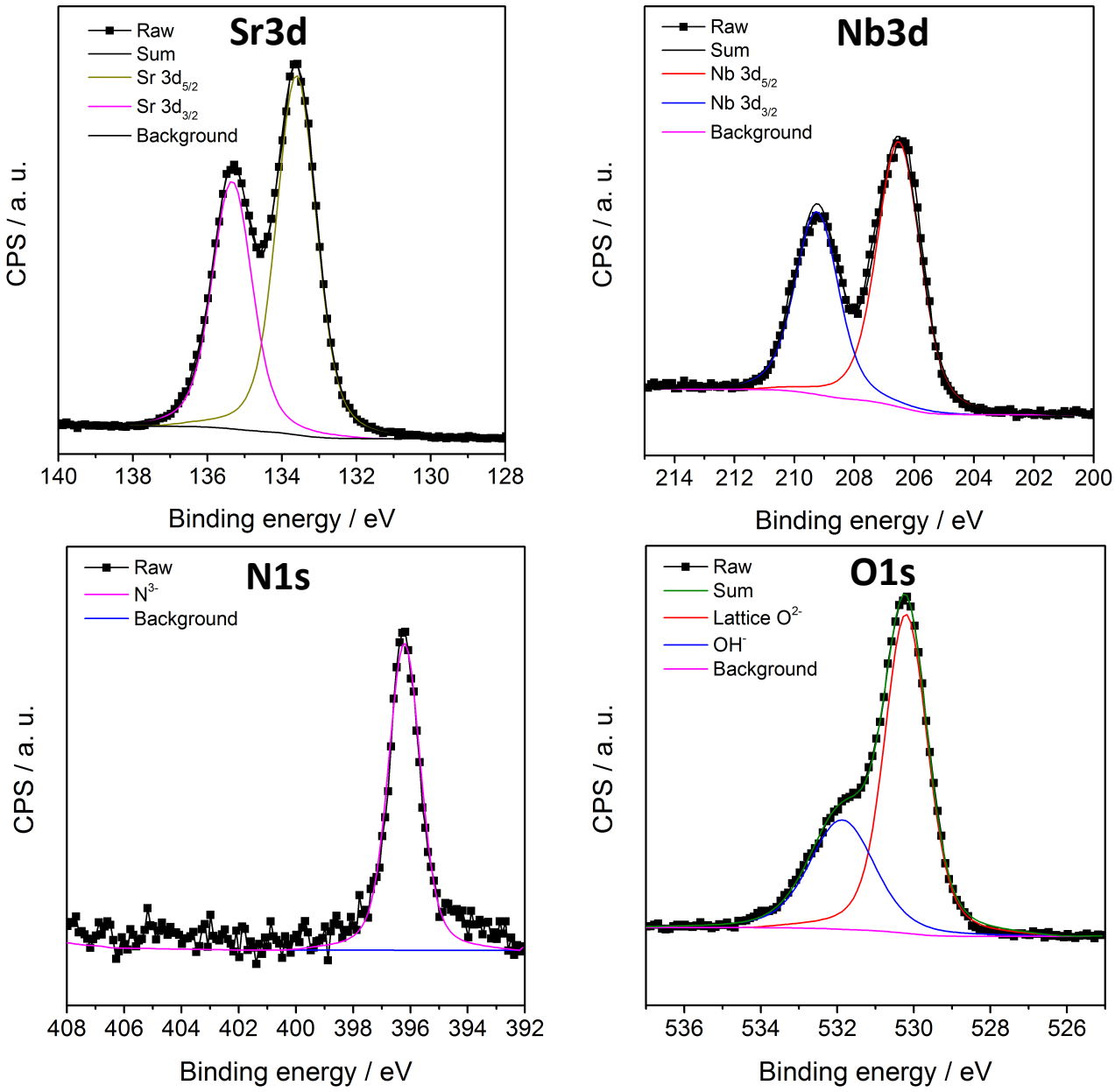

Figure 4.2 X-ray photoelectron core-level spectra of $SrNbO_2N$/TaN/Si film (a) Nb3d, (b) Sr3d, (c) N1s, and (d) O1s.

0.96-1.02).[36] This composition is also supported by the O1s spectra showing two features: dominant lattice O^{2-} and smaller surface absorbed OH^- centered at binding energies of 530.1 eV and 531.8 eV, respectively.

Film morphologies and roughness factor

Understanding how surface morphological changes correlate with photoelectrochemical performance is crucial for optimizing the device. Helium ion microscopy (HIM) was used to probe the film morphologies (top-view) and to determine the film thickness (when

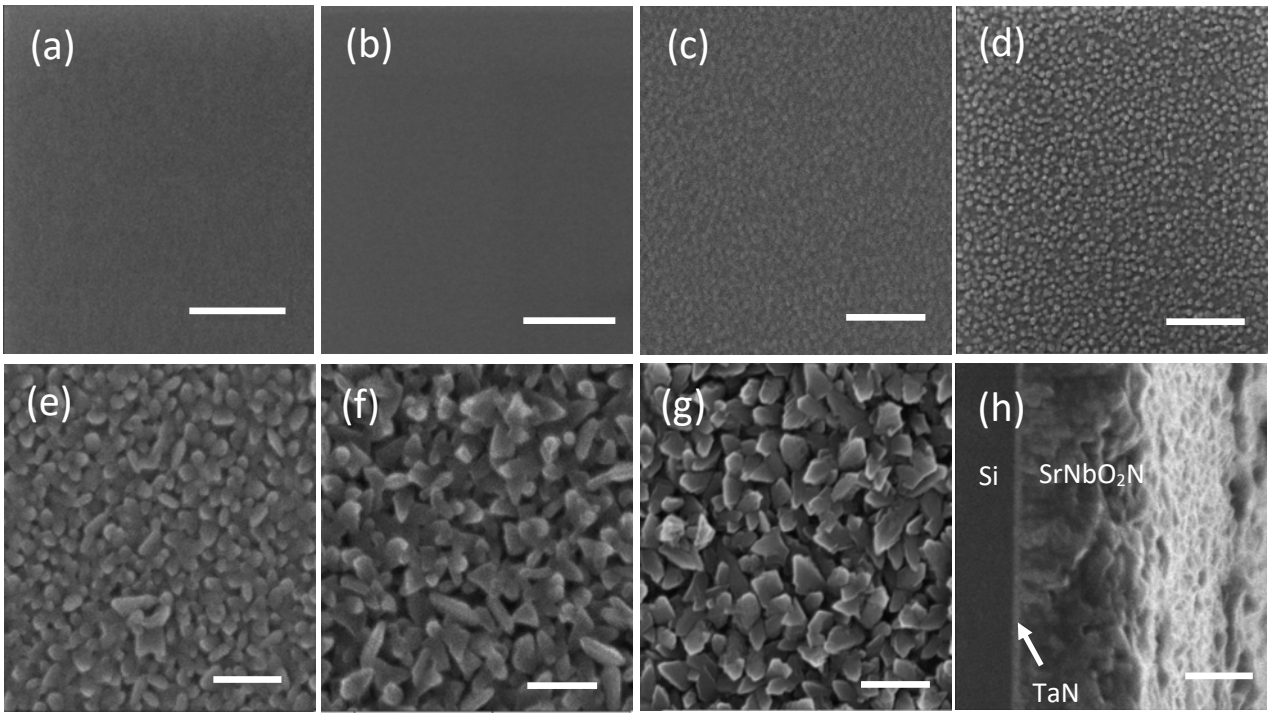

Figure 4.3 Helium ion microscope (HIM) images of (a) bare Si, (b) 5 nm TaN/Si (c) 21 nm $SrNbO_2N$/TaN/Si (d) 92 nm $SrNbO_2N$/TaN/Si (e) 158 nm $SrNbO_2N$/TaN/Si, (f) 334 nm $SrNbO_2N$/TaN/Si, (g) 440 nm $SrNbO_2N$/TaN/Si, and (h) cross-sectional view of 334 nm $SrNbO_2N$/TaN/Si. All scale bars are 200 nm.

imaged in cross-section). Figure 4.3(a-h) shows the top morphologies of bare Si, TaN/Si, and different thicknesses of the $SrNbO_2N$ thin-films. Figure 4.3a-b show top view HIM images of the bare Si (100) substrate and a TaN thin film on Si (5-10 nm TaN thin-films were studied). The featureless image of the TaN film indicates that the thin film is pin-hole free and follows the atomically smooth morphology of the Si (100) substrate. Cross-sectional HIM images of a $SrNbO_2N$/TaN/Si structure, shown in Figure 4.3(h), validates that a 5-10 nm TaN film uniformly coats the Si substrate, and that it was sufficient to prevent atomic interdiffusion during high-temperature ammonolysis. Cross-sectional images of five different thicknesses of $SrNbO_2N$ films are shown in Figure 4.4 and were used to determine the thickness of the films given in Table 1.

Samples	**(c)**	**(d)**	**(e)**	**(f)**	**(g)**
Thickness (nm)	21 ± 2	92 ± 3	158 ± 5	334 ± 8	440 ± 9

Table 4.1 HIM determined thickness of $SrNbO_2N$ films.

When the thickness of the film is less than 100 nm, (Figure 4.3b-c), the surface of films appears as 10-20 nm diameter grains. For thicker $SrNbO_2N$ films, >150 nm, the images (Figure 4.3e-g) show non-spherical grains, with dimensions varying between 10 nm and 100 nm in any given grain. A similar feature can be found in the cross-sectional images (Figure 4.4), where film thickness >150 nm starts to add porosity in the structure due to

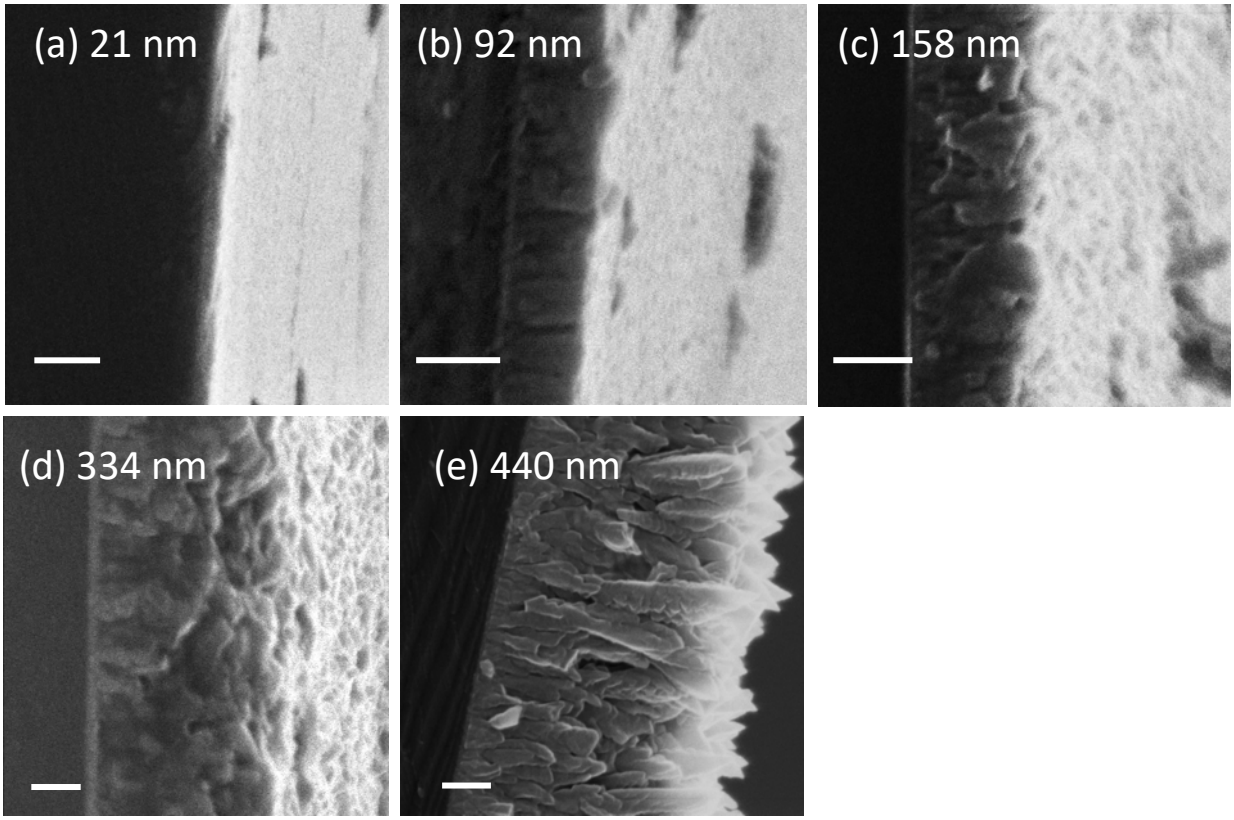

Figure 4.4 Cross-sectional helium ion microscope (HIM) images of different thickness $SrNbO_2N$ thin-films on TaN/Si. All scale bars are 100 nm.

larger grain sizes. Both top and side views indicate that controlling the thickness of $SrNbO_2N$ films not only changes the thickness, but also modifies the grain size, morphology and packing (porosity).

The HIM images show the change of film morphology, but they have a limited capability to determine the exact roughness factor of the films. To probe changes in film roughness as a function thickness, non-Faradaic electrochemical capacitance measurements were performed on $SrNbO_2N$ films under dark conditions.[37] Capacitive currents were measured between 0.7 V and 0.9 V vs. RHE, where no Faradaic process occurs. Capacitive current

density vs. scan rate, shown in Figure 4.5, gives the capacitance/area value. 40 μF/cm^2 was set as a roughness factor 1.[38] Similar to grain size observations, as the thickness of the film

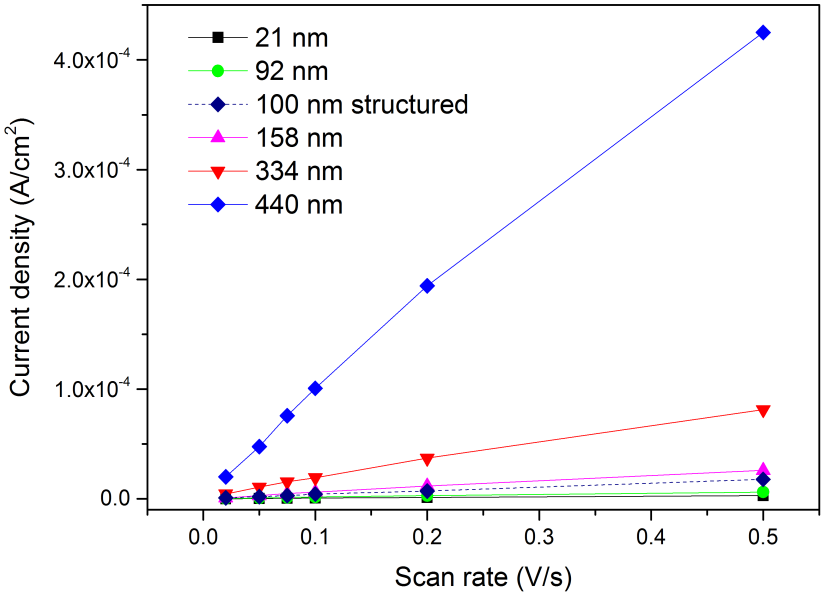

Figure 4.5 Electrochemical capacitive current density vs. scan rate for different thickness of $SrNbO_2N$ thin-films. "Structured" is the device fabricated on a nanostructured Si substrate; all others are on planar Si.

Thickness	Roughness factor
21 nm	0.14
92 nm	0.31
100 nm (structured)	0.87
158 nm	1.30
334 nm	4.00
440 nm	21.00

Table 4.2 Roughness factor of each $SrNbO_2N$ thickness measured by electrochemical capacitance. "Structured" is the device fabricated on a nanostructured Si substrate; all others are on planar Si.

increases, the roughness factor increases from very small (<1) below a thickness of 100 nm, increasing with film thicknesses over 150 nm. At a thickness of 440 nm, the roughness factor dramatically increased to 21, probably due to the large grains with increased poroisity, as demonstrated in Figure 4.3(g) and Figure 4.4(e).

Energy level diagram of $SrNbO_2N$ film

Understanding the valence and conduction electronic states of thin film semiconductors provides key diagnostic information for evaluating photoelectrochemical water splitting activity and electrode stability/corrosion. We used three methods to determine the energy level of $SrNbO_2N$ film: valence-resolved XPS to determine the energy separation between the Fermi level and the valence band DOS,[14] UV-visible diffuse reflectance to determing the band gap (E_g),[39-41] and Kelvin force microscopy to determine the work function relative

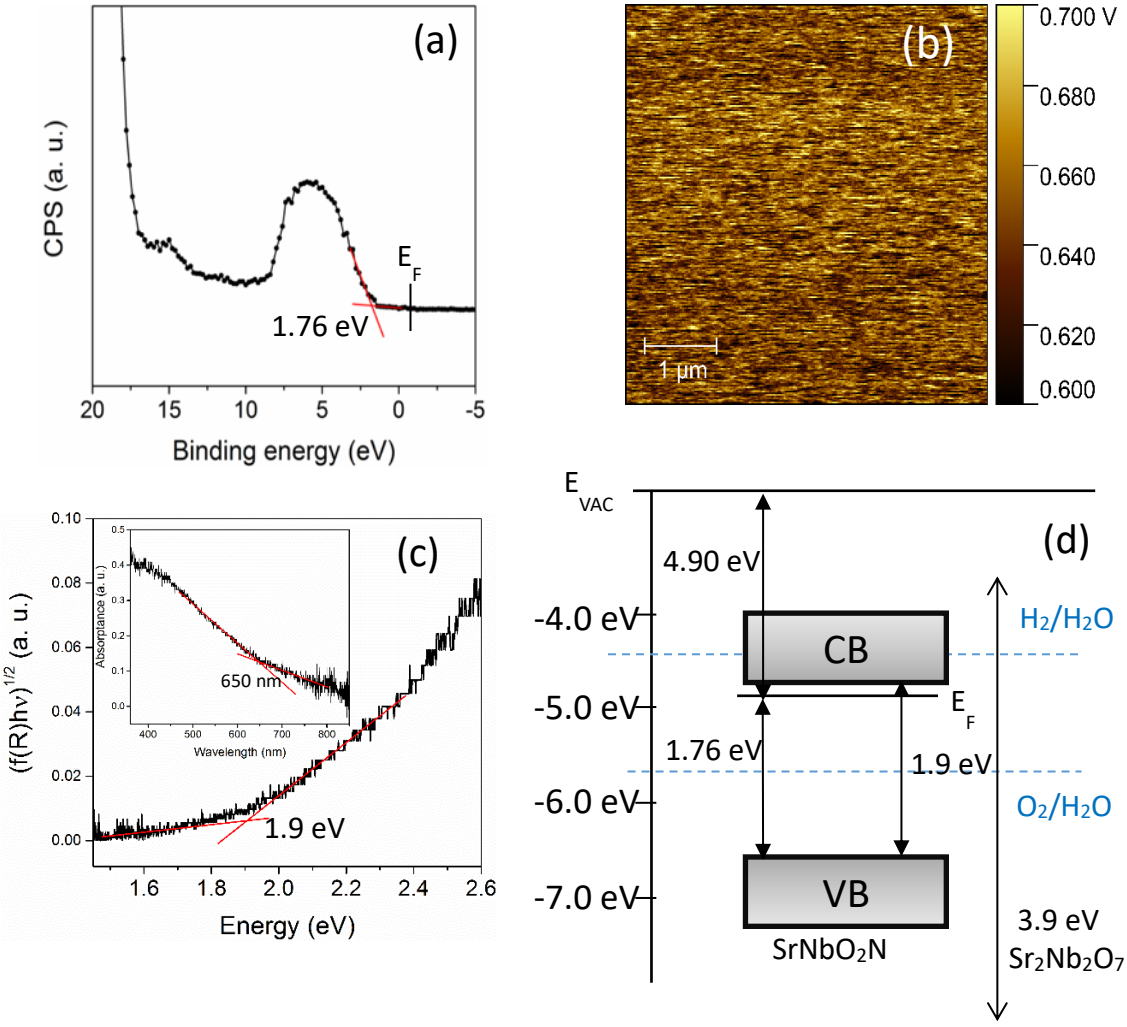

Figure 4.6 (a) XPS valence band spectra of a $SrNbO_2N$ thin film. The valence band edge was determined by the linear extraporation of two lines. (b) Kelvin probe force microscope derived contact potential difference surface map for $SrNbO_2N$.(c) Tauc plot and UV-VIS diffuse reflectance (inset) of the $SrNbO_2N$ thin film. The inflection in the absorptance and Tauc plots was determined by intersection of the two lines determined by linear regression.(d) Composite, experimental energy states for $SrNbO_2N$ compared to E_{vac} and the water redox potentials. The E_g is from UV-vis DRS, VB to E_F is from XPS, and E_F is from KPFM, which allow estimation energy levels of $SrNbO_2N$. The bandgap (3.9 eV) and estimated band edges of $Sr_2Nb_2O_7$ presented for the reference.[17]

to E_{vac}.[9,42,43] Two implicit assumptions were made in our measurements: that significant chemical changes do not occur on going from surface to bulk and that grain boundary charging in these samples is negligible.

In the valence XPS spectra, the threshold for the valance band absorption was observed at -1.76 eV vs zero binding energy (Figure 4.6a). This observed E_F to E_{VB} energy spacing is consistent with other compounds in this class, where ATa(O,N)$_3$ (A = Ca, Sr, Ba, Pr^{3+}) ranges from 0.85-2.84 eV.[44]

In Figure 4.6b, $SrNbO_2N$ has an optical band gap of 1.9 eV, and it has a relatively short tail at a wavelength higher than 700 nm. The weak long-wavelength absorption tail has been explained as either niobium reduction during ammonolysis or defects.[9] IR light scattering due to the grain size refraction also contributes. Low absorption at long wavelengths (near IR), is a necessary property for the larger bandgap material in tandem photoabsorber devices, and the optical measurement shown in Figure 4.6b demonstrates that fabricated $SrNbO_2N$ films are suitable for this purpose.

A 10 x 10 μm survey of the film by Kelvin probe force microscopy provided an averaged contact potential difference (CPD) value between the Au AFM tip and $SrNbO_2N$, 648 mV (± 20mV). The sample had uniform CPD values with no irregular or anomalous features observed (Figure 4.6c). The work function of the sample versus E_{vac} was calculated to be -4.90 eV. This value is in-line with those derived for ATaO_2N (A = Ca, Sr, Ba) perovskites.[44]

The energy levels of the valence band maxmium(-6.6 eV vs. Vac) the Fermi level (XPS), the bandgap (1.9 eV), the conduction band minimum (UV-vis DR) and the work function (-4.9 eV vs. Vac) (KPFM) are related to each other as shown in Figure 4.6d.[9] From this

emerges a more complete picture of the energy level digram of $SrNbO_2N$. The $SrNbO_2N$ Fermi level position lies near the top of the bandgap, indicating that this semiconductor is n-type. The absolute conduction and valence band positions can be compared to the E_{vac} level, and, compared to the potential for water oxidation (-5.67 eV).[45] $SrNbO_2N$ has a conduction band minimum 0.46 eV lower than the water reduction potential. The valence band maximum locates at 0.99 eV more negative than the water oxidation potential. With its near optimal bandgap and position of the valence band maximum (VBM) lower than the water oxidation potential, this material can be used as a photoanode to drive water oxidation in a tandem device. Compared to powder $SrNbO_2N$ measurements, this sample has a more negative conduction band minimum (~ 0.5 eV).[18] The absence of Nb^{4+} and the partial replacement of O^{2-} by N^{3-} in the thin-film is expected to shift the conduction band by allowing greater hybridization between Nb4d and N2p orbitals.[36]

When comparing with $Sr_2Nb_2O_7$,[17] the addition of N2p orbital significantly decrease bandgap from 3.9 eV to 1.9 eV and shift the VBM more than 1 eV as expected for oxynitride.[44]

Photoelectrochemical ferrocyanide oxidation

To study the effect of $SrNbO_2N$ film thickness and roughness on photoelectrochemical performance, ferrocyanide oxidations in $[Fe(CN)_6]^{3-/4-}$ redox couples were performed. Because ferrocyanide oxidation is a barrier-less, single-electron, reversible process, it allows more direct determination of some semiconductor properties without the kinetic

losses that occur during the higher-barrier, four-electron, water oxidation processes.[46] 1.5 AM G-filtered simulated sunlight was illuminated in all reported photoelectrochemical measurements. Since the ferrocyanide/ferricyanide couple absorbs blue light, it may change the incident light intensity. To identify the actual power density of light that illuminates the sample through the ferri/ferrocyanide solution, we recorded spectral irradiance with and without ferri/ferrocyanide solution in 0.1 M KOH (Figure 4.7) The results show that power loss from a given concentration of ferro/ferricyanide is around 20% for 350-465 nm light under our conditions.

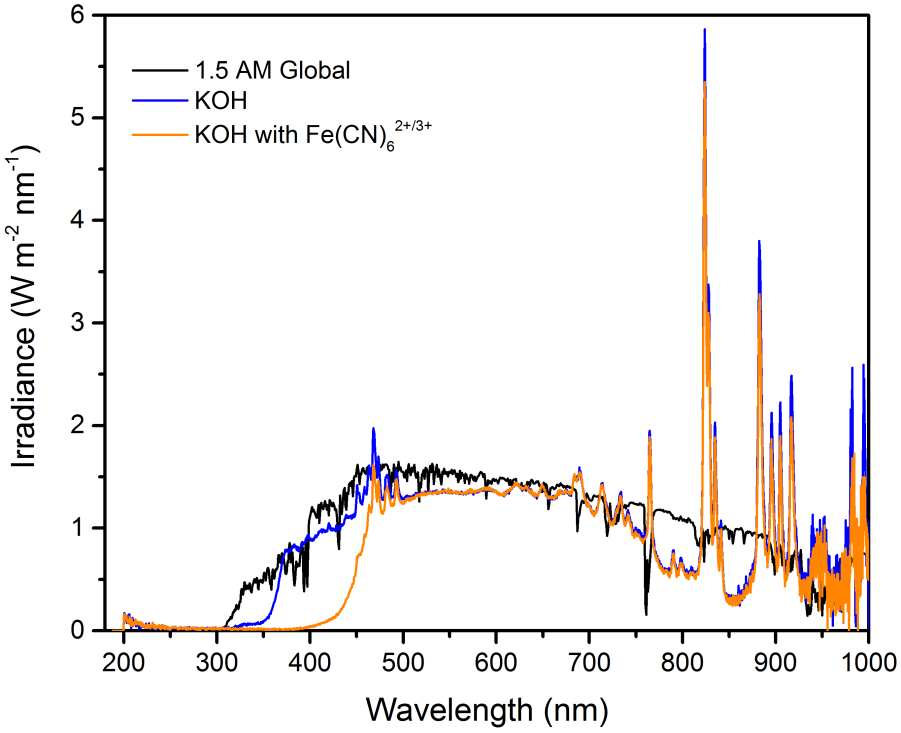

Figure 4.7 Spectral irradiance of 1.5 AM G filtered 300 W Xe arc lamp with (orange) and without (blue) $Fe(CN)_6^{2+/3+}$ in 0.1 M KOH electrolyte compared to 1.5 AM Global spectrum. Irradiance from 400 – 700 nm for 1.5 AMG Global, KOH, and KOH with $Fe(CN)_6^{2+/3+}$ is 463, 423, 342 W m^{-2}, respectively.

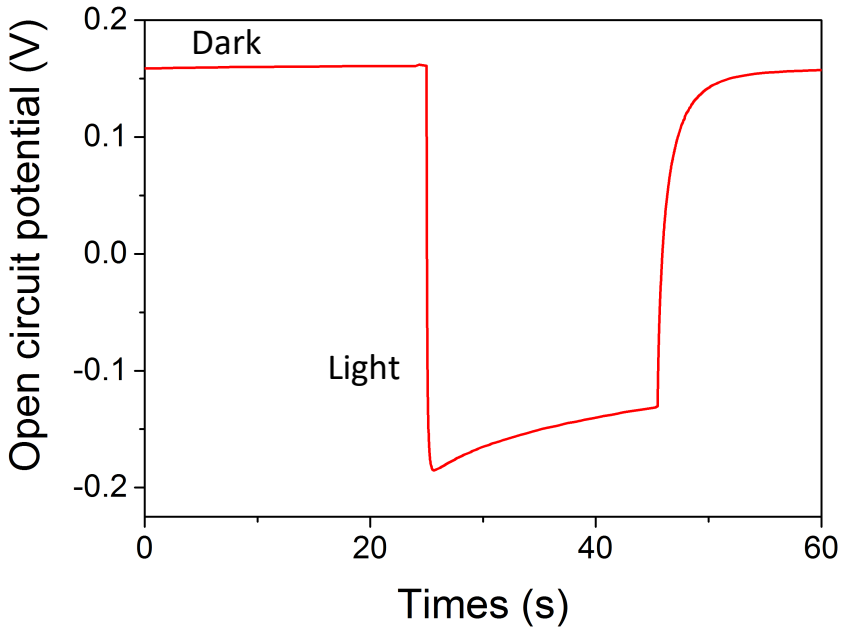

Figure 4.8 Example of open circuit potential (OCP) light and dark measurement to obtain photovoltage.

Figure 4.9a shows the linear sweep voltammograms (LSVs) of illuminated and dark $SrNbO_2N$ films of thicknesses 21, 92, 158, 334, and 440 nm. The onset potential of 21 and 92 nm thick films are around 0.9 V vs. RHE, whereas 158, 334, and 440 nm thickness films are near 0.73 V vs. RHE at 0.05 mA/cm^2. To evaluate photovoltage (V_{ph}) and compare it with onset potential, the difference between open-circuit potentials (OCP) under illumination and dark were measured (Figure 4.8) and summarized in Figure 4.10b. Similar to the results for the onset potential, the 21 and 92 nm films have similar averaged photo-voltage (190 mV). The highest averaged V_{ph} of 330 mV was obtained for the 334 nm thickness, which is very similar to the 440 nm thick film. The photocurrent density is another important metric to evaluate the photoabsorber, as it is directly related to solar-to-hydrogen efficiency.[2,46] The photocurrent density at 1.23 V vs. RHE was used for

comparison and is plotted in Figure 4.9b. The photocurrent density as a function of thickness graph shows a clear maximum, instead of a simple increase. The highest

photocurrent was measured at 334 nm, the same as the photovoltage result.

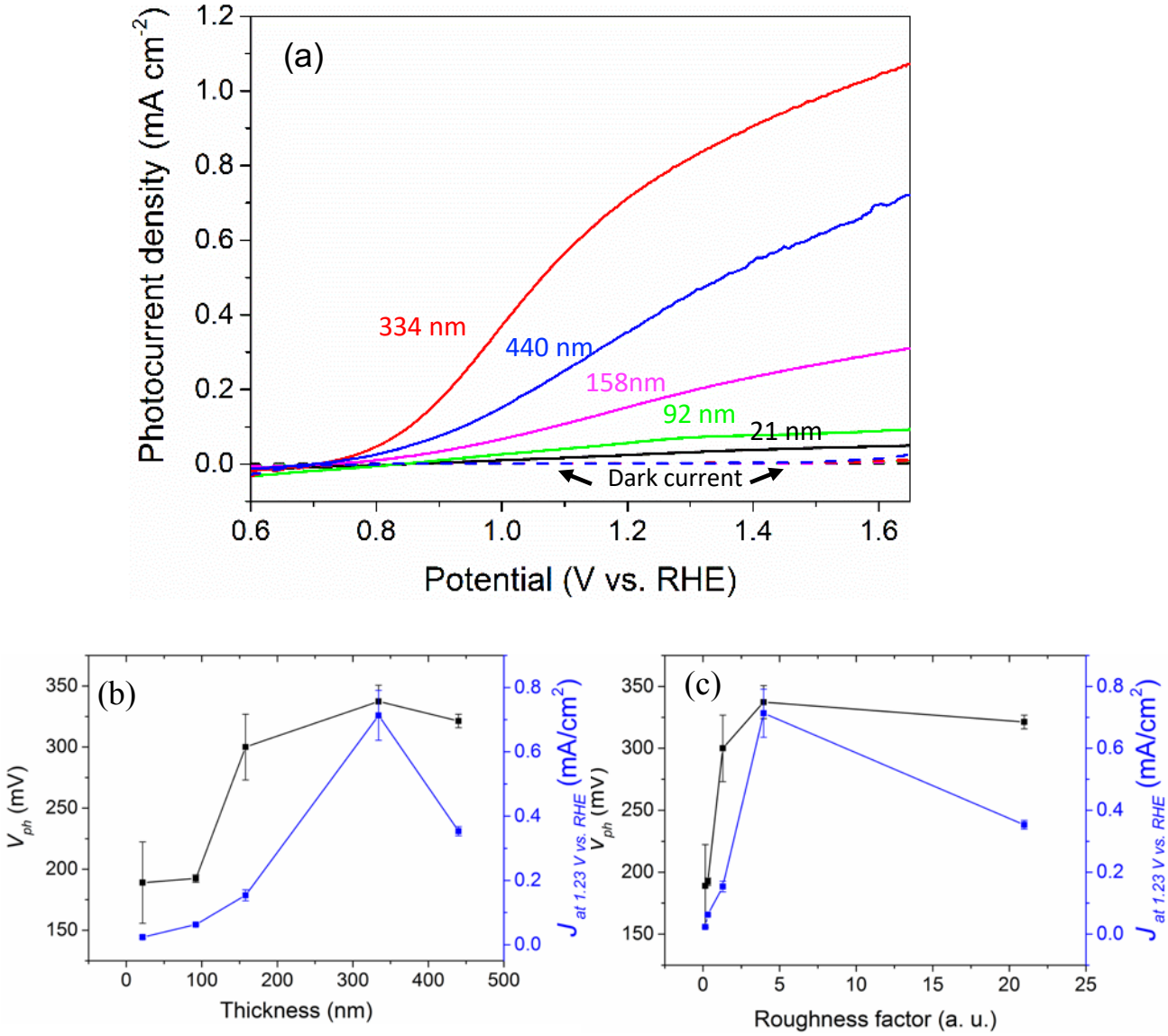

Figure 4.9 (a) Photoelectrochemical ferrocyanide oxidation of different thickness of $SrNbO_2N$ on TaN/Si. Scan rate is 10 mV/s. Photovoltage and photocurrent density at 1.23 V vs. RHE as a function of (b) thickness, and (c) roughness factor.

Considering that the light attenuation length of $SrNbO_2N$ is ~1 μm,[25] an increase of photocurrent density is expected up to ~1 μm thickness. However, since changing thickness also modifies the roughness and grain size[22] as observed by HIM images, other factors such as surface area, and carrier diffusion length have to be considered for PEC devices. The surface roughness is directly related to the electrochemical surface area, which is linearly proportional to the current density.[47] By contrast, for photovoltaic devices a high surface area photoabsorber can exacerbate surface recombination in the absence of efficient charge collection (metal contact or catalyst) [48,49] Because grain size and porosity of films can modify the mean distance that a minority carrier within the grains travels for collection, these properties must be tuned for optimal PEC performance.

To evaluate the effect of surface area and carrier diffusion length, photocurrent density and photovoltage are plotted as a function of roughness factor (Figure 4.9c). Both photovoltage and photocurrent density increase linearly up to a roughness factor of ~5, but both values decrease at higher roughness factors (e.g. 20). This can be explained as follows. Based on the HIM images (Figure 4.3 and Figure 4.4), the PEC performances as a function thickness, and the roughness factor (Figure 4.10b-c), the surface area and absorption length are the dominant factors determining PEC performance at thicknesses smaller than 100 nm. This is because the film is limited by insufficient light absorption. while the grain size is not limiting, as it is smaller than the minority carrier diffusion length. By contrast, for thickness greater than 150 nm, the larger grain size begins to exceed the carrier diffusion length and recombination starts to compete. Based on these results, at least a 100-150 nm $SrNbO_2N$ film should be used to achieve good light absorption without compromising

carrier diffusion to the surface. Although surface area (roughness, porosity, grain size) could not be independently controlled vs. photoabsorber thickness using this approach, both variables are demonstrated to contribute appreciably to PEC performance.

A nanostructuring approach has been shown to increase the photocurrent density for photoanodes that suffer from short carrier diffusion length.[50,51] Therefore for tandem PEC devices, it is crucial to know how surface area determines the photocurrent density, as it needs to be matched to the bottom junction.[5,52] To isolate the surface area contribution, we prepared $SrNbO_2N$ thin-films on a pyramidal nanostructured Si substrate. The pyramidal structure allows to increase the surface area 2-3 times, while maintaining the thickness and morphology of the $SrNbO_2N$ film similar to that on flat Si. Figure 4.10 shows HIM images

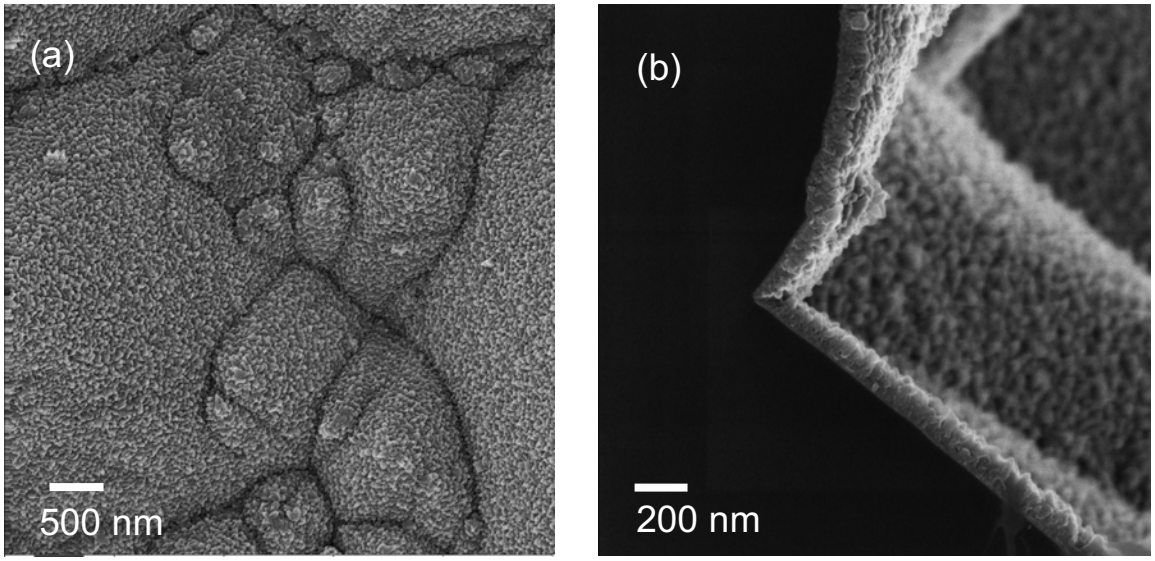

Figure 4.10 Top view (a) and cross-sectional view (b) of helium ion microscope (HIM) images for $SrNbO_2N$ thin-film on "structured" Si. The average thickness is 99.8 nm (± 3.6 nm)

of the top and cross-sectional view of $SrNbO_2N$ film on a pyramidal structured Si substrate.

The width and height of the pyramid are in the range of 0.1-3 μm and 2-3 μm, respectively. This footprint indeed creates a 2-3-fold increase in surface area and corroborates well with electrochemical surface area measurements (Figure 4.5). The thickness of the $SrNbO_2N$ was fabricated close to 100 nm to rule out carrier diffusion length limitations. Figure 4.11 compares the LSVs of $SrNbO_2N$ thin-films (approx. 100 nm) prepared on planar vs. pyramidal structured Si. The photocurrent density (at 1.23 V vs. RHE) of planar and structured substrates are 0.06 and 0.2 mA/cm^2, respectively, indicating that at a given thickness, photocurrent density is linearly proportional to the surface area, as expected.

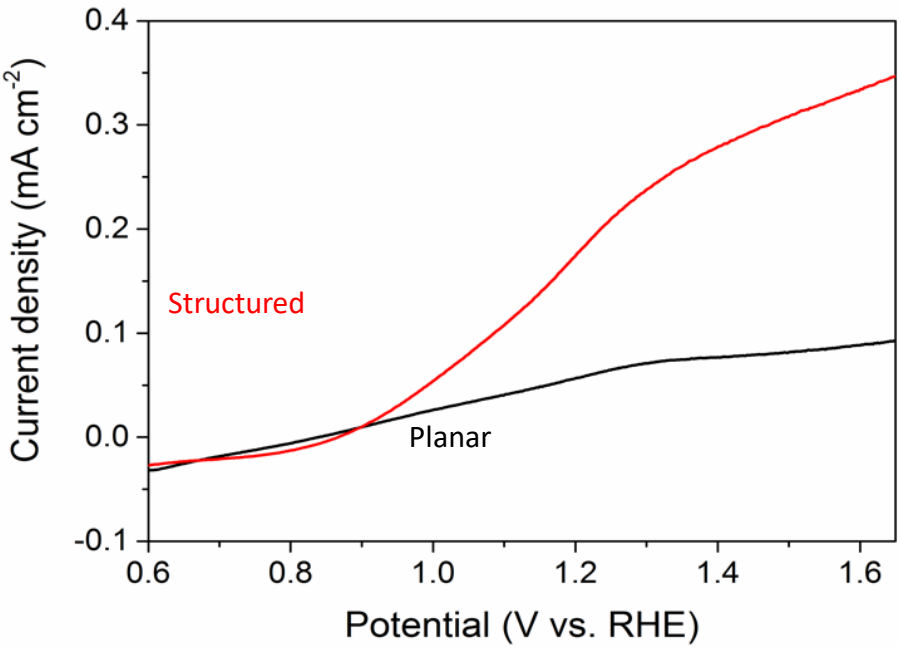

Figure 4.11 Photoelectrochemical ferrocyanide oxidation of $SrNbO_2N$ thin-film fabricated on structured and planar Si substrates. Scan rate is 10 mV/s

Photoelectrochemical OER

We examined the photoelectrochemical OER performance with and without OER catalyst, using the 334 nm thick $SrNbO_2N$ on a planar Si substrate sample. The samples were tested in 0.1 M KOH without any sacrificial agents under 1.5 AM G simulated solar illumination. RuO_x was selected for OER catalyst due to its high catalytic activity as well as conductivity.[53] RuO_x was deposited by an electrochemical deposition method using ruthenium trichloride hydrate salt (Details in Experimental). Ru3p core level spectra confirm successful RuO_x deposition (Figure 4.12a). Valence band spectra of RuO_x modified and unmodified $SrNbO_2N$ show that RuO_x modification adds energy states near the Fermi- level due to its high conductivity (Figure 4.12b). Figure 4.13 shows linear sweep voltammograms of unmodified and RuO_x-modified $SrNbO_2N$. The measured photocurrent density of unmodified and RuO_x-modified $SrNbO_2N$ are 0.03 and 0.06 mA/cm^2 at 1.23 V vs. RHE, and 0.09 and 0.37 mA/cm^2 at 1.6 V vs. RHE, respectively, corresponding to a 5-fold increase in the slope. The results are expected for RuO_x a highly active OER catalyst.

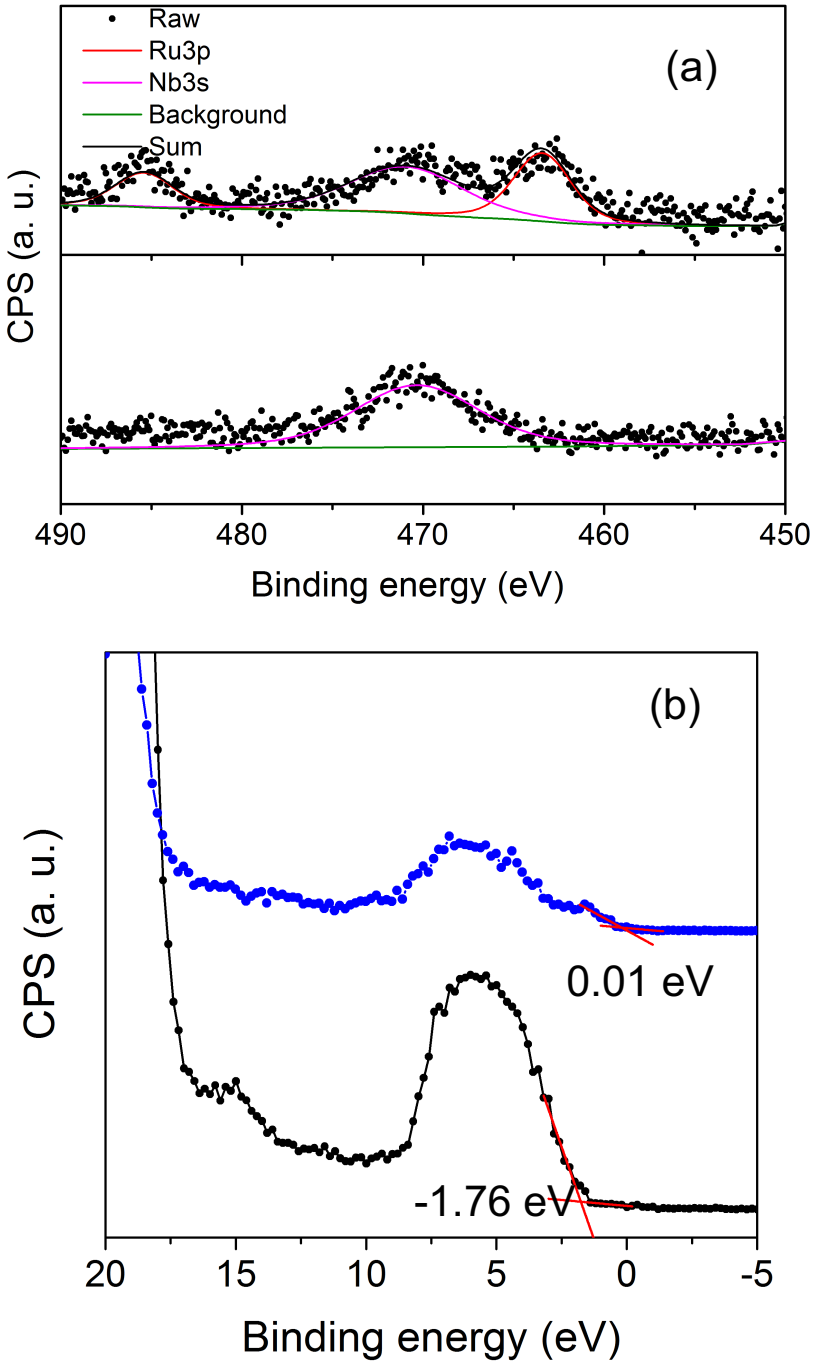

Figure 4.12 (a) XPS Ru3p core level spectra of $RuO_x/SrNbO_2N$ (top), and unmodified $SrNbO_2N$ (bottom). (b) XPS valence band spectra of $RuO_x/SrNbO_2N$ (top), and unmodified $SrNbO_2N$ (bottom).

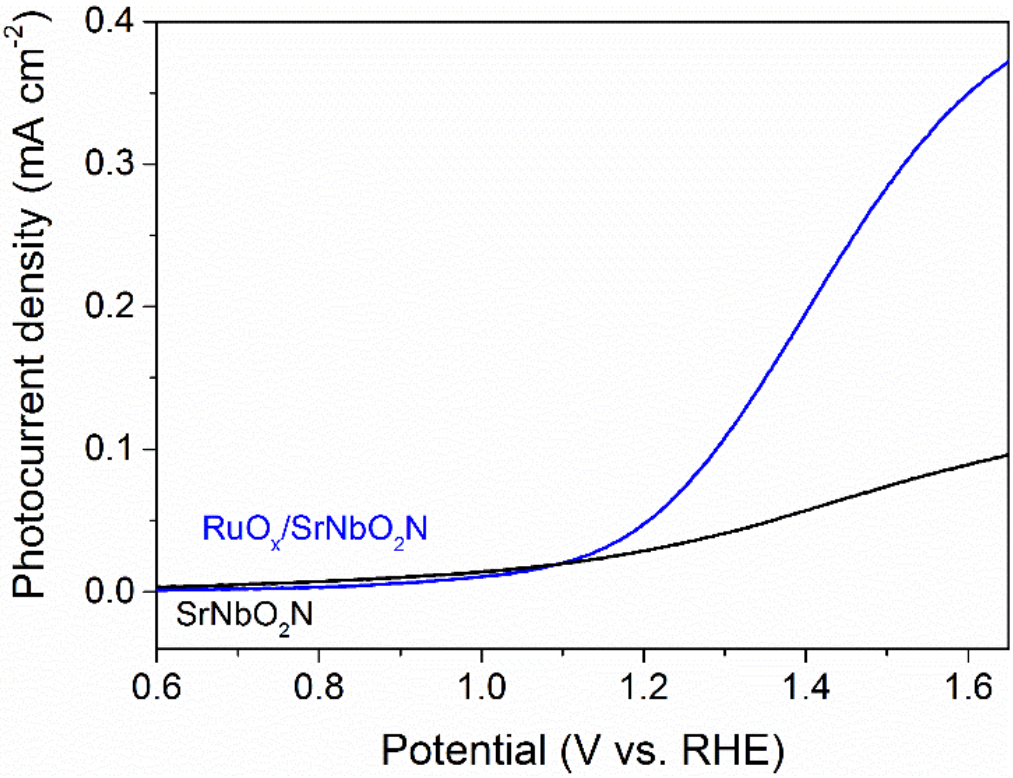

Figure 4.13 (a) Photoelectrochemical water oxidation of with and without RuO_x catalyst on 334 nm thickness $SrNbO_2N$/TaN/Si in 0.1 M KOH. Scan rate is 10 mV/s

4.5 Conclusions

In this work, we synthesized a polycrystalline $SrNbO_2N$ thin-film on a Si substrate and demonstrated that it can function in a tandem photo-absorber configuration with Si, if the film thickness, surface area, elemental stoichiometry, and morphology are properly controlled. A thin-film of TaN serves as an effective diffusion barrier that allows high-temperature ammonolysis to form an oxynitride thin-film without atomic interdiffusion into Si. The PEC performance as a function of thickness and roughness factor reveal that absorption length and surface area govern the PEC performance at a thickness (or grain

size) below 100 nm, whereas limited carrier diffusion length competes and lowers PEC performance at and above 150 nm. Experimental determination of the valence band minimum and conduction band maximum positions of $SrNbO_2N$ shows that it has the characteristics of an n-type semiconductor. Electrodeposition of RuO_x on this material leads to efficient electrocatalysis of water oxidation, demonstrating its suitability as a tandem PEC device. Ultimately, further advances of this PEC configuration could include a thin p-type semiconductor with a VBM located near -6.6 eV to facilitate hole transport and unidirectional capture at the surface.[54] The knowledge gained regarding requirements for thickness, morphology, and electronic structure advances our understanding of potential tandem PEC configurations utilizing $SrNbO_2N$ as photoanode. Lastly, the method for fabrication of high temperature phases on Si with TaN as a diffusion barrier highlights the opportunity to develop low-cost, tandem PEC devices based on silicon.

4.6 Acknowledgments

This work was supported by a joint DOE-EERE (energy Efficiency and Renewable Energy)/NSF-CBET (Chemical, Bioengineering, Environmental, and Transport systems) award number 1433492 and continuation award from DOE-EERE number DE-EE0008083. We thank Dr. P. Khalifah for helpful discussion on early stages of this project.

4.7 References

(1) Lewis, N. S.; Nocera, D. G. Powering the Planet: Chemical Challenges in Solar Energy Utilization. *PNAS* **2006**, *103* (43), 15729–15735.

(2) Prévot, M. S.; Sivula, K. Photoelectrochemical Tandem Cells for Solar Water Splitting. *J. Phys. Chem. C* **2013**, *117* (35), 17879–17893.

(3) Britto, R. J.; Benck, J. D.; Young, J. L.; Hahn, C.; Deutsch, T. G.; Jaramillo, T. F. Molybdenum Disulfide as a Protection Layer and Catalyst for Gallium Indium Phosphide Solar Water Splitting Photocathodes. *J. Phys. Chem. Lett.* **2016**, *7* (11), 2044–2049.

(4) Döscher, H.; Young, J. L.; Geisz, J. F.; Turner, J. A.; Deutsch, T. G. Solar-to-Hydrogen Efficiency: Shining Light on Photoelectrochemical Device Performance. *Energy Environ. Sci.* **2016**, *9* (1), 74–80.

(5) Young, J. L.; Steiner, M. A.; Döscher, H.; France, R. M.; Turner, J. A.; Deutsch, T. G. Direct Solar-to-Hydrogen Conversion via Inverted Metamorphic Multi-Junction Semiconductor Architectures. *Nature Energy* **2017**, *2* (4), 17028.

(6) Ager, J. W.; Shaner, M. R.; Walczak, K. A.; Sharp, I. D.; Ardo, S. Experimental Demonstrations of Spontaneous, Solar-Driven Photoelectrochemical Water Splitting. *Energy Environ. Sci.* **2015**, *8* (10), 2811–2824.

(7) Reece, S. Y.; Hamel, J. A.; Sung, K.; Jarvi, T. D.; Esswein, A. J.; Pijpers, J. J. H.; Nocera, D. G. Wireless Solar Water Splitting Using Silicon-Based Semiconductors and Earth-Abundant Catalysts. *Science* **2011**, *334* (6056), 645–648.

(8) Hu, S.; Xiang, C.; Haussener, S.; Berger, A. D.; Lewis, N. S. An Analysis of the Optimal Band Gaps of Light Absorbers in Integrated Tandem Photoelectrochemical Water-Splitting Systems. *Energy Environ. Sci.* **2013**, *6* (10), 2984–2993.

(9) Porter, S. H.; Huang, Z.; Woodward, P. M. Study of Anion Order/Disorder in RTaN2O (R = La, Ce, Pr) Perovskite Nitride Oxides. *Cryst. Growth Des.* **2014**, *14* (14), 117–125.

(10) Porter, S. H.; Huang, Z.; Dou, S.; Brown-Xu, S.; Sarwar, A. T. M. G.; Myers, R. C.; Woodward, P. M. Electronic Structure and Photocatalytic Water Oxidation Activity of RTiNO2 (R = Ce, Pr, and Nd) Perovskite Nitride Oxides. *Chem. Mat.* **2015**, *27* (7), 2414–2420.

(11) Seo, J.; Nishiyama, H.; Yamada, T.; Domen, K. Visible-Light-Responsive Photoanodes for Highly Active, Stable Water Oxidation. *Angew. Chem. Int. Ed. Engl.* **2018**, *57* (28), 8396–8415.

(12) Higashi, M.; Domen, K.; Abe, R. Fabrication of an Efficient BaTaO2N Photoanode Harvesting a Wide Range of Visible Light for Water Splitting. *Cryst. Growth Des.* **2013**, *135* (28), 10238–10241.

(13) Maeda, K.; Higashi, M.; Siritanaratkul, B.; Abe, R.; Domen, K. SrNbO 2N as a Water-Splitting Photoanode with a Wide Visible-Light Absorption Band. *J. Am. Chem. Soc.* **2011**, *133* (32), 12334–12337.

(14) Asako Kasahara; Kota Nukumizu; Go Hitoki; Tsuyoshi Takata; Junko N Kondo; Michikazu Hara; Hisayoshi Kobayashi, A.; Kazunari Domen. Photoreactions on LaTiO2N Under Visible Light Irradiation. *J. Phys. Chem. A* **2002**, *106*, 6750–6753.

(15) Castelli, I. E.; Olsen, T.; Datta, S.; Landis, D. D.; Dahl, S.; Thygesen, K. S.; Jacobsen, K. W. Computational Screening of Perovskite Metal Oxides for Optimal Solar Light Capture. *Energy Environ. Sci.* **2012**, *5* (2), 5814–5819.

(16) Young-Il Kim; Patrick M Woodward; Karim Z Baba-Kishi, A.; Tai, C. W. Characterization of the Structural, Optical, and Dielectric Properties of Oxynitride Perovskites AMO2N (a = Ba, Sr, Ca; M = Ta, Nb). *Chem. Mater.* **2004**, *16* (7), 1267–1276.

(17) Ebbinghaus, S. G.; Aguiar, R.; Weidenkaff, A.; Gsell, S.; Reller, A. Topotactical Growth of Thick Perovskite Oxynitride Layers by Nitridation of Single Crystalline Oxides. *Solid State Sciences* **2008**, *10* (6), 709–716.

(18) Sun, X.; Liu, G.; Xu, X. Defect Management and Efficient Photocatalytic Water Oxidation Reaction Over Mg Modified SrNbO 2 N. *J. Mat. Chem. A* **2018**, *6* (23), 10947–10957.

(19) Kodera, M.; Urabe, H.; Katayama, M.; Hisatomi, T.; Minegishi, T.; Domen, K. Effects of Flux Synthesis on SrNbO2N Particles for Photoelectrochemical Water Splitting. *J. Mat. Chem. A* **2016**, *4* (20), 7658–7664.

(20) Kawashima, K.; Hojamberdiev, M.; Mabayoje, O.; Wygant, B. R.; Yubuta, K.; Mullins, C. B.; Domen, K.; Teshima, K. NH 3 -Assisted Chloride Flux-Coating Method for Direct

Fabrication of Visible-Light-Responsive SrNbO 2 N Crystal Layers. *CrystEngComm* **2017**, *19* (37), 5532–5541.

(21) Hiralal, P.; Saremi-Yarahmadi, S.; Bayer, B. C.; Wang, H.; Hofmann, S.; Upul Wijayantha, K. G.; Amaratunga, G. A. J. Nanostructured Hematite Photoelectrochemical Electrodes Prepared by the Low Temperature Thermal Oxidation of Iron. *Sol. Energy Mater. Sol. Cells* **2011**, *95* (7), 1819–1825.

(22) Pinaud, B. A.; Vesborg, P. C. K.; Jaramillo, T. F. Effect of Film Morphology and Thickness on Charge Transport in Ta3N5/Ta Photoanodes for Solar Water Splitting. *J. Phys. Chem. Lett.* **2012**, *116* (30), 15918–15924.

(23) Kuang, Y.; Jia, Q.; Nishiyama, H.; Yamada, T.; Kudo, A.; Domen, K. A Front-Illuminated Nanostructured Transparent BiVO4 Photoanode for >2% Efficient Water Splitting. *Adv. Energy Mater.* **2016**, *6* (2), 1501645.

(24) Porter, S. H.; Hwang, S.; Amarasinghe, V.; Taghaddos, E.; Manichev, V.; Li, M.; Gardner, G.; Safari, A.; Garfunkel, E.; Greenblatt, M.; et al. Optimizing "Artificial Leaf" Photoanode-Photocathode-Catalyst Interface Systems for Solar Water Splitting. *ECS Trans.* **2016**, *72* (37), 1–19.

(25) Kikuchi, R.; Nakamura, T.; Tamura, S.; Kaneko, Y.; Hato, K. Fundamental Semiconducting Properties of Perovskite Oxynitride SrNbO2N: Epitaxial Growth and Characterization. *Cryst. Growth Des.* **2017**, *29* (18), 7697–7703.

(26) Kim, H.; Lavoie, C.; Copel, M.; Narayanan, V.; Park, D. G.; Rossnagel, S. M. The Physical Properties of Cubic Plasma-Enhanced Atomic Layer Deposition TaN Films. *J. Appl. Phys.* **2004**, *95* (10), 5848–5855.

(27) Kwon, J.-D.; Jeong, S.-J.; Kang, J.-W.; Kim, D.-G.; Kim, J.-K.; Rha, J.-J.; Nam, K.-S.; Kwon, S.-H. Low Temperature Two-Step Atomic Layer Deposition of Tantalum Nitride for Cu Diffusion Barrier. *J. Electrochem. Soc.* **2009**, *156* (11), H832–H835.

(28) Rossnagel, S. M.; Kim, H. Diffusion Barrier Properties of Very Thin TaN with High Nitrogen Concentration. *Journal of Vacuum Science & Technology B: Microelectronics and Nanometer Structures Processing, Measurement, and Phenomena* **2003**, *21* (6), 2550.

(29) Hwang, S.; Porter, S. H.; Laursen, A. B.; Yang, H.; Li, M.; Manichev, V.; Calvinho, K. U. D.; Amarasinghe, V.; Greenblatt, M.; Garfunkel, E.; et al. Creating Stable Interfaces Between Reactive Materials: Titanium Nitride Protects Photoabsorber–Catalyst Interface in Water-Splitting Photocathodes. *J. Mat. Chem. A* **2019**, *7* (5), 2400–2411.

(30) Mayer, M. *SIMNRA User's Guide*; Max-Planck-Institut für Plasmaphysik, 1997.

(31) Golecki, I. Rutherford Backscattering and Channeling Analysis of Epitaxial, Low-Mass Films on High-Mass Substrates. *Nucl. Instrum. Methods Phys. Res* **1983**, *218* (1-3), 63–66.

(32) Seo, J.; Moriya, Y.; Kodera, M.; Hisatomi, T.; Minegishi, T.; Katayama, M.; Domen, K. Photoelectrochemical Water Splitting on Particulate ANbO2N (a = Ba, Sr) Photoanodes Prepared From Perovskite-Type ANbO3. *Chem. Mater.* **2016**, *28* (19), 6869–6876.

(33) Atuchin, V. V.; Grivel, J. C.; Korotkov, A. S.; Zhang, Z. Electronic Parameters of Sr2Nb2O7 and Chemical Bonding. *Journal of Solid State Chemistry* **2008**, *181* (6), 1285–1291.

(34) Wang, J.; Wang, X.; Liu, B.; Li, X.; Cao, M. Facile Synthesis of SrNbO2N Nanoparticles with Excellent Visible-Light Photocatalytic Performances. *Materials Letters* **2015**, *152*, 131–134.

(35) Ji, L.; McDaniel, M. D.; Wang, S.; Posadas, A. B.; Li, X.; Huang, H.; Lee, J. C.; Demkov, A. A.; Bard, A. J.; Ekerdt, J. G.; et al. A Silicon-Based Photocathode for Water Reduction with an Epitaxial SrTiO3 Protection Layer and a Nanostructured Catalyst. *Nature Nanotechnology* **2015**, *10* (1), 84–90.

(36) Oka, D.; Hirose, Y.; Kaneko, M.; Nakao, S.; Fukumura, T.; Yamashita, K.; Hasegawa, T. Anion-Substitution-Induced Nonrigid Variation of Band Structure in SrNbO3–xNx ($0 \leq X \leq 1$) Epitaxial Thin Films. *ACS Appl. Mater. Interfaces* **2018**, *10* (41), 35008–35015.

(37) Narkeviciute, I.; Jaramillo, T. F. Impact of Nanostructuring on the Photoelectrochemical Performance of Si/Ta3N5 Nanowire Photoanodes. *J. Phys. Chem. C* **2017**, *121* (49), 27295–27302.

(38) Kibsgaard, J.; Tsai, C.; Chan, K.; Benck, J. D.; Nørskov, J. K.; Abild-Pedersen, F.; Jaramillo, T. F. Designing an Improved Transition Metal Phosphide Catalyst for Hydrogen Evolution Using Experimental and Theoretical Trends. *Energy Environ. Sci.* **2015**, *8* (10), 3022–3029.

(39) Nurlaela, E.; Ould-Chikh, S.; Harb, M.; del Gobbo, S.; Aouine, M.; Puzenat, E.; Sautet, P.; Domen, K.; Basset, J.-M.; Takanabe, K. Critical Role of the Semiconductor–Electrolyte Interface in Photocatalytic Performance for Water-Splitting Reactions Using Ta3N5 Particles. *Chem. Mat.* **2014**, *26* (26), 4812–4825.

(40) Xu, J.; Pan, C.; Takata, T.; Domen, K. Photocatalytic Overall Water Splitting on the Perovskite-Type Transition Metal Oxynitride CaTaO 2 N Under Visible Light Irradiation. *Chemical Communications* **2015**, *51* (33), 7191–7194.

(41) McClure, E. T.; Ball, M. R.; Windl, W.; Woodward, P. M. Cs2AgBiX6 (X = Br, Cl): New Visible Light Absorbing, Lead-Free Halide Perovskite Semiconductors. *Chem. Mat.* **2016**, *28* (5), 1348–1354.

(42) Zhou, X.; Liu, R.; Sun, K.; Friedrich, D.; McDowell, M. T.; Yang, F.; Omelchenko, S. T.; Saadi, F. H.; Nielander, A. C.; Yalamanchili, S.; et al. Interface Engineering of the Photoelectrochemical Performance of Ni-Oxide-Coated N-Si Photoanodes by Atomic-Layer Deposition of Ultrathin Films of Cobalt Oxide. *Energy Environ. Sci.* **2015**, *8* (9), 2644–2649.

(43) Nonnenmacher, M.; o'Boyle, M. P.; Wickramasinghe, H. K. Kelvin Probe Force Microscopy. *Appl. Phys. Lett.* **1998**, *58* (25), 2921–2923.

(44) Balaz, S.; Porter, S. H.; Woodward, P. M.; Brillson, L. J. Electronic Structure of Tantalum Oxynitride Perovskite Photocatalysts. *Chem. Mater.* **2013**, *25* (16), 3337–3343.

(45) Trasatti, S. The Absolute Electrode Potential: an Explanatory Note (Recommendations 1986). *J. Electroanal. Chem* **1986**, *58* (7), 955–966.

(46) Narkeviciute, I.; Jaramillo, T. F. Effects of Ta3N5 Morphology and Composition on the Performance of Si-Ta3N-5 Photoanodes. *Solar RRL* **2017**, *110*, 1700121.

(47) McCrory, C. C. L.; Jung, S.; Ferrer, I. M.; Chatman, S. M.; Peters, J. C.; Jaramillo, T. F. Benchmarking Hydrogen Evolving Reaction and Oxygen Evolving Reaction Electrocatalysts for Solar Water Splitting Devices. *J. Am. Chem. Soc.* **2015**, *137* (13), 4347–4357.

(48) Zhu, K.; Kopidakis, N.; of, N. N. T. J.; 2006. Influence of Surface Area on Charge Transport and Recombination in Dye-Sensitized TiO2 Solar Cells | the Journal of Physical Chemistry B. *J. Phys. Chem. B* **2006**, *110*, 25174–25180.

(49) Oh, J.; Yuan, H.-C.; Branz, H. M. An 18.2%-Efficient Black-Silicon Solar Cell Achieved Through Control of Carrier Recombination in Nanostructures. *Nature Nanotechnology* **2012**, *7* (11), 743–748.

(50) Narkeviciute, I.; Chakthranont, P.; Mackus, A. J. M.; Hahn, C.; Pinaud, B. A.; Bent, S. F.; Jaramillo, T. F. Tandem Core–Shell Si–Ta3N5 Photoanodes for Photoelectrochemical Water Splitting. *Nano Lett.* **2016**, *16* (16), 7565–7572.

(51) Liardet, L.; Katz, J. E.; Luo, J.; Grätzel, M.; Hu, X. An Ultrathin Cobalt–Iron Oxide Catalyst for Water Oxidation on Nanostructured Hematite Photoanodes. *J. Mat. Chem. A* **2019**, *7* (11), 6012–6020.

(52) Cheng, W.-H.; Richter, M. H.; May, M. M.; Ohlmann, J.; Lackner, D.; Dimroth, F.; Hannappel, T.; Atwater, H. A.; Lewerenz, H. J. Monolithic Photoelectrochemical Device for Direct Water Splitting with 19% Efficiency. *ACS Energy Letters* **2018**, *3* (8), 1795–1800.

(53) Lee, Y.; Suntivich, J.; May, K. J.; Perry, E. E.; Shao-Horn, Y. Synthesis and Activities of Rutile IrO 2and RuO 2Nanoparticles for Oxygen Evolution in Acid and Alkaline Solutions. *J. Phys. Chem. Lett.* **2012**, *3* (3), 399–404.

(54) Seger, B.; Castelli, I. E.; Vesborg, P. C. K.; Jacobsen, K. W.; Hansen, O.; Chorkendorff, I. 2-Photon Tandem Device for Water Splitting: Comparing Photocathode First Versus Photoanode First Designs. *Energy Environ. Sci.* **2014**, *7* (8), 2397–2413.

Appendix

TiN film absorption coefficient estimation (Chapter 2)

To estimate absorption coefficient of the TiN film, we used general three-layer model shown here.

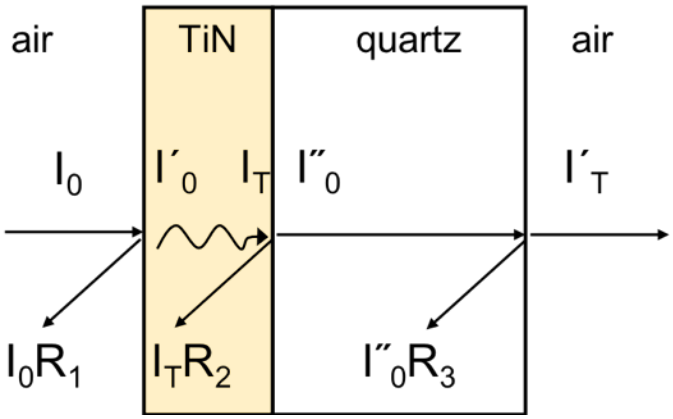

When the incident light intensity (I_0) propagate to the layers, the transmittance (T) can be defined

$$T = \frac{I'_T}{I_0} = (1 - R_1)(1 - R_2)(1 - R_3)e^{-\alpha x}$$

Where R_i is reflectance of each interface, α is absorption coefficient, and x is thickness of TiN film (4 nm). Since the extinction coefficient of the quartz substrate is zero, there is no loss of the light intensity in the quartz medium. (no loss of I''_0 in quartz medium).

Because the difference between the total reflectance of TiN/quartz and bare quartz is negligible based on the **Figure 2.3**, we can estimate $R_1 \sim 0$, and $R_2 \approx R_3$ (same as quartz).

Then, absorption coefficient α is

$$\alpha = -\frac{1}{x} ln \frac{T}{(1-R)^2}$$

At 500 nm,

$$\alpha = -\frac{1}{(4 \times 10^{-9} m)} ln \frac{0.753}{(1-0.036)^2} = 5.2 \times 10^5 \, cm^{-1}$$

Rutherford backscattering (RBS) thickness estimation (Chapter 2)

Simulated RBS spectra give thickness information as the number of atoms per unit area (atoms/cm^2). Using the atomic density of each material, thickness can be estimated using the following formula:

$$Thickness = \frac{Atoms\ per\ square\ cm\ (\frac{atoms}{cm^2})}{Atomic\ density\ (\frac{atoms}{cm^3})}$$

Atomic density can be obtained using the following formula:

$$Atomic\ density = \frac{(Avogadro's\ number)(Density)}{Molecular\ weight/\#\ of\ atoms}$$

NiP_2 thickness:

The number of atoms per sq. cm of NiP_2 obtained from RBS is 4.0×10^{16} atoms/cm^2.

$$Thickness = \frac{(5.0 \times 10^{16} atoms\ cm^{-2})}{(6.022 \times 10^{23}\ mol^{-1})(4.89\ \frac{g}{cm^{-3}})(\frac{mol}{40.21\ g})}$$

$$= 6.82 \times 10^{-7} cm$$

$$= 6.8\ nm$$

TiN thickness:

The number of atoms per sq. cm of the TiN obtained from RBS is 4.2×10^{16} atoms/cm^2.

Although composition of the TiN was identified as $Ti_{0.39}N_{0.33}O_{0.27}$, we used the atomic density of TiN since oxygen incorporation would not significantly alter the atomic density.

$$Thickness = \frac{(4.2 \times 10^{16} atoms\ cm^{-2})}{(6.022 \times 10^{23}\ mol^{-1})(5.4 \frac{g}{cm^{-3}})(\frac{mol}{30.93\ g})}$$

$$= 3.99 \times 10^{-7} cm \approx 4.0\ nm$$

$Ni_{0.2}P_{0.39}Ti_{0.05}O_{0.18}N_{0.2}$ interfacial layer thickness:

The number of atoms per sq. cm of the interfacial layer obtained from RBS is 5.1×10^{16} atoms/cm^2. We used the density of $Ni_3(PO_4)_2$ for the calculation since this is the closest equivalent composition that exists in the literature.

$$Thickness = \frac{(5.1 \times 10^{16} atoms\ cm^{-2})}{(6.022 \times 10^{23}\ mol^{-1})(4.42 \frac{g}{cm^{-3}})(\frac{mol}{28.88\ g})}$$

$$= 5.53 \times 10^{-7} cm \approx 5.5\ nm$$

Turn-over frequency (TOF) analysis

The turn-over frequency can be obtained using the following formula [1,2]:

$$TOF = \frac{\#\ total\ hydrogen\ turn\ overs/cm^2_{geo}}{\#\ surface\ sites/cm^2_{geo}}$$

In order to estimate the turn-over frequency of a catalyst as a function of overpotential, the number of surface active sites per surface area of our film needs to be determined. Since the exact active sites for hydrogen binding is unknown for cubic NiP_2, we employed the method used by Kibsgaard et al.[2] By using this method, the total number of surface sites from the unit cell of cubic NiP_2 crystal structure (PDF 01-073-0436) is used to estimate the average number of surface sites assuming all surface sites are active and then averaging these over the entire surface area of the unit cell. This gives a geometric average atom density per unit surface area.

Cubic NiP_2:

Cell volume: 163.72 $Å^3$, 12 atoms per unit cell (4 Ni + 8 P)

$$\#\ surface\ sites = \left(\frac{12\ atoms/\ unit\ cell}{163.73\ Å^3}\right)^{\frac{2}{3}} = 1.75 \times 10^{15} atoms/cm^2_{ECSA}$$

To obtain the electrochemical surface area, we use the electrochemical intrinsic capacitance (EC) measurement. Using the cyclic voltammogram (Figure 2.11b) the roughness factor (R_f) is 2.75 cm^2_{ECSA}/cm^2_{geo} while the atomic force microscope-derived R_f (Figure 2.11a) is 1.08 cm^2_{ECSA}/cm^2_{geo}. Using roughness factor from electrochemical surface area, the TOF can be calculated:

$$TOF = (j\frac{A}{cm^2})(\frac{1\ mol}{96485.3\ C})(\frac{1\ mol\ H_2}{2\ mol\ e^-})(\frac{6.022\ \times 10^{23}\ H_2}{1\ mol\ H_2})(\frac{1}{1.75 \times \frac{10^{15} atoms}{cm^2_{ECSA}} \times R_f})$$

References

(1) Kibsgaard, J.; Tsai, C.; Chan, K.; Benck, J. D.; Nørskov, J. K.; Abild-Pedersen, F.; Jaramillo, T. F. Designing an Improved Transition Metal Phosphide Catalyst for Hydrogen Evolution Using Experimental and Theoretical Trends. *Energy Environ. Sci.* **2015**, *8*, 3022–3029.

(2) Hellstern, T. R.; Benck, J. D.; Kibsgaard, J.; Hahn, C.; Jaramillo, T. F. Engineering Cobalt Phosphide (CoP) Thin Film Catalysts for Enhanced Hydrogen Evolution Activity on Silicon Photocathodes. *Adv. Energy Mater.* **2015**, 1501758.